

# Ultrashort filaments of light in weakly ionized, optically transparent media

L Bergé<sup>1</sup>, S Skupin<sup>1</sup>, R Nuter<sup>1</sup>, J Kasparian<sup>2</sup> and J-P Wolf<sup>3</sup>

<sup>1</sup> Département de Physique Théorique et Appliquée, CEA-DAM/Ile de France, B.P. 12, 91680 Bruyères-le-Châtel, France

<sup>2</sup> Laboratoire de Spectroscopie Ionique et Moléculaire, Université Claude Bernard Lyon 1, 43 bd du 11 Novembre, 69622 Villeurbanne Cedex, France

<sup>3</sup> GAP-Biophotonics, Université de Genève, 20 Rue de l'Ecole de Médecine, 1211 Genève 4, Switzerland

E-mail: [luc.berge@cea.fr](mailto:luc.berge@cea.fr)

Received 5 May 2007, in final form 2 September 2007

Published 26 September 2007

Online at [stacks.iop.org/RoPP/70/1633](http://stacks.iop.org/RoPP/70/1633)

## Abstract

Modern laser sources nowadays deliver ultrashort light pulses reaching few cycles in duration and peak powers exceeding several terawatt (TW). When such pulses propagate through optically transparent media, they first self-focus in space and grow in intensity, until they generate a tenuous plasma by photo-ionization. For free electron densities and beam intensities below their breakdown limits, these pulses evolve as self-guided objects, resulting from successive equilibria between the Kerr focusing process, the chromatic dispersion of the medium and the defocusing action of the electron plasma. Discovered one decade ago, this self-channeling mechanism reveals a new physics, widely extending the frontiers of nonlinear optics. Implications include long-distance propagation of TW beams in the atmosphere, supercontinuum emission, pulse shortening as well as high-order harmonic generation. This review presents the landmarks of the 10-odd-year progress in this field. Particular emphasis is laid on the theoretical modeling of the propagation equations, whose physical ingredients are discussed from numerical simulations. The dynamics of single filaments created over laboratory scales in various materials such as noble gases, liquids and dielectrics reveal new perspectives in pulse shortening techniques. Far-field spectra provide promising diagnostics. Attention is also paid to the multifilamentation instability of broad beams, breaking up the energy distribution into small-scale cells along the optical path. The robustness of the resulting filaments in adverse weathers, their large conical emission exploited for multipollutant remote sensing, nonlinear spectroscopy and the possibility of guiding electric discharges in air are finally addressed on the basis of experimental results.

(Some figures in this article are in colour only in the electronic version)

## Contents

	Page
1. Introduction	1636
2. Propagation equations	1637
2.1. Helmholtz equation	1638
2.1.1. From vectorial to scalar description	1639
2.1.2. Weak backscattering	1639
2.1.3. Unidirectional pulse propagation	1639
2.1.4. Envelope description	1641
2.2. Nonlinear optical responses	1641
2.3. Plasma generation for singly charged ionization	1643
3. Optical ultrashort filaments: a few tools for their analytical description	1648
3.1. Kerr focusing and wave collapse	1648
3.1.1. Principles of wave self-focusing	1649
3.1.2. Variational and perturbative approaches	1650
3.2. Saturation by temporal dispersion	1651
3.3. Saturation by plasma defocusing	1653
3.4. Saturation by optical nonlinearities	1654
3.5. Self-phase modulation and supercontinuum generation	1657
3.6. Modulational instabilities: the route to multiple filamentation	1657
4. Universal features of femtosecond filamentation	1660
4.1. Radial self-focusing and temporal splittings	1661
4.2. Robustness and multifilamentation	1663
4.3. White-light generation and conical emission	1666
4.4. Role of the laser wavelength	1670
5. Ultrashort filaments in gases	1671
5.1. Novel perspectives for pulse shortening	1672
5.2. High-order harmonic generation	1674
6. Ultrashort filaments in dense media	1677
6.1. Pulse propagation in dielectrics and damages	1677
6.2. Pulse propagation in liquids and applications	1679
6.3. X/O waves and far-field spectra	1680
7. Filaments in the atmosphere: conveying intense structures over kilometres	1683
7.1. Long-distance propagation and white-light supercontinuum	1684
7.1.1. Temporal chirping and spatial lensing	1684
7.1.2. Plasma and optical field measurements	1685
7.1.3. Multifilamentation	1688
7.1.4. White-light generation	1691
7.2. Remote sensing (LIDAR) applications	1693
7.2.1. Principle of LIDAR: towards ‘femtolidars’	1693
7.2.2. Remote filament-induced breakdown spectroscopy	1695
7.3. Towards a laser lightning rod	1696
8. Outlook	1698

---

Acknowledgments	1698
Appendix A. List of abbreviations	1699
Appendix B. Ionization rates for atoms and molecules	1699
Appendix B.1. Ionization in gases	1699
Appendix B.1.1. Keldysh theory	1699
Appendix B.1.2. The PPT theory	1701
Appendix B.1.3. The ADK molecular theory	1702
Appendix B.2. Ionization in dense media	1702
Appendix C. Atomic dipole for high harmonic generation	1703
Appendix D. The Teramobile laser	1705
References	1706



**Figure 1.** Principle of producing femtosecond filaments in air at the laser wavelength of 800 nm. Photograph at the right-hand side shows a transverse cut of the filament profile.

## 1. Introduction

Over the past two decades, ultrafast laser sources producing ultrashort pulses have come of age. Technological advances in this field have permitted the generation of light wave-packets comprising only a few oscillation cycles of the electric field. Mode-locking and chirped-pulse amplification (CPA) technologies allow to access smaller and smaller pulse durations, down to the femtosecond scale ( $1 \text{ fs} = 10^{-15} \text{ s}$ ). Optical intensities locally exceed hundreds of terawatt (TW) per  $\text{cm}^2$  at moderate (mJ) energies. Due to extreme temporal and spatial confinements, the pulse strength exceeds that of the Coulomb field which binds electrons at their nucleus. It becomes strong enough to overcome the Coulomb barrier and triggers optical-field ionization.

In this regime, an intriguing phenomenon was discovered by [Braun \*et al\* \(1995\)](#) in the middle of the nineties. By launching infrared pulses with femtosecond durations and gigawatt (GW) powers in the atmosphere, the beam became confined to a long-living, self-confined tube of light capable of covering several tens of metres, i.e. many linear diffraction lengths along the propagation axis. The mechanism supporting this ‘light bullet’ results from the balance between Kerr focusing, which increases the local optical index with the wave intensity and self-induced ionization. When an ultrashort pulse self-focuses and couples with a self-induced plasma channel, its spatial profile exhibits a narrow extent along the optical path. Spectra broaden due to self-phase modulation (SPM), which is sustained by the mechanism of high intensity clamping. This picture classically refers to what is commonly called a ‘femtosecond filament’. In the diffraction plane, this filament is characterized by a white-light spot, surrounded by concentric ‘rainbows’ with colors ranging from red to green. The high nonlinearities competing through the filamentation process produce an impressive supercontinuum leading to white-light emission. They also affect the beam divergence through an apparent conical emission, as illustrated in figure 1.

Femtosecond filaments have, for the last decade, opened the route to a fascinating physics. Their highly nonlinear dynamics sparked broad interest, first because femtosecond pulses are able to convey high intensities over spectacular distances, second because the white-light emitted by the filaments transforms infrared lasers into ‘white-light lasers’ ([Chin \*et al\* 1999b](#), [Kasparian \*et al\* 2003](#)). For appropriate beam configurations, long fs filaments can be created not only in the atmosphere but also in noble gases, liquids and dielectrics, as long as the pulse intensity does not reach the limit of optical breakdown and the electron plasma remains at subdense levels. The dynamical balance between nonlinear focusing and ionization can result in a drastic shortening of the pulse duration, down to the optical cycle limit. This property offers promising perspectives to generically deliver light waves with durations of a few fs only, which should further impact the fields of high-order harmonic generation and sub-fs pulse production. In solids, femtosecond filaments are used to imprint irreversible tracks and modify the birefringence of the medium near the breakdown threshold. This opens new routes for material micro-processing. In liquids, filaments can be self-guided over long distances, without causing any damage. Their spectral signatures, occurring as X or O-shaped lines in the far-field spectrum, may supply efficient diagnostics to extract information about the nonlinear pulse dynamics. In air, femtosecond pulses with broad spatial extents create several

filaments, whose mutual interactions support the self-guiding of the beam envelope and can preserve a confined state over several kilometres. This recently led to the development of ultrashort light detection and ranging (LIDAR) facilities, which exploit the white-light emitted by these filaments, in order to detect and identify several pollutants within a single laser shot.

Many applications have been inspired by this ultrafast ‘light bullet’. Although a couple of comprehensive reports were recently published in this field (Chin *et al* 2005, Couaïron and Mysyrowicz 2007), the theoretical foundations of these unique structures of light and their universal features still deserve to be exposed, which justifies the present review. An accurate understanding of the filamentation phenomenon requires a rigorous derivation of the propagation equations together with basic tools for capturing the underlying physics. For this purpose, section 2 addresses the model describing the long range propagation of ultrashort laser pulses in any optically transparent medium. Section 3 reviews the phenomenon of wave self-focusing and its limitation by potential players such as plasma generation, chromatic dispersion and optical nonlinearities. Emphasis is given to semi-analytic methods providing qualitative information about these effects. Section 4 lists the major phenomena driving femtosecond filaments. Section 5 is devoted to pulse shortening that can be achieved by letting femtosecond pulses ionize atom gases at appropriate pressures and to high-order harmonic generation. Section 6 addresses different propagation regimes in condensed materials (water, silica glasses), from the laser-induced breakdown limit to nonlinear waves self-guided with no plasma generation and their characteristic angle-frequency spectra. Section 7 concentrates on the atmospheric applications of the white-light supercontinuum emitted by ultrashort filaments. Current techniques for changing their onset distance and self-channeling length are discussed, together with the diagnostics used for plasma and optical-field measurements. Attention is paid to novel ultrashort LIDAR-based setups and their use in remotely analyzing aerosols, biological agents and dense targets through remote filament-induced breakdown spectroscopy. Their ability to trigger and guide electric discharges over several metres is also discussed. Section 8 summarizes the principal aspects of this review and presents future prospects. For an easier reading, the abbreviations employed in this article are spelt out in [appendix A](#).

## 2. Propagation equations

To start with, we derive the model describing the propagation of ultrashort optical pulses in transparent media. Using the conventional description of nonlinear optics, straightforward combination of the Maxwell’s equations yields (Agrawal 2001, He and Liu 1999, Shen 1984)

$$\nabla^2 \vec{E} - \vec{\nabla}(\vec{\nabla} \cdot \vec{E}) - c^{-2} \partial_t^2 \vec{E} = \mu_0 (\partial_t^2 \vec{P} + \partial_t \vec{J}), \quad (1a)$$

$$\vec{\nabla} \cdot \vec{E} = (\rho - \vec{\nabla} \cdot \vec{P})/\epsilon_0, \quad (1b)$$

where  $\epsilon_0$ ,  $\mu_0$  and  $c$  denote the electric permittivity, magnetic permeability and the speed of light in vacuum, respectively. The optical electric field  $\vec{E}$ , the polarization vector  $\vec{P}$ , the carrier density  $\rho$  and the current density  $\vec{J}$  are real valued. For further convenience, we introduce standard Fourier transforms applied to the fields  $(\vec{E}, \vec{P}, \vec{J})^\dagger$  as

$$(\hat{\vec{E}}, \hat{\vec{P}}, \hat{\vec{J}})^\dagger(\vec{r}, \omega) \equiv \frac{1}{2\pi} \int (\vec{E}, \vec{P}, \vec{J})^\dagger(\vec{r}, t) e^{i\omega t} dt. \quad (2)$$

The current density  $\vec{J}$  describes the motions of the free electrons created by ionization of the ambient atoms, for which ion dynamics is discarded. The polarization vector  $\vec{P}$  describes the bounded electron response driven by the laser radiation. It is usually decomposed into a linear part  $\vec{P}_L \equiv \vec{P}^{(1)}$  related to the first-order susceptibility tensor  $\overset{\leftrightarrow}{\chi}^{(1)}$  and a nonlinear one  $\vec{P}_{NL}$

satisfying  $|\vec{P}^{(1)}| \gg |\vec{P}_{\text{NL}}|$ . For isotropic, homogeneous, nonmagnetizable media and spectral ranges far from any material resonance,  $\vec{P}$  can be expressed as a power series in  $\vec{E}$ :

$$\hat{\vec{P}} = \hat{\vec{P}}^{(1)}(\vec{r}, \omega) + \hat{\vec{P}}^{(3)}(\vec{r}, \omega) + \hat{\vec{P}}^{(5)}(\vec{r}, \omega) + \dots \quad (3)$$

with scalar components

$$\begin{aligned} \hat{P}_{\mu}^{(j)} = \epsilon_0 \sum_{\alpha_1 \dots \alpha_j} \int \dots \int \chi_{\mu\alpha_1 \dots \alpha_j}^{(j)}(-\omega_\sigma; \omega_1, \dots, \omega_j) \\ \times \hat{E}_{\alpha_1}(\vec{r}, \omega_1) \dots \hat{E}_{\alpha_j}(\vec{r}, \omega_j) \delta(\omega - \omega_\sigma) d\omega_1 \dots d\omega_j, \end{aligned} \quad (4)$$

where  $\omega_\sigma = \omega_1 + \dots + \omega_j$ . All susceptibility tensors  $\chi^{(j)}$  with even index  $j$  vanish due to inversion symmetry. The subscript  $\mu$  indicates the field vector component in Cartesian coordinates and the indices  $\alpha_j$  have to be summed up over  $x, y$  and  $z$ . The tensor  $\chi^{\leftrightarrow(1)}$  is diagonal with  $\chi_{\mu\alpha}^{(1)} = \chi^{(1)} \delta_{\mu\alpha}$ , so that

$$\hat{\vec{P}}^{(1)}(\vec{r}, \omega) = \epsilon_0 \chi^{(1)}(\omega) \hat{\vec{E}}(\vec{r}, \omega), \quad (5)$$

and the scalar dielectric function, defined by

$$\epsilon(\omega) = 1 + \chi^{(1)}(\omega), \quad (6)$$

enters the wave number of the electromagnetic field  $k(\omega) = \sqrt{\epsilon(\omega)}\omega/c$ . Since  $\chi^{(1)}$  is complex-valued, the dielectric function  $\epsilon(\omega)$  contains all information not only about the material dispersion but also about the linear losses given by the imaginary part of  $\chi^{(1)}(\omega)$ . When losses are negligible,  $\epsilon(\omega)$  is real and reduces to  $\epsilon(\omega) = n^2(\omega)$ , where  $n(\omega)$  here denotes the linear refractive index of the medium, which can be described in certain frequency ranges (far from resonances) by, e.g. a Sellmeier formula. By convention,  $n_0 \equiv n(\omega_0)$  for the central frequency  $\omega_0 = 2\pi c/\lambda_0$  of a laser operating at the wavelength  $\lambda_0$  and  $k_0 \equiv k(\omega_0)$ . Without any specification,  $\omega = 2\pi c/\lambda$ ,  $w_\perp = 2\pi/k_\perp$  is the waist of the optical wave-packet in the plane  $(x, y)$  and  $k_\perp$  is the corresponding extent in the transverse Fourier space.

### 2.1. Helmholtz equation

By Fourier transformation, equations (1a) and (1b) express as the Helmholtz equation

$$[\partial_z^2 + k^2(\omega) + \nabla_\perp^2] \hat{\vec{E}} = -\mu_0 \omega^2 \hat{\vec{\mathcal{F}}}_{\text{NL}} + \vec{\nabla}(\vec{\nabla} \cdot \hat{\vec{E}}), \quad (7a)$$

$$\vec{\nabla} \cdot \hat{\vec{E}} = (\epsilon_0 \epsilon)^{-1} (\hat{\rho} - \vec{\nabla} \cdot \hat{\vec{P}}_{\text{NL}}), \quad (7b)$$

where  $\nabla_\perp^2 \equiv \partial_x^2 + \partial_y^2$  stands for transverse diffraction and

$$\hat{\vec{\mathcal{F}}}_{\text{NL}} \equiv \hat{\vec{P}}_{\text{NL}} + i\hat{J}/\omega \equiv \hat{F} \otimes \hat{\vec{E}} \quad (8)$$

gathers all nonlinear contributions through the function  $F$ . This function depends on  $\vec{E}$  and can be viewed as the effective nonlinear refractive index change of the medium ( $\otimes$  is the convolution operator). Because equations (7a) and (7b) are usually difficult to integrate in the full space-time domain, assumptions are required to simplify them into a more tractable form. The most fundamental of those consists of supposing that the wavefield keeps a transverse extension always fulfilling

$$k_\perp^2/k^2(\omega) \ll 1, \quad (9)$$

i.e. for  $k(\omega)$  located around  $\omega_0$ , the transverse waist of the beam has dimensions larger than the central wavelength. The second one assumes small nonlinearities:

$$\frac{\hat{F}}{\epsilon_0 \epsilon(\omega)} \ll 1. \quad (10)$$

**2.1.1. From vectorial to scalar description.** The previous conditions make vectorial effects negligible for, e.g. a transversally polarized light field  $E_\perp = (E_x, E_y)$ . Indeed, equations (7a) and (7b) can be combined, with the help of the continuity equation  $\partial_t \rho + \vec{\nabla} \cdot \vec{J} = 0$  expressed in Fourier variable, into the form

$$[\partial_z^2 + k^2(\omega) + \nabla_\perp^2] \hat{E} = -\mu_0 \omega^2 \left[ \hat{\mathcal{F}}_{\text{NL}} + \frac{\vec{\nabla}(\vec{\nabla} \cdot \hat{\mathcal{F}}_{\text{NL}})}{k^2(\omega)} \right]. \quad (11)$$

The last term scrambles nonlinear vectorial components. When we project the vectors  $\vec{E} = (\vec{E}_\perp, E_z)^\dagger$ ,  $\vec{P}_{\text{NL}} = (\vec{P}_{\text{NL}}^\perp, P_{\text{NL}}^z)^\dagger$ ,  $\vec{J} = (\vec{J}_\perp, J_z)^\dagger$  and  $\vec{\nabla} = (\vec{\nabla}_\perp, \partial_z)^\dagger$  onto the transverse and longitudinal axis,  $\hat{E}_z$  is found to scale as  $O(k_\perp/k)$ . This follows from a direct Fourier transform of equation (7b) for weak nonlinearities (equation (10)). Expressed in Fourier space, the nonlinear coupling of transverse/longitudinal components described by the scrambling term behaves as  $O(k_\perp^2/k^2)$  (Fibich and Ilan 2001a, 2001b, Milsted and Cantrell 1996). So these effects become important in the limit  $k_\perp \rightarrow k(\omega)$  only. Conversely, if the nonlinear compression processes are stopped *before*  $k_\perp$  becomes comparable with  $k$ , the last term in the right-hand side (RHS) of (11) is close to zero and the field remains transversally polarized. Hence, as long as the nonlinear polarization and current density preserve conditions (9) and (10), vectorial effects can be ignored for purely optical or weakly ionized materials as well. This property justifies the use of a scalar description for linearly polarized beams having, e.g.  $E_y = 0$ .

**2.1.2. Weak backscattering.** The question of evaluating backscattering waves may be crucial in several areas, such as remote sensing (Kasparian *et al* 2003, Yu *et al* 2001), which spectrally analyze the photons returning towards the laser source. The amount of backscattered photons, however, constitutes a weak percentage of those traveling in the forward direction through a transparent medium. The reason can be seen from the scalar version of equation (11) expressed as

$$D_+(\omega) D_-(\omega) \hat{E} = -\nabla_\perp^2 \hat{E} - \mu_0 \omega^2 \hat{F} \otimes \hat{E}, \quad (12)$$

where  $D_\pm(\omega) \equiv \partial_z \mp ik(\omega)$ . By substituting the solution  $\hat{E} = \hat{U}_+ e^{ik(\omega)z} + \hat{U}_- e^{-ik(\omega)z}$ , equation (12) expands as

$$e^{2ik(\omega)z} [\partial_z^2 + 2ik(\omega)\partial_z + \nabla_\perp^2 + \mu_0 \omega^2 \tilde{F}] \hat{U}_+ + [\partial_z^2 - 2ik(\omega)\partial_z + \nabla_\perp^2 + \mu_0 \omega^2 \tilde{F}] \hat{U}_- = 0. \quad (13)$$

Here,  $\hat{U}_+$  and  $\hat{U}_-$  represent the Fourier components of the forward and backward running fields, for which we *a priori* assume  $|\partial_z U_\pm| \ll |k(\omega) U_\pm|$  and  $U_+ \gg U_-$ . For technical convenience, we consider  $\hat{F} = \tilde{F} \delta(\omega)$ . Following Fibich *et al* (2002), we can integrate equation (13) over the interval  $z - \pi/2k \leq z \leq z + \pi/2k$  (one fast oscillation) and Taylorize  $\hat{U}_\pm(z)$  to evaluate

$$2ik(\omega) \partial_z \hat{U}_- \sim -\frac{e^{2ik(\omega)z}}{2ik(\omega)} \partial_z [\nabla_\perp^2 + \mu_0 \omega^2 \tilde{F}] \hat{U}_+. \quad (14)$$

Since  $\nabla_\perp^2 \sim -k_\perp^2$  in Fourier space, the backscattered component has a weak influence on the beam dynamics if  $k_\perp^2 \ll k^2(\omega)$  and as long as the longitudinal variations of the nonlinearities remain small.

**2.1.3. Unidirectional pulse propagation.** Because the propagation physics is mainly brought by the forward component, one has  $\hat{U}_- \rightarrow 0$  and  $\hat{E} \sim \hat{U}_+ e^{ik(\omega)z}$ . With the above approximations, the operator  $D_-(\omega)$  for backscattering mainly applies to the most rapid

variations of the field driven by the complex exponential, i.e.  $D_-(\omega)\hat{E} \approx 2ik(\omega)\hat{E}$ . The so-called ‘forward Maxwell equation’ (FME)

$$\partial_z \hat{E} = \frac{i}{2k(\omega)} \nabla_\perp^2 \hat{E} + ik(\omega)\hat{E} + \frac{i\mu_0\omega^2}{2k(\omega)} \hat{\mathcal{F}}_{\text{NL}} \quad (15)$$

then naturally emerges from equation (12). The validity of this model explicitly requires that the second-order derivative in  $z$  of the envelope function  $\hat{U}_+$  must be small compared with  $|k(\omega)\partial_z \hat{U}_+|$ , since  $D_+(\omega)D_-(\omega)\hat{E} = e^{ik(\omega)z}[\partial_z^2 + 2ik(\omega)\partial_z]\hat{U}_+$  (Geissler *et al* 1999, Husakou and Herrmann 2001). This approximation, usually expressed as  $|\partial_z \hat{U}_+| \ll |k(\omega)\hat{U}_+|$ , refers to the ‘paraxiality’ assumption. It holds if the field envelope  $U_+$  does not significantly change over propagation distances of the order of  $\lambda$ , for all wavelengths under consideration. Paraxiality is again linked to the weakness of both the ratio  $k_\perp/k$  and the nonlinearities. Let us indeed assume the nonlinear function  $F$  clamped at a maximal constant level,  $F_{\text{max}}$ . The forward component of equation (13) then reads

$$\hat{U}_+ \sim e^{ik(\omega)z} \left[ \sqrt{1 - \frac{k_\perp^2}{k^2(\omega)} + \frac{\mu_0\omega^2}{k^2(\omega)} F_{\text{max}}} - 1 \right]. \quad (16)$$

It is seen right away that this solution fits that of the paraxial model,  $\hat{U}_+ \sim e^{-i(k_\perp^2 - \mu_0\omega^2 F_{\text{max}})z/2k(\omega)}$ , as long as the two constraints (9) and (10) apply.

Alternatively, Kolesik *et al* (2002) derived a propagation model from the superposition of electromagnetic modal fields applied to the starting Maxwell equations. The resulting model only assumes that the nonlinear responses are mainly given by their projection onto the forward-propagating half of the plane-wave space. Without dwelling upon details, a brief construction of this model, known as the ‘unidirectional pulse propagation equation’ (UPPE), can be sketched by rewriting equation (12) as

$$D_+^\perp(\omega)D_-^\perp(\omega)\hat{E} = -\mu_0\omega^2 \hat{\mathcal{F}}_{\text{NL}}, \quad (17)$$

with  $D_\pm^\perp(\omega) \equiv (\partial_z \mp i\sqrt{k^2(\omega) + \nabla_\perp^2})$ . If we retain the forward running component  $\hat{E} = \hat{U}_+ e^{i\sqrt{k^2(\omega) + \nabla_\perp^2}z}$  constrained to the unidirectional assumption  $D_-^\perp(\omega)\hat{E} \approx 2i\sqrt{k^2(\omega) + \nabla_\perp^2}\hat{E}$ , the UPPE expresses in scalar form

$$\partial_z \hat{E} = i\sqrt{k^2(\omega) + \nabla_\perp^2} \hat{E} + \frac{i\mu_0\omega^2 \hat{\mathcal{F}}_{\text{NL}}}{2\sqrt{k^2(\omega) + \nabla_\perp^2}}. \quad (18)$$

Equation (18) allows to describe dc-field components ( $\omega = 0$ ), whereas equation (15) is strictly limited to nonzero frequencies. Despite these minor differences, models (15) and (18) become quite analogous when the condition  $k_\perp^2/k^2 \ll 1$  applies. Their major advantage is to elude the formal use of a central optical frequency and correctly describe the complete spectrum of pulses in nonlinear regimes, even when they develop very large bandwidths. More details about the relative accuracy of these models can be found in Kolesik and Moloney (2004a).

For practical use, it is convenient to introduce the complex version of the electric field

$$E = \sqrt{c_1}(\mathcal{E} + \mathcal{E}^*), \quad \mathcal{E} = \frac{1}{\sqrt{c_1}} \int \Theta(\omega) \hat{E} e^{-i\omega t} d\omega, \quad (19)$$

where  $c_1 \equiv \omega_0\mu_0/2k_0$  and  $\Theta(x)$  denotes the Heaviside function. Because  $\mathcal{E}$  satisfies  $\hat{\mathcal{E}}^*(\omega) = \hat{\mathcal{E}}(-\omega)^*$  (\* means complex conjugate), it is then sufficient to treat the FME model (15) in the frequency domain  $\omega > 0$  only. The field intensity can be defined by  $E^2$  averaged over an optical period at least, for a given central frequency  $\omega_0$ . This quantity usually follows from the modulus of the time averaged Poynting vector. It is expressed in  $\text{W cm}^{-2}$  and with the above normalization factor  $c_1$  it is simply given by the classical relation  $I = |\mathcal{E}|^2$ .



**2.1.4. Envelope description.** When a central frequency  $\omega_0$  is imposed, equation (15) restitutes the nonlinear envelope equation (NEE), earlier derived by Brabec and Krausz (1997). We can make use of the Taylor expansion

$$k(\omega) = k_0 + k'\bar{\omega} + \hat{\mathcal{D}}, \quad \hat{\mathcal{D}} \equiv \sum_{n \geq 2}^{+\infty} \frac{k^{(n)}}{n!} \bar{\omega}^n, \quad (20)$$

where  $\bar{\omega} = \omega - \omega_0$ ,  $k' = \partial k / \partial \omega|_{\omega=\omega_0}$  and  $k^{(n)} = \partial^n k / \partial \omega^n|_{\omega=\omega_0}$  and develop equation (15) as

$$\partial_z E = \int \left[ \frac{i \nabla_\perp^2}{2k(\omega)} + i(k_0 + k'\bar{\omega} + \hat{\mathcal{D}}) \right] \hat{E}(\omega) e^{-i\omega t} d\omega + i \frac{\mu_0}{2} \int \frac{\omega^2}{k(\omega)} \hat{\mathcal{F}}_{\text{NL}}(\omega) e^{-i\omega t} d\omega. \quad (21)$$

$\hat{E}(\omega)$  is the Fourier transform of  $E(t)e^{i\omega_0 t}$  in  $\bar{\omega}$ , so that  $\bar{\omega}$  corresponds to  $i\partial_t$  applied to the field envelope by inverse Fourier transform. Terms with  $k(\omega)$  in their denominator are expanded up to first order in  $\bar{\omega}$  only. Furthermore, we introduce the complex-field representation

$$\mathcal{E} = U e^{ik_0 z - i\omega_0 t}, \quad (22)$$

involving the novel envelope function  $U$ . Next, the new time variable  $t \rightarrow t - z/v_g$  can be utilized to replace the pulse into the frame moving with the group velocity  $v_g = k'^{-1}$ . Equation (21) then restores the NEE model

$$(i\partial_z + \mathcal{D})U \simeq -\frac{T^{-1}}{2k_0} (\nabla_\perp^2 U) - \frac{\mu_0 \omega_0^2}{2k_0 \sqrt{c_1}} T \mathcal{F}_{\text{NL}}^{\text{env}}(U), \quad (23)$$

where

$$\mathcal{D} \equiv \sum_{n \geq 2}^{+\infty} (k^{(n)} / n!) (i\partial_t)^n, \quad T = \left( 1 + \frac{i}{\omega_0} \partial_t \right), \quad (24)$$

whenever  $|k_0 - \omega_0 k'| / k_0 \ll 1$ . This condition is met if the difference between group and phase velocity relative to the latter is small, which is fulfilled in a wide range of propagation phenomena. The operator  $T^{-1}$  introduces *space-time focusing* in front of the diffraction term  $[T^{-1}(\nabla_\perp^2 U)]$ . On the other hand, nonlinearities with the envelope function  $\mathcal{F}_{\text{NL}}^{\text{env}}(U)$  are also affected by the operator  $T$ , which refers to *self-steepening*. For dispersion relations truncated at finite orders  $n < +\infty$ , the NEE model applies to optical fields with sufficiently narrow spectral bandwidths. With full chromatic dispersion, it holds for describing light pulses down to the single cycle.

## 2.2. Nonlinear optical responses

We henceforth assume a linearly polarized field (along, e.g.  $\vec{e}_x$ ) and treat nonlinear effects within a scalar description. For centro-symmetric materials, only one relevant component of the tensor remains in the cubic contribution  $P^{(3)}$ , e.g.  $\chi^{(3)} = \chi_{xxxx}^{(3)}$  (Agrawal 2001). For simplicity, we may first consider  $\chi^{(3)}$  as keeping a constant value for a spectral domain centered around  $\omega_0$ . Equation (4) then simplifies with a single component, denoted  $\chi_{\omega_0}^{(3)}$ , and in the time domain one finds  $P^{(3)}(\vec{r}, t) = \epsilon_0 \chi_{\omega_0}^{(3)} E^3$ . This expression holds whenever we suppose an instantaneous response of the medium, which ignores the contribution of molecular vibrations and rotations to  $\chi^{(3)}$ . Strictly speaking, however, the phenomenon of Raman scattering comes into play when the laser field interacts with anisotropic molecules. This interaction can be schematized by a three-level system built from the rotational states of a molecule. The molecular scatterer has two rotational eigenstates, the ground state (level 1) with energy  $\hbar\Omega_1$  and an excited one (level 2) with energy  $\hbar\Omega_2$  where  $\hbar = 1.06 \times 10^{-34}$  Js and  $\Omega_m$  denotes the frequency of the state  $m = 1, 2, 3$ . Far above lies an electronic (or translational) state with energy

$\hbar\Omega_3 \gg \hbar\Omega_2 - \hbar\Omega_1$ . This molecule interacts with the laser field whose photon frequency  $\omega_0$  fulfills  $\Omega_{13}, \Omega_{23} \gg \omega_0 \gg \Omega_{21}$ , [ $\Omega_{nm} \equiv \Omega_n - \Omega_m$ ], such that state  $|3\rangle$  cannot be populated. Because of the definite parity of these molecular states, the dipole matrix element  $\mu_{12}$  associated with the transition  $|1\rangle \rightarrow |2\rangle$  via a single photon is null, so that the rotational state  $|2\rangle$  can only be excited via transition through a virtual state  $|3\rangle$  [ $\mu_{13} \simeq \mu_{23} \equiv \mu \neq 0$ ]. Following this path, a Stokes photon with energy  $\hbar\omega_s = \hbar\omega_0 - \hbar\Omega_{21}$  is emitted. The density matrix element associated with the states  $|1\rangle$  and  $|2\rangle$  is found to satisfy (Peñano *et al* 2003)

$$\partial_t \rho_{12} \simeq -\frac{\rho_{12}}{\tau_2} - i \frac{\mu^2 E^2}{\hbar^2 \Omega_{31}} e^{-it/\tau_1}, \quad (25)$$

where  $\tau_1 = 1/\Omega_{21}$  and  $\tau_2$  are the rotational and dipole dephasing times. The polarization vector  $P_{\text{Raman}} = \chi^{(1)}[\rho_{12}e^{i\omega_R t} + \text{c.c.}]E$  then provides the Raman response

$$P_{\text{Raman}} = \frac{2\chi^{(1)}\mu^2}{\Omega_{31}\hbar^2} E \int_{-\infty}^t e^{-\frac{t-t'}{\tau_2}} \sin\left(\frac{t-t'}{\tau_1}\right) E^2(t') dt', \quad (26)$$

which originates from nonresonant, nonlinear couplings.

Expressed in terms of the rescaled complex field  $\mathcal{E}$  (equation (19)) and with appropriate normalizations (Sprangle *et al* 2002), it completes the cubic polarization as

$$P^{(3)} = 2n_0 n_2 \epsilon_0 \sqrt{c_1} \int_{-\infty}^{+\infty} \bar{R}(t-t') |\mathcal{E}(t')|^2 dt' \mathcal{E} + 2n_0 n_2 \epsilon_0 \sqrt{c_1} (1-x_K) \mathcal{E}^3/3 + \text{c.c.}, \quad (27a)$$

$$\bar{R}(t) = (1-x_K)\delta(t) + x_K \Theta(t)h(t), \quad (27b)$$

$$h(t) = \frac{\tau_1^2 + \tau_2^2}{\tau_1 \tau_2} e^{-t/\tau_2} \sin(t/\tau_1), \quad (27c)$$

with the definition of the nonlinear refractive index  $n_2 = 3\chi_{\omega_0}^{(3)}/(4n_0^2 c \epsilon_0)$ . Here, contributions in  $O(\mathcal{E}^3)$  are retained to further describe third-harmonic generation. Expression (27a) possesses both retarded and instantaneous components in the ratio  $x_K$ . The instantaneous part  $\sim \delta(t)$  describes the response from the bound electrons upon a few femtoseconds or less. The retarded part  $\sim h(t)$  accounts for nuclear responses, in which fast oscillations in  $E^2$  give negligible contributions, as  $\tau_1$  and  $\tau_2$  exceed the optical period  $\sim \omega_0^{-1}$ .

The fraction of delayed Kerr depends on the molecular species under consideration. For air at 800 nm, Sprangle *et al* (2002) chooses  $\tau_1 \simeq 62$  fs,  $\tau_2 \simeq 77$  fs and  $x_K = 1/2$ . This choice is consistent with that proposed in experimental papers (Nibbering *et al* 1997, Ripoche *et al* 1997). When  $\tau_1 \sim \tau_2$ , the function  $h(t) \simeq (1/\tau_1)e^{-t/\tau_1}$  can also be used in the ratio  $x_K = 1/2$  (Chiron *et al* 1999). For condensed materials, the parameter ranges  $\tau_2/\tau_1 = 2-4$ ,  $\tau_2 = 30-50$  fs with  $x_K = 0.15-0.18$  have been suggested (Agrawal 2001, Zozulya *et al* 1999). Values of the nonlinear Kerr index  $n_2$  can be found in the literature (Gong *et al* 1998, Hellwarth *et al* 1990, Lehmeier *et al* 1985, Luo *et al* 1995, Nibbering *et al* 1997). Comprised between  $10^{-19} \text{ cm}^2 \text{ W}^{-1}$  for gases and  $10^{-16} \text{ cm}^2 \text{ W}^{-1}$  in dense media, they may, however, vary by a factor of the order of unity, depending on the procedure used for their evaluation (polarization spectroscopy, self- or cross-phase modulated spectra, time-resolved interferometry). They also depend on the laser wavelength and pulse durations at which measurements are performed.

Besides, the susceptibility tensor has nonlinear components  $\chi^{(j>3)}$  that satisfy the ordering (Boyd 1992, Shen 1984)

$$\frac{P^{(k+2)}}{P^{(k)}} = \frac{\chi^{(k+2)}}{\chi^{(k)}} \cdot \frac{E^{k+2}}{E^k} \approx \frac{|E|^2}{|E_{\text{at}}|^2}, \quad (28)$$

where  $E_{\text{at}} \simeq 3 \times 10^{10} \text{ V m}^{-1}$  is the characteristic atomic electric field strength with intensity  $I_{\text{at}} > 10^{14} \text{ W cm}^{-2}$ . Typically, the evaluation  $\chi^{(5)}/\chi^{(3)} \sim 10^{-12}$  holds for nonresonant interactions in, e.g. gases. Despite the lack of knowledge on the sign of  $\chi^{(5)}$  (Pan *et al* 1990), the quintic susceptibility is often expected to saturate Kerr focusing and has, therefore, a negative sign (Nurhuda *et al* 2002b). Since the ordering (28) suggests that  $\chi^{(j)}$  is rapidly decreasing with the order  $j$ , the Taylor series with respect to the electric field is truncated at the 5th order. Quintic polarization can be derived following the same procedure as above, with  $\chi^{(5)}$  assumed constant in the frequency domain. By developing  $E^5$  in terms of  $(\mathcal{E}, \mathcal{E}^*)$  (equation (19)), the quintic contribution of the polarization vector then expands as

$$P^{(5)} = -2n_0 n_4 \epsilon_0 \sqrt{c_1} \left( |\mathcal{E}|^4 + \frac{1}{2} |\mathcal{E}|^2 \mathcal{E}^2 + \frac{1}{10} \mathcal{E}^4 \right) \mathcal{E} + \text{c.c.}, \quad (29)$$

where  $n_4 = 5|\chi_{\omega_0}^{(5)}|/(4n_0^3 c^2 \epsilon_0^2)$ . On the whole, the total nonlinear polarization vector reads as

$$P_{\text{NL}} = P^{(3)} + P^{(5)}. \quad (30)$$

### 2.3. Plasma generation for singly charged ionization

When free electrons are created, they induce a current density  $\vec{J} = q_e \rho \vec{v}_e$ . This quantity depends on the electron charge  $q_e = -1.6 \times 10^{-19} \text{ C}$ , the electron density  $\rho$  and the electron velocity  $\vec{v}_e$ .  $\vec{J}$  is computed from the fluid equations (Esarey *et al* 1997, Sprangle *et al* 1996)

$$\partial_t \rho + \vec{\nabla} \cdot (\rho \vec{v}_e) = \mathcal{S}, \quad (31a)$$

$$\partial_t \vec{v}_e + (\vec{v}_e \cdot \vec{\nabla}) \vec{v}_e = \frac{q_e}{m_e} (\vec{E} + \vec{v}_e \times \vec{B}) - \nu_e \vec{v}_e - \mathcal{S} \vec{v}_e / \rho. \quad (31b)$$

Here,  $\mathcal{S}$  represents external plasma sources and  $\nu_e$  is the effective electron collision frequency. These equations can be combined to yield

$$\partial_t \vec{J} + \nu_e \vec{J} = \frac{q_e^2 \rho}{m_e} \vec{E} + \vec{\Pi}, \quad (32)$$

where

$$\vec{\Pi} = \frac{q_e}{m_e} \vec{J} \times \vec{B} - \frac{\vec{J}}{\rho q_e} (\vec{\nabla} \cdot \vec{J}) - (\vec{J} \cdot \vec{\nabla}) \vec{v}_e \quad (33)$$

represents ponderomotive forces acting on slowly varying time scales. This driving term admits envelope components containing gradients of the field intensity, radiation pressure due to electron collisions and changes in the electron density. Ponderomotive forces induce low plasma currents, which can in turn generate electromagnetic pulses (EMP) (Cheng *et al* 2001, 2002) and provide sources of coherent sub-THz radiation (Tzortzakis *et al* 2002). Numerical simulations (Peñano *et al* 2004, Sprangle *et al* 2004) have shown, however, that for 100 fs pulses reaching intensities of  $10^{14} \text{ W cm}^{-2}$  and free electron densities  $\rho \sim 10^{16} \text{ cm}^{-3}$  in the atmosphere, the efficiency conversion to EMP is of the order of  $10^{-9}$  with local intensities attaining only  $10 \text{ kW cm}^{-2}$ . In dielectrics, the plasma generates EMP intensities remaining about  $\sim \text{MW cm}^{-2}$  for laser intensities of  $\sim 10^{13} \text{ W cm}^{-2}$ . These ponderomotive terms can thus be ignored, as long as peak intensities are below  $10^{15} \text{ W cm}^{-2}$ . In this range, plasma density perturbations due to Langmuir wave oscillations and relativistic increase of the electron mass also have a negligible influence. Therefore,  $\Pi = 0$  in equation (32) and at the lowest order in  $\nu_e$ , the growth of the electron density is governed only by the source term  $\mathcal{S}$ :

$$\partial_t \rho = \mathcal{S} = W(I)(\rho_{\text{nt}} - \rho) + \frac{\sigma}{U_i} \rho I - f(\rho). \quad (34)$$

This equation involves photo-ionization processes with rate  $W(I)$ , collisional ionization with cross-section  $\sigma$  and a function describing electron recombination or attachment with neighboring ions denoted by  $f(\rho)$ . Here,  $\rho_{\text{nt}}$  and  $U_i$  are the density of neutral species and the ionization potential, respectively, while  $\rho \ll \rho_{\text{nt}}$ . Typically, the recombination function in gases has a quadratic dependence on  $\rho$ , so that  $f(\rho) = \beta_{\text{recomb}} \rho^2$  with  $\beta_{\text{recomb}} \text{ (cm}^3 \text{ s}^{-1}) \sim 2 \times 10^{-8}$  at electron temperatures  $T_e = 1 \text{ eV}$  (Mlejnek *et al* 1998a, Sprangle *et al* 2002, Tzortzakis *et al* 2000b). Recombination times belong to the nanosecond scale. In dielectrics, much shorter recombination times are involved ( $\tau_{\text{recomb}} = 50\text{--}150 \text{ fs}$ ) and the density linearly decreases as  $f(\rho) = \rho/\tau_{\text{recomb}}$  (Audebert *et al* 1994, Peñano *et al* 2005, Tzortzakis *et al* 2001d).

Besides, the electron collisional rate depends on the electron energy distribution function and temperature versus the ionization potential  $U_i$ . Assuming a Maxwellian distribution function for the electron velocity, this rate linearly varies like  $\sigma |\mathcal{E}|^2/U_i$ , as long as the electron thermal energy is small compared with  $U_i$ . Here,  $\sigma$  is the inverse bremsstrahlung cross-section (Lotz 1967a, 1967b). If we omit Ohmic heating, solving for the current density (32) leads by Fourier transformation to

$$\hat{\vec{J}} = \frac{q_e^2}{m_e(v_e^2 + \omega^2)}(v_e + i\omega)\widehat{(\rho \vec{E})}. \quad (35)$$

The current density term in equation (1a) transforms as

$$\mu_0 \partial_t \vec{J} \rightarrow \left[ -i \frac{\omega n_0 \sigma(\omega)}{c} + \frac{\omega_0^2}{c^2 \rho_c (1 + v_e^2/\omega^2)} \right] \widehat{(\rho \vec{E})}, \quad (36)$$

after introducing the critical plasma density

$$\rho_c \equiv \frac{\omega_0^2 m_e \epsilon_0}{q_e^2} \simeq \frac{1.11 \times 10^{21}}{\lambda_0^2 (\mu\text{m})} \text{ cm}^{-3}, \quad (37)$$

at which the laser wave number vanishes. The cross-section

$$\sigma(\omega) = \frac{q_e^2}{m_e \epsilon_0 n_0 c v_e (1 + \omega^2/v_e^2)} \quad (38)$$

then provides the frequency-dependent collisional rate. This expression was earlier derived for zero elastic collisions with ions by Kennedy (1995), Yablonovitch and Bloembergen (1972) and by Feit and Fleck (1974). Often linked to what is called the ‘Drude’ model, it determines energy losses by cascade ionization.

In equation (34),  $W(I)$  denotes the rate for photo-ionization. It is evaluated from perturbative theories valid as long as the electric field  $E$  is weaker than the atom field strength  $E_{\text{at}}$ . This rate has been rederived in appendix B, following Keldysh’s and Perelomov, Popov and Terent’ev (PPT)’s theories applying to atoms or dielectrics (crystals) (Keldysh 1965, Perelomov and Popov 1967, Perelomov *et al* 1966, 1967). To describe the ionization of complex atoms, PPT formula usually includes the so-called ADK coefficients (for Ammosov *et al* (1986)), originally established in the limit of high intensities. Optical field ionization theories stress two major limits bounded by the ‘adiabaticity’ Keldysh parameter,

$$\gamma = \omega_0 \frac{\sqrt{2m_e U_i}}{|q_e| E_p}, \quad (39)$$

namely, the limit for multiphoton ionization (MPI,  $\gamma \gg 1$ ) concerned with rather low intensities and the tunnel limit ( $\gamma \ll 1$ ) concerned with high intensities, from which the Coulomb barrier becomes low enough to let the electron tunnel out. Here,  $E_p$  denotes the peak optical amplitude. For simplicity, we ignore the phenomenon of above-threshold ionization

(Agostini *et al* 1979, Corkum *et al* 1989), through which the electron absorbs more kinetic energy than  $K\hbar\omega_0 - U_i$ . For laser intensities  $I = |\mathcal{E}|^2 < 10^{13} \text{ W cm}^{-2}$ , MPI characterized by the limit

$$\gamma \gg 1 \implies W(I) \rightarrow W_{\text{MPI}} = \sigma_K I^K \quad (40)$$

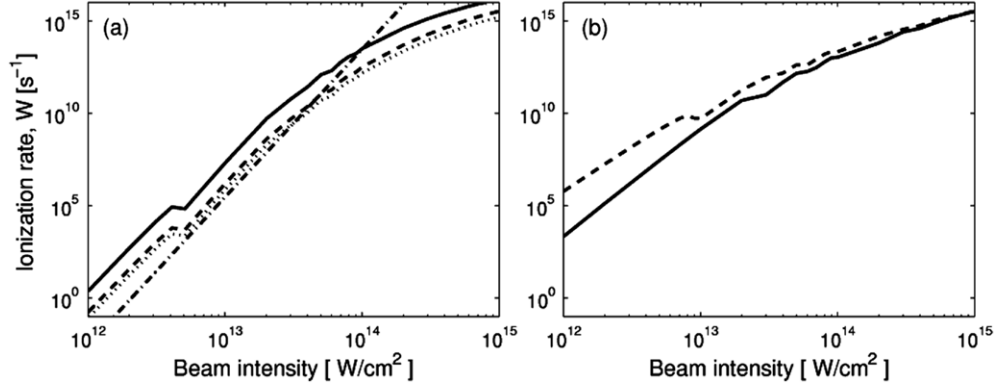
dominates, where  $K = \text{mod}(U_i/\hbar\omega_0) + 1$  is the number of photons necessary to liberate one electron. For higher intensities, tunnel ionization starts to contribute, i.e. electrons tunnel out within one optical cycle. Despite the complexity of ionization formulae, all of them exhibit common dependences on the laser field strength (Perry *et al* 1988b, Reiss 1980). By producing charged ions of noble gases as a function of the laser intensity, quantitative measurements confirmed the validity of Keldysh theory for singly charged ions only (Perry *et al* 1988a). This theory basically applies to hydrogen atoms and discards the effect of the Coulomb field of the residual ion on the outgoing electron. The PPT/ADK or Krainov's models (Krainov 1997), instead, better reproduce experimental ionization rates of atoms in, e.g. the tunnel regime and may even suit higher-charged states (Augst *et al* 1991, Cornaggia and Hering 2000). On this basis, ionization of diatomic molecules can be predicted through semi-empirical theories using the PPT rate in which the electron tunnels through a barrier with effective potential  $Z_{\text{eff}}/r$ . Here,  $Z_{\text{eff}}$  is determined by fitting the theoretical slope of the PPT formula onto measured ion signals. For ion signals collected from the interaction of  $\text{O}_2$  and  $\text{N}_2$  molecules with a 800 nm laser pulse,  $Z_{\text{eff}}$  is inferred from PPT applied to a corresponding atom (Xe atom) with ionization potential close to that of dioxygen molecules ( $U_i^{\text{O}_2} \simeq 12.1 \text{ eV}$ ,  $Z_{\text{eff}} = 0.53$ ) and to Ar atoms with  $U_i$  close to the energy gap of  $\text{N}_2$  molecules ( $U_i^{\text{N}_2} \simeq 15.6 \text{ eV}$ ,  $Z_{\text{eff}} = 0.9$ ) (Talebpour *et al* 1999). Differences in the effective residual charge number  $Z_{\text{eff}}$  originate from the 'suppressed' ionization of homonuclear diatomic molecules like  $\text{O}_2$ , that have active valence orbitals with antibonding symmetry. Suppression of  $\text{O}_2$  ionization turns out to be more than one order of magnitude. To take this property into account, models for the ionization dynamics can be improved by means of the many-body  $S$ -matrix theory applied to molecules (Muth-Böhm *et al* 2000). Alternatively, the PPT/ADK formula can be extended to  $\text{O}_2$  molecules by selecting the molecular coefficients of Tong *et al* (2002) within the so-called 'ADK molecular' ionization model (Nuter and Bergé 2006).

Figure 2 illustrates ionization rates for some of the previous theories applied to  $\text{O}_2$  molecules (figure 2(a)) or to fused silica (figure 2(b)). PPT and ADK molecular ionization rates plotted in the solid and dashed curves differ by only one decade. The dotted curve indicates the experimental fit from  $\text{O}_2^+$  signals with the PPT rate using  $Z_{\text{eff}} = 0.53$ . A good agreement is achieved between this fit and the ADK molecular ionization curve. Note that as long as the beam saturates below  $10^{13} \text{ W cm}^{-2}$ , the MPI limit alone can be retained. Beyond this intensity, the photo-ionization rate departs from the law  $\sigma_K I^K$  and must include tunnel contributions. To get qualitative behaviors only, the MPI rate may, however, be used at higher intensities, while keeping the interaction physics valid.

Because free carriers are first generated by photo-ionization, we must take the corresponding losses into account. Via energy conservation law, self-consistent expressions for these losses can be established. The temporal evolution of the energy density  $w$  is determined by a local version of the Poynting theorem, i.e.

$$\frac{d}{dt} w(\vec{r}, t) = \vec{J}(\vec{r}, t) \cdot \vec{E}(\vec{r}, t), \quad (41)$$

from which we can compute the energy lost by the pulse when it extracts electrons through the single ionization process (Kandidov *et al* 2003, Rae and Burnett 1992). The amount of energy per time and volume units is then given by  $\vec{J} \cdot \vec{E} = U_i \partial_t \rho_{\text{PI}}$ , where  $\partial_t \rho_{\text{PI}} \equiv W(I)(\rho_{\text{nt}} - \rho)$ .



**Figure 2.** (a) Ionization rate of O<sub>2</sub> molecules versus laser intensity obtained from the PPT theory (—), ADK molecular model (---), the fitting curve from PPT with  $Z_{\text{eff}} = 0.53$  (·····) (Talebpour *et al* 1999) and the MPI-like formulation (— · —) used in (Couairon *et al* 2002) at 800 nm. (b) Keldysh ionization rates for crystals applied to fused silica (solid curve,  $U_i = 7.8$  eV) and water (dashed curve,  $U_i = 7$  eV) at the same laser wavelength.

Using complex-valued fields, the current associated with photo-ionization losses is merely found to be

$$\vec{J}_{\text{loss}} = \sqrt{\frac{k_0}{2\omega_0\mu_0}} U_i \frac{W(I)}{I} (\rho_{\text{nt}} - \rho) (\vec{\mathcal{E}} + \vec{\mathcal{E}}^*). \quad (42)$$

Geissler *et al* (1999) derived similar losses by introducing the overall polarization vector for free electrons  $\vec{P} = q_e \rho_{\text{PI}} \vec{x}$ , so that  $\partial_t \vec{P} = q_e \dot{\rho}_{\text{PI}} \vec{x} + \vec{J}$ . Free electrons arise with zero velocity at the position  $\vec{x}(t) \simeq U_i \vec{E} / (2|q_e|I)$ , yielding the same loss current.

As a final result, the propagation equation within the FME description (15) reads in Fourier space as

$$\begin{aligned} \frac{\partial}{\partial z} \hat{\mathcal{E}} = & \left[ \frac{i}{2k(\omega)} \nabla_{\perp}^2 + ik(\omega) \right] \hat{\mathcal{E}} + \frac{i\mu_0\omega^2}{2k(\omega)\sqrt{c_1}} \Theta(\omega) \hat{P}_{\text{NL}} \\ & - \frac{ik_0^2 \Theta(\omega)}{2\epsilon(\omega_0)k(\omega)(1 + (v_e^2/\omega^2))} \left( \frac{\rho \hat{\mathcal{E}}}{\rho_c} \right) - \frac{\Theta(\omega)}{2} \sqrt{\frac{\epsilon(\omega_0)}{\epsilon(\omega)}} \mathcal{L}(\omega), \end{aligned} \quad (43)$$

where

$$\mathcal{L}(\omega) = \frac{U_i}{2\pi} \int \mathcal{E} \left[ \frac{W(I)}{I} (\rho_{\text{nt}} - \rho) + \frac{\sigma(\omega)}{U_i} \rho \right] e^{i\omega t} dt. \quad (44)$$

$P_{\text{NL}}(\vec{r}, t)$  (equation (30)) and the expression containing the electron density  $\rho(\vec{r}, t)$  (equation (34)) must be transformed to Fourier space. Treating the complex field  $\mathcal{E}$  only for positive frequencies is sufficient because of the symmetry  $\hat{\mathcal{E}}^*(\omega) = \hat{\mathcal{E}}(-\omega)^*$ , which imposes to select the parts of the nonlinear terms belonging to the frequency range  $\omega > 0$ .

Although the FME model (43) formally purports to describe ultrabroadband interactions, the nonlinear material models are mostly known at a single central frequency. This may be problematic when, e.g. correctly evaluating the nonlinear polarization vector for harmonics of the carrier wave. However, harmonic components emerge as a small fraction of the pump field, so that discrepancies linked to the accurate choice of the cubic susceptibility tensor should be limited. In addition, plasma generation is highly peaked around the frequency of the input pulse spectrum, so that satellite spectral modes do not significantly contribute to the production of

free electrons. This presupposes that the nonlinear response function keeps a dominant central component around  $\omega = \omega_0$ , which we henceforth assume. The collision cross-section  $\sigma$  is thus stated for a central frequency  $\omega_0$ . We furthermore apply the approximations  $v_e^2/\omega_0^2 \ll 1$  and  $\sqrt{\epsilon(\omega_0)}/\epsilon(\omega) \approx 1$ . The link to the NEE model is then straightforward, whenever the dispersion relation supports a Taylor expansion around  $\omega_0$ . By retaining only waveforms beating at  $\omega_0$ , the nonlinear envelope equation for the forward component  $U$  is directly inferred from (23) as

$$\begin{aligned} \frac{\partial}{\partial z} U = & \frac{i}{2k_0} T^{-1} \nabla_{\perp}^2 U + i \mathcal{D} U + i \frac{\omega_0}{c} n_2 T \left[ (1 - x_K) |U|^2 + x_K \int_{-\infty}^t h(t - t') |U(t')|^2 dt' \right] U \\ & - i \frac{\omega_0}{c} n_4 T |U|^4 U - i \frac{k_0}{2n_0^2 \rho_c} T^{-1} \rho U - \frac{\sigma}{2} \rho U - \frac{\beta_{\text{MPA}}(|U|)}{2} U, \end{aligned} \quad (45a)$$

$$\frac{\partial}{\partial t} \rho = W(I)(\rho_{\text{nt}} - \rho) + \frac{\sigma(\omega_0)}{U_i} \rho |U|^2 - f(\rho), \quad (45b)$$

where  $t$  stands for the retarded time variable  $t - z/v_g$ . The function  $\beta_{\text{MPA}}(|U|) = (\rho_{\text{nt}} - \rho) U_i W(I)/|U|^2$  accounts for losses caused by photo-ionization. In the MPI limit (40), this dissipative function takes the form  $\beta_{\text{MPA}}(|U|) \rightarrow \beta^{(K)} |U|^{2K-2}$  where  $\beta^{(K)} \equiv K \hbar \omega_0 \sigma_K \rho_{\text{nt}}$  is the coefficient for multiphoton absorption (MPA). The first term of the operator  $\mathcal{D}$  corresponds to group-velocity dispersion (GVD) with coefficient  $k'' = \partial^2 k / \partial \omega^2|_{\omega=\omega_0}$ . Equations (45a) and (45b) describe wave diffraction, Kerr focusing response, plasma generation, chromatic dispersion with a self-consistent action of deviations from the classical slowly varying envelope approximation through space-time focusing and self-steepening operators  $[(T^{-1} \nabla_{\perp}^2 \mathcal{E})$  and  $(T|\mathcal{E}|^2 \mathcal{E})$ , respectively]. They are usually integrated numerically by using, e.g. initially singly humped pulses taken with a super-Gaussian beam shape

$$U(x, y, z = 0, t) = U_0 e^{-\frac{r^2 N}{w_0^2} - i k_0 \frac{r^2}{2f} - \frac{t^2}{t_p^2} - i C \frac{t^2}{t_p^2}}, \quad (46)$$

which may be focused through a lens of focal length  $f$  and be temporally chirped if  $C \neq 0$ . Here,  $r = \sqrt{x^2 + y^2}$ . For Gaussian beams ( $N = 1$ ),  $U_0 = \sqrt{2P_{\text{in}}/\pi w_0^2}$  involves the input power  $P_{\text{in}}$ ,  $w_0$  is the beam waist and  $t_p$  the  $1/e^2$  pulse half-width, such that its full width at half maximum (FWHM) is  $\Delta t = \sqrt{2 \ln 2} t_p$ . The initial level ( $t = -\infty$ ) of plasma density is zero. In linear propagation, such Gaussian pulses diffract over the distance

$$z_f = (f^2/z_0)/(1 + f^2/z_0^2), \quad (47)$$

where  $z_0 = \pi n_0 w_0^2/\lambda_0$  is the diffraction range of the collimated beam ( $f = +\infty$ ). In nonlinear propagation, the interplay between all competitors in equations (45a) and (45b) severely alters beam diffraction and can maintain intense pulse components in self-guided state over longer distances. As an example, figure 3 shows the dynamics of the maximum fluence ( $\bar{F} = \int_{-\infty}^{+\infty} |\mathcal{E}|^2 dt$ ) for an unchirped, collimated Gaussian pulse with 0.9 and 0.45  $\mu\text{J}$  energies, input waist  $w_0 = 71 \mu\text{m}$ , half-width duration  $t_p = 42.5 \text{ fs}$  propagating in a 3 cm long silica sample. This beam is numerically simulated from the FME model (figure 3(a)) and the NEE including higher order dispersion up to  $n = 5$  (figure 3(b)). The ionization rate is delivered by the Keldysh's formula for crystals (figure 2(b)). Silica promotes strong chromatic dispersion, which is approximated by the NEE model, but not by FME that describes the full linear dispersion relation. Despite this difference, we can observe that the beam fluence remains identical according to both descriptions (43) and (45a). This property is true in several media (dielectrics, liquids and air as well), whenever equation (45a) includes dispersive contributions  $k^{(n)}$  with  $n > 3$  (Kolesik *et al* 2003b, 2002).

Earlier studies on femtosecond pulse propagation in the atmosphere started with simpler models than equations (43) or (45a) and (45b) by, e.g. ignoring time dispersion



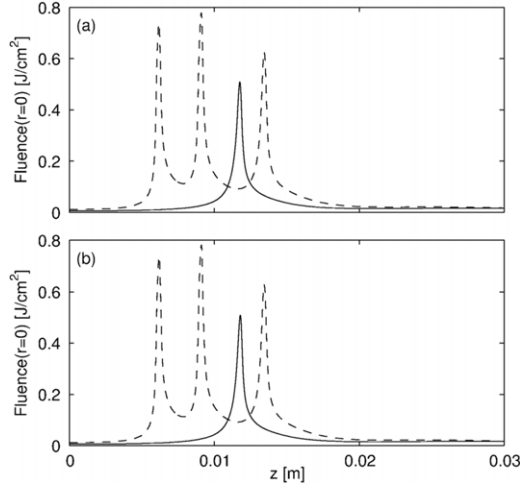


**Figure 3.** Maximum fluence for pulses propagating in silica glass with  $0.45 \mu\text{J}$  (—) and  $0.9 \mu\text{J}$  (---) energies simulated from (a) the FME model, (b) the NEE model with dispersion limited to fifth order.

(Kandidov *et al* 1994). Their derivation was improved later (Feng *et al* 1995, Mlejnek *et al* 1998a, 1998b, Sprangle *et al* 1996), before being finalized into NEE and FME formulations.

### 3. Optical ultrashort filaments: a few tools for their analytical description

#### 3.1. Kerr focusing and wave collapse

In the absence of temporal dispersion, equation (45a) with an instantaneous cubic Kerr term only,

$$\frac{\partial}{\partial z} U = \frac{i}{2k_0} \nabla_{\perp}^2 U + i \frac{\omega_0}{c} n_2 |U|^2 U = 0, \quad (48)$$

describes the self-focusing of optical beams when  $n_2 > 0$  (Askar'yan 1962, Marburger 1975). Self-focusing is a nonlinear phenomenon common to several branches of physics. In optics, it intervenes through the refractive index  $N_{\text{opt}} = n_0 + n_2 I$  that increases with the field intensity and forces light rays to refract onto the axis. This causes a compression of the beam in the diffraction plane, which leads to ‘wave collapse’ when the Kerr nonlinearity is not saturated. A necessary condition for the collapse is that the input power  $P_{\text{in}} = \int |\mathcal{E}|^2 d\vec{r}$  exceeds some critical value,

$$P_{\text{cr}} \simeq \frac{3.72 \lambda_0^2}{8\pi n_0 n_2}, \quad (49)$$

computed on the Townes mode (see below). The beam waist decreases more and more, as the field amplitude  $|U|$  diverges. Figure 4 illustrates the self-focusing principle taking place in purely Kerr media. The two insets detail the collapsing evolution of a Gaussian wave-packet with initial condition (46) at  $z = 0$  and near the collapse distance  $z_c$ . This distance, also termed as ‘nonlinear focus’, locates the point at which the beam amplitude diverges along the optical path. For purely Gaussian beams, it is given by the well-known semi-empirical Marburger



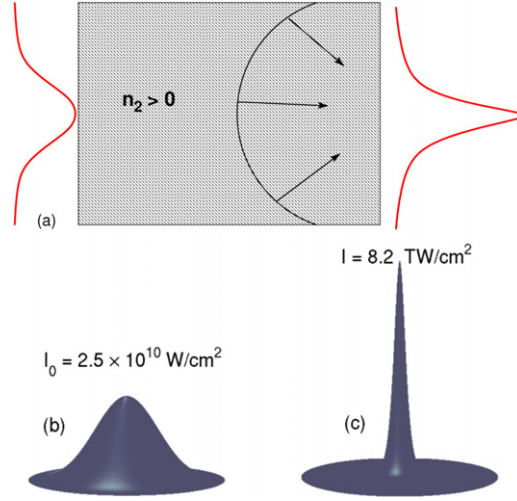


**Figure 4.** (a) Principle of wave self-focusing. Insets (b) and (c) detail some intensity profiles of the solution to equation (48), applied to silica ( $n_2 = 3.2 \times 10^{-16} \text{ cm}^2 \text{ W}^{-1}$ ). The initial condition is the Gaussian pulse (46) where  $f = +\infty$ ,  $w_0 = 130 \mu\text{m}$ ,  $P_{\text{in}}/P_{\text{cr}} = 3$ ,  $t_p = 85 \text{ fs}$  and  $C = 0$ .

formula (Marburger 1975)

$$z_c = \frac{0.367z_0}{\sqrt{\left(\sqrt{\frac{P_{\text{in}}}{P_{\text{cr}}}} - 0.852\right)^2 - 0.0219 + \frac{z_0}{f}}}. \quad (50)$$

Below we briefly review properties of wave collapse and how self-focusing is affected by temporal dispersion and plasma generation. In order to argue on the relevant mechanisms participating in this process, we discard non-resonant terms causing harmonic generation and consider an instantaneous cubic response ( $x_K = 0$ ). We apply the approximation  $T^{-1} \simeq 1 - (i/\omega_0)\partial_t$  supposing  $\omega_0 t_p \gg 1$ , neglect recombination and treat the plasma coupling term driven by MPI only and subject to the limit  $T^{-1} \rightarrow 1$ . Equations (45a) and (45b) are then rescaled in dimensionless form by using the substitutions  $r \rightarrow w_0 r$ ,  $t \rightarrow t_p t$ ,  $z \rightarrow 4z_0 z$ ,  $U \rightarrow \sqrt{c_2} \psi$  and  $\rho \rightarrow (n_0^2 \rho_c / 2z_0 k_0) \rho$ , where  $c_2 \equiv \lambda_0^2 / 8\pi^2 n_0 n_2 w_0^2$ . They result in the extended nonlinear Schrödinger (NLS) equation

$$i\partial_z \psi + \nabla_{\perp}^2 \psi + |\psi|^2 \psi + \mathcal{F}(\psi) = 0, \quad (51a)$$

$$\mathcal{F} = -\delta \partial_t^2 \psi - \rho \psi - \epsilon |\psi|^4 \psi + i\nu |\psi|^{2K-2} \psi + \frac{i(|\psi|^2 \psi - \nabla_{\perp}^2 \psi)_t}{t_p \omega_0}, \quad \partial_t \rho = \Gamma |\psi|^{2K}, \quad (51b)$$

where  $\mathcal{F}(\psi)$  includes GVD, MPI, nonlinear saturation, MPA and pulse steepening. GVD and MPA have the normalized coefficients  $\delta \equiv 2z_0 k'' / t_p^2$  and  $\nu = 2z_0 \beta^{(K)} c_2^{K-1}$ , respectively. Quintic saturation is taken into account through  $\epsilon = n_4 c_2 / n_2$ . The rescaled MPI coefficient reads as  $\Gamma = (2z_0 k_0 / n_0^2 \rho_c) \sigma_K \rho_{\text{nt}} t_p c_2^K$ .

**3.1.1. Principles of wave self-focusing.** With a purely cubic nonlinearity, solutions to the Cauchy problem (51a) can blow up (or collapse) at finite distance (Kelley 1965, Sulem and Sulem 1999). To describe this singular process, let us consider the NLS

equation (51a) with  $\mathcal{F} = \partial_t^2 \psi$  ( $\delta = -1$ ), so that the Laplacian  $\vec{\nabla}_\perp^2 \rightarrow \vec{\nabla}^2 = \partial_x^2 + \partial_y^2 + \partial_t^2 + \dots$  formally accounts for the dispersion of a wave-packet along  $D$  orthogonal spatial axes [ $\vec{r} = (x, y, t, \dots)$ ]. The wavefunction  $\psi$  evolves from the spatially localized initial datum  $\psi(\vec{r}, 0) \equiv \psi_0(\vec{r})$ , while it preserves the  $L^2$  norm (power)  $P$  and Hamiltonian  $H$ :

$$P = \int |\psi|^2 d\vec{r}, \quad H = \int (|\vec{\nabla}\psi|^2 - \frac{1}{2}|\psi|^4) d\vec{r}. \quad (52)$$

The following ‘virial’ equality can be established (Glassey 1977, Vlasov *et al* 1974)

$$P d_z^2 \langle r^2 \rangle = 4 \left\{ 2H + \left( 1 - \frac{D}{2} \right) \int |\psi|^4 d\vec{r} \right\}, \quad (53)$$

where  $\langle r^2 \rangle = \int r^2 |\psi|^2 d\vec{r} / P$  denotes the mean squared radius of the solution  $\psi$ . By a double integration in  $z$ , equation (53) shows that, whenever  $D \geq 2$ , there exist initial conditions for which  $\langle r^2 \rangle$  vanishes at finite distance, which is the sufficient signature of a wave collapse. For finite norms  $P$ , the inequality  $P \leq (2/D)^2 \langle r^2 \rangle \times \int |\vec{\nabla}\psi|^2 d\vec{r}$  implies that the gradient norm diverges in collapse regimes. As  $H$  is finite, the  $L^4$  norm and  $\max_r |\psi|$  diverge accordingly, which leads to a finite-distance blow-up (Kuznetsov 1996, Rasmussen and Rypdal 1986).

While  $H < 0$  arises as a sufficient condition for collapse, the gradient norm blows up in the critical case  $D = 2$ , only if  $P$  fulfills the constraint  $P > P_c$ . The critical power  $P_c = \int R^2 d\vec{r} = 11.68$  involves the radially-symmetric soliton solution, called the ‘Townes mode’, of  $-R + r^{-1} \partial_r r \partial_r R + R^3 = 0$  (Chiao *et al* 1964, Weinstein 1983). In the supercritical case  $D = 3$ , a criterion for collapse, sharper than  $H < 0$ , can be established as  $H < P_c^2 / P$  for gradient norms initially above  $3P_c^2 / P$  (Kuznetsov *et al* 1995). In that case,  $P_c$  again corresponds to the mass of the 3D soliton.

Once collapse is triggered, the solution focuses self-similarly near the singularity point  $z_c$  as (Rypdal *et al* 1985)

$$\psi(\vec{r}, z) = L^{-1}(z) \phi(\vec{\xi}, \xi) e^{i\lambda\xi + iLL_z\xi^2/4}, \quad (54)$$

where  $\vec{\xi} = \vec{r}/L(z)$ ,  $\xi(z) \equiv \int_0^z du/L^2(u)$  and the parameter  $\lambda$  is positive for making the new wavefunction  $\phi$  localized. The function  $L(z)$  represents the scale length that vanishes as collapse develops, and  $\phi$  converges to an exactly self-similar form  $\phi(\vec{\xi})$  fulfilling  $\partial_\xi \phi \rightarrow 0$ . The length  $L(z)$  is then identified from the continuity equation describing the mass exchanges between the core and tail parts of  $\psi$ , which can be determined through quasi-self-similar techniques (Bergé 1998). For  $D = 2$ ,  $L(z) \simeq L_0 \sqrt{z_c - z} / \sqrt{\ln \ln [1/(z_c - z)]}$  has a twice-logarithmic correction (Fraiman 1985, Landman *et al* 1988, Malkin 1990). The power  $P$  relaxes to the critical value  $P_c$  and stays mostly located around the center, which has also been reported experimentally (Moll *et al* 2003). For  $D = 3$ , the scaling law  $L(z) \simeq L_0 \sqrt{z_c - z}$  applies (Kosmatov *et al* 1991, LeMesurier 2000, Vlasov *et al* 1989, Zakharov and Kuznetsov 1986).

**3.1.2. Variational and perturbative approaches.** Because the cubic NLS equation is not integrable at dimension numbers  $D \geq 2$ , approximation methods describing the fate of singular solutions may be employed. Among these, ‘variational approaches’ consist of building a set of dynamical equations governing the size, amplitude and phase of the beam. These parameters are evaluated from functional integrals computed from a given trial function, which the pulse keeps along the optical path. Such methods only give global behaviors. Their principal drawback is that, as they need to fulfill the main conservation laws, they capture the entire initial mass of the solution and cannot evacuate radiation to the boundaries. This discrepancy may partly be cured by accounting for corrective damping

(Arévalo and Becker 2005, Kath and Smyth 1995), but improvements rapidly become tricky and limited. Variational principles applied to NLS solutions were extensively exploited in different contexts (Anderson and Bonnedal 1979, Cerullo *et al* 1996, Couairon 2003b, Desaix *et al* 1991, Esarey *et al* 1997, Karlsson *et al* 1992, Lehner and Auby 2000, Manassah 1992, Silberberg 1990, Sprangle *et al* 1996).

For example, considering the shape (46) with  $N = 1$ , a Gaussian trial function in the form

$$\psi = \frac{\sqrt{\mathcal{J}(z)}}{L(z)\sqrt{T(z)}} \phi(\xi_\perp, \eta) e^{i\frac{L_z L}{4} \xi_\perp^2 - i\frac{T_z T}{4\delta} \eta^2} \quad (55)$$

with  $\phi = e^{-\xi_\perp^2/2 - \eta^2/2 + i\theta(z)}$ ,  $\xi_\perp = r/L(z)$ ,  $\eta = t/T(z)$  can be employed in the virial identities governing the transverse and temporal mean squared extents of the solution to equations (51a) and (51b) (Bergé and Couairon 2000, Sprangle *et al* 2002). Coupled dynamical systems for the transverse width  $[L(z)]$ , the temporal duration  $[T(z)]$  and the intensity factor  $[\mathcal{J}(z)]$  yield qualitative behaviors for the propagation of a single femtosecond pulse preserving its cylindrical symmetry. This method, of course, cannot depict any temporal or spatial splitting phenomenon. However, it offers a global evolution of the beam intensity, which may support the comparison with (3+1)-dimensional numerical simulations (Champeaux and Bergé 2005).

Besides, perturbative methods provide information about the changes in the scale  $L$  induced by contributions that can stop the collapse. Here, the radial size  $L(z, t)$  tends to zero in the diffraction plane as  $z \rightarrow z_c$ , but it now depends on time. The principle is to perturb a collapsing state that naturally tends to the Townes mode  $R$ , by means of  $L^2$  orthogonal perturbative modes depending on  $\mathcal{F}$  (Fibich and Papanicolaou 1999). At the critical dimension, the zeroth-order collapsing solution, whose core converges as

$$\psi \rightarrow \psi_s = L^{-1} R(\vec{r}/L) \exp(i\zeta + iL_z r^2/4L), \quad (56)$$

has its mean radius  $L(z, t)$  modified by the perturbation  $|\mathcal{F}| \ll 1$ . Appropriate functions  $\mathcal{F}$  are then capable of turning the sign of  $\beta = -\frac{1}{4}L^3 L_{zz}$  from positive to negative, which predicts the arrest of collapse. This method was applied to many ‘perturbations’ of NLS (Fibich 1996, Fibich and Papanicolaou 1997, LeMesurier *et al* 2004, Schjødt-Eriksen *et al* 2001a). It was later extended to a variational system accounting for dissipative losses,  $\psi \rightarrow \sqrt{\mathcal{J}(z, t)}\psi_s$  (Bergé and Couairon 2001b). Applied to equations (51a) and (51b) for pulses having a Gaussian distribution in time, this procedure involves the substitution

$$\psi \rightarrow \sqrt{\mathcal{J}(z, t)}\psi_s; \quad \mathcal{J}(z = 0, t) = P_{\text{in}} e^{-2t^2}/P_{\text{cr}}, \quad (57)$$

and leads to the dynamical equations

$$\frac{M}{4P_c} L^3 L_{zz} = 1 - \mathcal{J} + 4\epsilon \frac{\mathcal{J}^2}{L^2} - \frac{L^2}{2P_c} \int R^2 \xi \partial_\xi \rho \, d\vec{\xi}, \quad (58a)$$

$$\frac{\mathcal{J}_z}{\mathcal{J}} \simeq 2\delta\zeta_{tt} - 2\nu A \frac{\mathcal{J}^{K-1}}{L^{2K-2}} - \frac{B(L^{-2})_t}{t_p \omega_0}, \quad (58b)$$

where  $M = \int \xi^2 R^2(\xi) \, d\vec{\xi}$ ,  $A = \int R^{2K} \, d\vec{\xi}/P_c$ ,  $B = 3\mathcal{J} + 1$  and  $C = \int R^{2K+2} \, d\vec{\xi}/P_c$ . In the right-hand side of equation (58b), the first term refers to GVD, the second one to MPA and the last term corresponds to pulse steepening. Below, equations (58a) and (58b) will be employed for extracting qualitative information about the generic features observed in the numerical simulations of the NEE model (45a) and (45b).

### 3.2. Saturation by temporal dispersion

By mixing GVD and spatial diffraction, the Kerr nonlinearity causes defocusing in time for  $k'' > 0$  (normal dispersion) and temporal compression for  $k'' < 0$  (anomalous dispersion).

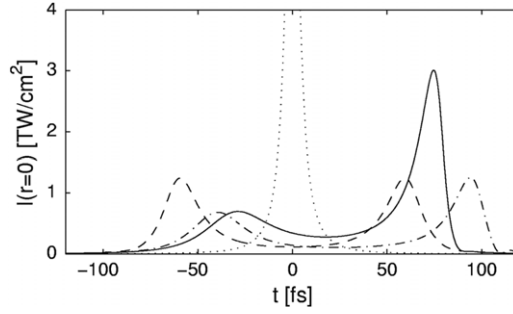


**Figure 5.** Temporal profiles of Gaussian pulses ( $w_0 = 130 \mu\text{m}$ ,  $t_p = 85 \text{ fs}$ ) near the nonlinear focus with power  $P_{\text{in}} = 3 P_{\text{cr}}$  for the Kerr response alone ( $\cdots$ ), for Kerr + normal GVD ( $---$ ), for Kerr + GVD +  $T$ ,  $T^{-1}$  ( $—$ ), for Kerr + GVD +  $T$ ,  $T^{-1}$  + higher order dispersion ( $- \cdot -$ ). In all cases, plasma response is omitted.

The interplay of these processes results in the symmetric splitting of the pulse along the time axis with normal GVD (Chernev and Petrov 1992a, 1992b) and to a 3D spatiotemporal collapse with anomalous GVD. In addition, when ultrashort pulses develop sharp temporal gradients, the operator  $T$  in front of the Kerr term (self-steepening) induces a shock dynamics: the field develops a singular profile with  $|\psi_t| \rightarrow +\infty$  in the trail ( $t > 0$ ) of the pulse (Anderson and Lisak 1983). This dynamics is reinforced by space-time focusing (Rothenberg 1992). Figure 5 depicts temporal profiles of pulses undergoing steepening effects in normally dispersive regime (silica glass at 790 nm), together with a transverse collapse.

To understand these dynamics, the pulse can be stacked along the temporal direction into different time slices each having its own power, e.g.  $P(t) = P_{\text{in}} e^{-2t^2}$ . Slices located at times  $t < 0$  correspond to the front (or leading) pulse; those at  $t > 0$  constitute the back (trailing) pulse. Each time slice self-focuses at its respective singularity point,  $z_c(t)$ , according to equation (50) in which the ratio  $P_{\text{in}}/P_{\text{cr}}$  must be replaced by  $P_{\text{in}} e^{-2t^2}/P_{\text{cr}}$ . This scenario is known as the ‘moving-focus’ model (Lugovoi and Prokhorov 1974, Shen 1976) and yields simple comprehension elements to figure out the pulse distortions. Here, the central time slice focuses at the shortest distance  $z_c(t = 0)$ . Furthermore,  $\dot{z}_c(t)$  is positive for  $t > 0$  and negative for  $t < 0$  [ $\dot{z}_c(0) = 0$ ], whereas  $\ddot{z}_c(t)$  always remains positive. Near the collapse distance, we can replace all time derivatives by  $\partial_t = -\dot{z}_c \partial_z$  (Fibich and Papanicolaou 1997, Luther *et al* 1994b). Power fluctuations (58b) are then given by

$$\frac{\mathcal{J}_z^{\text{disp}}}{\mathcal{J}} = 2\delta[-\ddot{z}_c/L^2 + \dot{z}_c^2(1/L^2)_z] + \frac{2B}{\omega_0 t_p} \dot{z}_c(L^{-2})_z, \quad (59)$$

where  $L_z < 0$  in compression regime. With  $\delta > 0$ , equation (59) describes defocusing around the central slice. Normal GVD transfers power towards nonzero instants, symmetrically located with respect to  $t = 0$ . Self-steepening and space-time focusing moreover produce a transfer of power from the leading ( $\dot{z}_c < 0$ ) to the trailing portion of the pulse ( $\dot{z}_c > 0$ ). This asymmetrizes the temporal profile, which was retrieved in experiments (Ranka and Gaeta 1998). Normal GVD alone ‘splits’ a focusing pulse into two regular, symmetric spikes at powers  $< 2P_{\text{c}}$ . For higher powers, the peak edges develop shock profiles and disintegrate into ripplelike cells (Fibich *et al* 2003, Germaschewski *et al* 2001). Due to the hyperbolic operator  $\nabla_{\perp}^2 - \delta \partial_t^2$ , one splitting event produces an  $X$ -shaped waveform in the  $(r, t)$  plane (Bergé *et al* 2002, Christodoulides *et al* 2004, Litvak *et al* 2000a, 2000b, Zharova *et al* 2003).

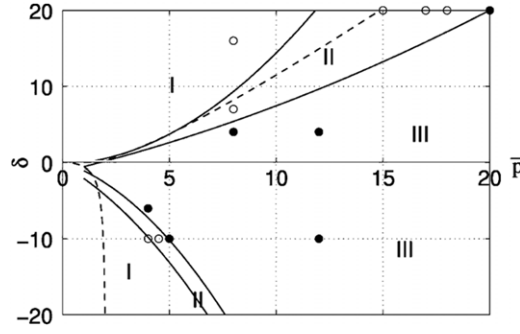


**Figure 6.** Collapse regions in the plane  $(\delta, \bar{p})$ . The solid curves extrapolate results from the propagation equations. The dashed curves represent theoretical limits estimated from equations (51a) and (51b), above which dispersion inhibits the self-focusing. Regions I, II and III are explained in the text.

Normal GVD ( $k'' > 0$ ) and plasma formation compete at powers moderately above critical to halt the wave collapse. The stronger the GVD coefficient, the larger the power interval in which the collapse is arrested by pulse splitting. A boundary  $\delta_{\text{crit}}(\bar{p})$ , function of the ratio of input power over critical  $\bar{p} = P_{\text{in}}/P_{\text{cr}}$ , can be calculated in such a way that initial conditions fulfilling  $\delta > \delta_{\text{crit}}(\bar{p})$  will limit the Kerr self-focusing through GVD splitting (Luther *et al* 1994a). Higher order dispersion together with steepening effects ( $T, T^{-1}$ ) modify this curve in the sense of shifting the self-focusing threshold to higher powers (Skupin and Bergé 2006, Skupin *et al* 2006a). In particular, third-order dispersion tends to delocalize the pulse by pushing the temporal centroid to the back (Fibich and Ilan 2004). In contrast, for anomalous GVD ( $k'' < 0$ ) power is transferred to the center, as seen from equation (59) with  $\delta < 0$ . Ultrashort pulses thus collapse both in space and time. A mapping  $|\delta| > \delta_{\text{crit}}(\bar{p})$  can again be constructed on the basis of virial-type arguments (Bergé and Skupin 2005). It predicts pulse spreading when the dispersion length  $\sim t_p^2/|k''|$  is short enough to prevail over diffraction and Kerr nonlinearity. As for normal GVD, the theoretical boundaries are modified by higher order dispersion and steepening terms.

Figure 6 summarizes the zone of collapse and no-collapse in the plane  $(\delta, \bar{p})$  for both normally and anomalously dispersive media computed from equations (45a) and (45b). Open circles represent initial conditions that do not collapse. Close ones result in a strong divergence of the beam intensity. Three zones clearly occur: (I) a dispersion-dominated domain leading to pulse spreading; (II) a transition zone in which GVD and steepening operators inhibit the self-focusing; (III) a Kerr-dominated region, in which chromatic dispersion is unable to stop the wave blow-up. Here, the field intensity can increase by several decades before reaching the ionization threshold.

### 3.3. Saturation by plasma defocusing

The action of MPI is to deplete the pulse temporal profile through the sudden emergence of an ionization front near the focus point  $z_c$ . In the absence of time dispersion and nonlinear losses, the plasma equation  $\partial_t \rho = \Gamma |\psi|^{2K}$  can be integrated with the ansatz (57) as

$$\rho(r, t, z) \simeq \sqrt{\frac{\pi}{8K}} \Gamma \left( \frac{P_{\text{in}}}{P_{\text{cr}}} R^2 \right)^K \frac{\text{Erf}(\sqrt{2K}t) + 1}{L^{2K}(z, t)}, \quad (60)$$

where  $\text{Erf}(x) = (2/\sqrt{\pi}) \int_0^x e^{-u^2} du$  denotes the error function. The last integral of equation (58a) is negative and can efficiently compete with the Kerr contribution as  $L \rightarrow 0$ . With the step function  $\text{Erf}(\sqrt{2K}t) + 1$ , the plasma response arises like a defocusing plateau, as the field intensity reaches its maximum. All time slices belonging to the interval  $t > 0$  are defocused. At negative times, the pulse continues to self-focus within a shorter temporal profile (Bergé and Couaïron 2001a, Henz and Herrmann 1999).

When GVD and MPA come into play, the leading peak becomes unstable and refocusing of the trail can occur. With MPA, the leading component is partly damped in the intensity ratio  $\mathcal{J}_z/\mathcal{J} \simeq -2\nu A(\mathcal{J}/L^2)^{K-1}$  (equation (58b)). Consequently, the electron density attains much lower levels and permits the emergence of a trail. This complex dynamics leads to two following signatures for plasma defocusing: (i) MPI shortens the pulse duration near the nonlinear focus; (ii) because  $\rho$  scales as  $R^{2K}$ , plasma defocusing takes place inside a narrow region ( $\sim 1/\sqrt{K}$  times the beam width) of the intensity distribution, which creates spatial rings. This ‘self-guiding’ mechanism is therefore not static. Certain pulse components are defocused to the benefit of the others. To clear this up, figure 7 depicts focusing/defocusing cycles affecting the peak intensity, electron density, beam radius and the distribution in space and time of a 150 fs pulse for atmospheric propagation. Note the rings formed just at the stage of plasma defocusing (figure 7(e)) and the occurrence of a sharp trail when steepening effects ( $T, T^{-1}$ ) are included (figure 7(d)).

### 3.4. Saturation by optical nonlinearities

Defocusing quintic nonlinearities produce stable solitons in continuous wave media (Gatz and Herrmann 1997, Malkin 1993, Trillo and Torruellas 2001, Vakhitov and Kolokolov 1975, Vidal and Johnston 1996), which is partly reflected by equation (58a) emphasizing an arrest of collapse like  $\beta = -\frac{1}{4}L^3 L_{zz} \sim -1/L^2$ .

Reframed in the present context, several papers addressed the question of limiting self-focusing by nonlinear optical saturations, instead of relying on plasma generation alone (Gaeta and Wise 2001, Koprinkov *et al* 2000, 2001). The impact of  $\chi^{(5)}$  susceptibility may vary with the pulse length, the ratio of instantaneous over delayed Kerr responses and the ionization sources. All influence the maximum intensity attained by the beam (Aközbek *et al* 2001, Couaïron 2003a, Vinçotte and Bergé 2004). Among those, the ionization rate is particularly important. For instance, figure 8 displays the peak intensities and electron density of a Gaussian pulse propagating in air (Nuter and Bergé 2006). One of the ionization models involves the ADK molecular rate without (dashed curve) and with (dotted curve) a weak quintic saturation ( $n_4 = 2.5 \times 10^{-33} \text{ cm}^4 \text{ W}^{-2}$ ). The measured intensity peak of  $5 \times 10^{13} \text{ W cm}^{-2}$  is refound in the latter configuration only. The  $\chi^{(5)}$  susceptibility lowers the peak intensity and density, which stays close to  $10^{16} \text{ cm}^{-3}$ . The self-guiding range is increased. Quintic nonlinearities can have a significant role when their own saturation level becomes comparable with the ionization threshold. To perform further quantitative comparisons, their characteristic coefficients should be accurately quantified. This knowledge is unfortunately missing in the literature.

Other high order effects may soften the Kerr focusing of nonlinear waves. For instance, the Raman response function in equations (27a), (27b) and (27c) becomes all the weaker as the pulse is short, which affects the critical power for self-focusing like  $P_{\text{cr}} \rightarrow P_{\text{cr}}/[1 - x_K + x_K G(t)]$  (Ting *et al* 2005a). Here, the function  $G(t)$  follows from computing the integral  $\int h(t-t')|\psi(t')|^2 dt' \sim G(t)|\psi|^2$  over the initial pulse profile. Unlike long pulses, for which  $G(t) \rightarrow 1$ , the non-instantaneous nonlinearity reduces the effective value of the Kerr index



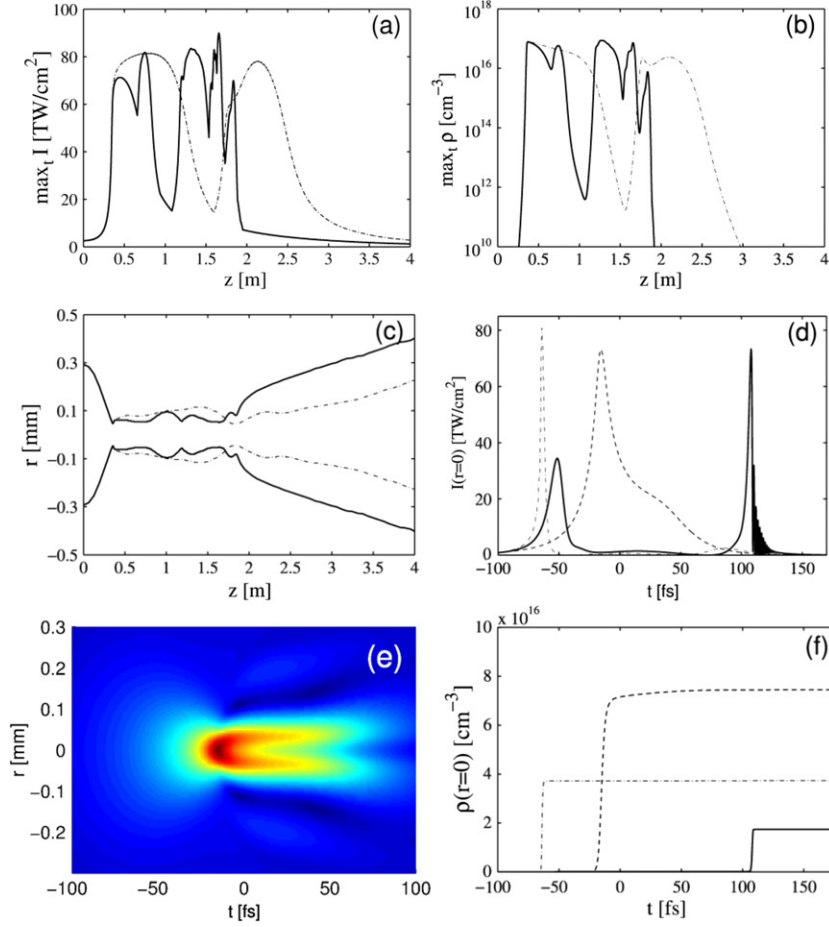


**Figure 7.** (a) Maximum intensity, (b) peak electron density and (c) mean radius (FWHM of the fluence) of a 150 fs, 0.5 mm-waisted Gaussian pulse with  $4P_{cr}$  in air at  $\lambda_0 = 800$  nm. Dash-dotted curves refer to the case when  $T, T^{-1} = 1$  and chromatic dispersion is limited to GVD ( $k'' = 0.2 \text{ fs}^2 \text{ cm}^{-1}$ ). Solid curves refer to the full model (45a). (d) Temporal profiles at  $z = 0.8$  m. The dashed curve refers to the distribution at  $z = 0.4$  m (identical for both models). (e) Radial profile versus time near  $z_c$ . (f) Plasma responses associated with (d).

and results in delaying the nonlinear focus from which a filament emerges (Aközbek *et al* 2001, Chiron *et al* 1999, Liu and Chin 2005).

Besides, the cubic polarization  $\sim E^3$  generates a third-order harmonic as

$$E \rightarrow U_\omega e^{ik(\omega)z - i\omega t} + \tilde{U}_{3\omega} e^{ik(3\omega)z - 3i\omega t} + \text{c.c.} \quad (61)$$

at  $\omega = \omega_0$  (Agrawal 2001). Two coupled equations can then be derived under the basic assumptions of slowly varying envelopes and narrow spectral bandwidths  $\Delta\omega_j/\omega_j \ll 1$  ( $j = \omega, 3\omega$ ). The coupling is insured by cross-phase modulation (XPM) and four-wave mixing (4WM) induced by the cubic nonlinearity. By substituting  $\tilde{U}_{3\omega} \rightarrow U_{3\omega} e^{i\Delta k z}$ , where  $\Delta k = 3k(\omega) - k(3\omega)$  is the linear wavevector mismatch parameter, the propagation equations read like equation (51a), where the function  $\mathcal{F}$  for the two components  $U_\omega$  and  $U_{3\omega}$  must be

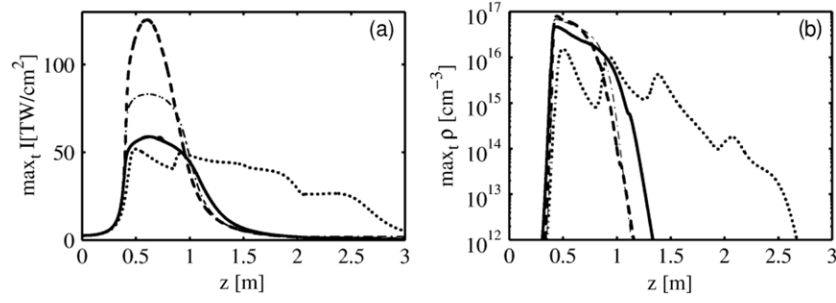


**Figure 8.** (a) Peak intensities and (b) electron densities for Gaussian pulses with  $w_0 = 0.5$  mm,  $t_p = 70$  fs,  $T = T^{-1} = 1$  and different ionization models: PPT (—), ADK molecular (---), ADK molecular +  $\chi^{(5)}$  susceptibility (.....) and the MPI-like approximation of figure 2 (— · —).

adapted as

$$\mathcal{F}_\omega \rightarrow \mathcal{F}_\omega + 2|\psi_{3\omega}|^2\psi_\omega + (\psi_\omega^*)^2\psi_{3\omega}, \quad (62a)$$

$$\mathcal{F}_{3\omega} \rightarrow \mathcal{F}_{3\omega} + 2|\psi_\omega|^2\psi_{3\omega} + \frac{\psi_\omega^3}{3} + \left( \frac{i\partial_t}{t_p\Delta v} - \Delta k \right) \frac{\psi_{3\omega}}{(4z_0)^{-1}}, \quad (62b)$$

which includes the group-velocity mismatch responsible for temporal walk-off,  $\Delta v = [v_g(3\omega)^{-1} - v_g(\omega)^{-1}]^{-1}$ . In self-focusing regimes, the intensity of the third harmonic (TH) usually contributes by a small percentage to the overall beam fluence (Aközbek *et al* 2002). Despite the smallness of the TH field, this component may act as a saturable nonlinearity for the pump component when  $\Delta k < 0$  and the term containing  $|\Delta k|$  has an order of magnitude comparable with the 4 WM and XPM terms,  $\psi_{3\omega} \sim -\psi_\omega^3/3(4z_0|\Delta k| + 2|\psi_\omega|^2)$ . Once inserted into the pump wave equation, this so-called ‘cascading’ limit (Buryak *et al* 1999) introduces a saturable quintic nonlinearity that lowers the peak intensity and can enhance the propagation (Bergé *et al* 2005).

So far, we have been dealing with linearly polarized waves. However, by writing the electric field as  $\mathcal{E} = (\mathcal{E}_x, \mathcal{E}_y)$ , each polarization component undergoes optical nonlinearities as

$$P_{NL} \sim |\psi_j|^2\psi_j + \frac{2}{3}|\psi_k|^2\psi_j + \frac{1}{3}\psi_j^2\psi_k^*, \quad (63)$$

with  $j, k = x, y$  ( $j \neq k$ ). A linearly polarized state is described by the single-component NLS equation with, e.g.  $\psi_y = 0$ . A circularly polarized state corresponds to the configuration  $\psi_y = \pm i\psi_x$ . In between, elliptically polarized states facilitate energy transfers through the phase-dependent terms  $\psi_j^2\psi_k^*/3$  from one orthogonal component to the other (Schjødt-Eriksen *et al* 2001b). These energy transfers increase the power threshold for self-focusing (Bergé *et al* 2003). For circular polarization, the collapse threshold for the total power  $P = \int (|\psi_x|^2 + |\psi_y|^2) d\vec{r}$  is increased by a factor 3/2 when passing from linearly- to circularly-polarized geometries. In addition, circular polarizations on femtosecond filaments self-channeling in the atmosphere produce stabler patterns than those issued from linear polarization (Kolesik *et al* 2001). They moreover weaken the MPI efficiency and decrease ion signals by a couple of decades in the fluorescence of  $N_2$  molecules collected from infrared pulses (Petit *et al* 2000).



### 3.5. Self-phase modulation and supercontinuum generation

The Kerr effect creates spectral broadening through self-phase modulation (SPM). Solving for  $i\partial_z\psi = -|\psi|^2\psi$  indeed yields the exact solution  $\psi = \psi_0 e^{i|\psi_0|^2 z}$ , which describes a self-induced phase modulation experienced by the optical field during its propagation. This intensity-dependent phase shift is responsible for spectral broadening by virtue of the relation  $\Delta\omega = -\partial_t \arg(\psi)$  (Agrawal 2001, Shen 1984). Because the frequency spectrum is expanded by the nonlinearity, SPM leads to supercontinuum generation and white-light emission. This elementary picture must, of course, be revised when plasma generation and pulse steepening come into play. With plasma generation, this phenomenon can be described by employing the following approximations in equations (51a) and (51b). First, we assume that the MPI response behaves like a static density plateau (see, e.g. figure 7(f)), so that the ratio  $\rho/|\psi|^2$  is either zero or close to unity. Second, for simplicity, we retain self-steepening to the detriment of space-time focusing, diffraction, GVD and MPA. By modeling the pulse with a sech-shaped profile, integration of the resulting equation yields the spectral broadening (Champeaux and Bergé 2003)

$$\frac{\Delta\lambda}{\lambda_0} \simeq 1 - \frac{\rho}{|\psi|^2} - \left[ 1 + \frac{Q^2 - 2Q \sinh(t)}{\cosh^2(t)} \right]^{-1/2}, \quad (64)$$

where  $Q \equiv z|\psi_0|^2/t_p\omega_0$  is linked to self-steepening. This expression is valid under the basic assumption  $\Delta\omega/\omega_0 = -\Delta\lambda/\lambda_0 \ll 1$ . As long as  $Q \ll 1$  and in the absence of MPI, variations in wavelength  $\Delta\lambda/\lambda_0 \approx -Q \sinh(t)/\cosh^2(t)$  represent the early symmetric broadening through SPM (Yang and Shen 1984). When MPI forms a defocusing plateau,  $\Delta\lambda/\lambda_0$  becomes larger in the region where  $\rho = 0$  (nondefocused leading pulse), than when  $\rho \rightarrow |\psi|^2$  (defocused trail). Consequently, as the beam reaches the first focus point  $z_c$ , the dominant part of the pulse is the front edge ( $\rho = 0$ ) and MPI creates a primary redshift (Lehner and Auby 2000). In the trail, full plasma coupling limits the spectral enlargement to the opposite side. However, self-steepening induced at increasing  $Q$  inhibits the MPI redshifting and instead further displaces the spectrum to the blue side. This creates an asymmetric spectral broadening with a prominent blueshift  $\Delta\lambda < 0$  (Berkovsky *et al* 2005, Gaeta 2000, Ward and Bergé 2003, Yang and Shen 1984).

Figure 9 shows spectral modifications around 790 nm induced by SPM affected by space-time focusing and self-steepening in the presence (or not) of ionization in fused silica. The properties stressed by equation (64) can be refound. Note the asymmetry in the SPM profile when the Fourier transform of the on-axis field intensity is expressed in wavelengths (figure 9(a)), since  $\Delta\omega = -2\pi c \Delta\lambda/\lambda^2$ . For comparison, figure 9(d) illustrates the supercontinuum reached in air with or without pulse steepening at 800 nm. In all cases, we can observe a clear amplification of the UV/blue wavelengths due to steepening terms.

### 3.6. Modulational instabilities: the route to multiple filamentation

In the context of nonlinear optics, an intense wave propagating in a focusing Kerr medium can break up into several spots from the inhomogeneities affecting its initial distribution. This phenomenon was first evidenced by self-focusing experiments in liquids (Bespalov and Talanov 1966, Campillo *et al* 1973) and the resulting small-scale structures are usually named ‘filaments’. Because this process mostly concerns spatial distortions, (2 + 1)-dimensional models freezing temporal dependences can be used to simulate the early filamentation stage of high power beams in various media (Dubietis *et al* 2004a, 2004c, Fibich *et al* 2005, 2004, Kandidov *et al* 2005, 1999, Porras *et al* 2004). In plasma regimes, 2D models can also simulate complex multifilamentation patterns created from terawatt laser pulses

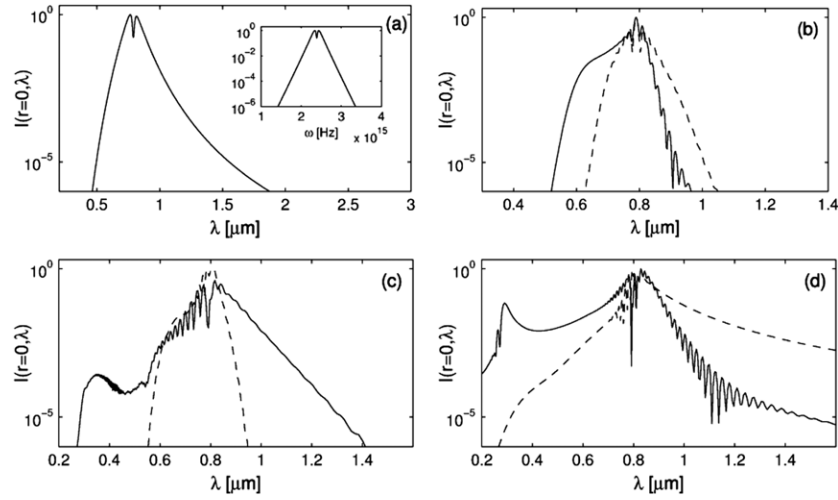


**Figure 9.** Spectral broadening induced by SPM and steepening effects in fused silica: (a) with purely cubic nonlinearity (inset shows the spectrum in frequency for comparison), (b) with Kerr + GVD only (---) and when adding space-time focusing and self-steepening (—) for  $P_{in} = 3P_{cr}$ , (c) same with plasma generation that remains inefficient at this power level (dashed curve, see figure 6), but strongly affects the spectrum when  $P_{in} = 6P_{cr}$  (—). For comparison, (d) shows supercontinuum with (—) and without (---)  $T, T^{-1}$  in air for the initial data of figure 7.

(Bergé *et al* 2004, Skupin *et al* 2004b). For instance, by assuming that MPI counterbalances Kerr focusing at a dominant time slice  $t = t_c(z)$ , the field envelope can be decomposed as  $\psi = \tilde{\psi}(x, y, z) \times e^{-[t-t_c(z)]^2/\tau^2}$  where the highest intensity peak is modeled by the temporal Gaussian with constant extent  $\tau$ . Plugging the above expression into equations (51a) and (51b) and averaging the result in time supplies the extended NLS equation for the spatial profile  $\tilde{\psi}$

$$i\partial_z \tilde{\psi} = -\nabla_{\perp}^2 \tilde{\psi} - f(|\tilde{\psi}|^2) \tilde{\psi}, \quad (65a)$$

$$f(s) = \alpha s - \frac{\epsilon s^2}{\sqrt{3}} - \sqrt{\frac{\pi}{8K}} \tau \Gamma s^K + i \frac{v s^{K-1}}{\sqrt{K}}, \quad (65b)$$

where the coefficient  $\alpha$  averages the Raman delayed response. This model does not formally depend on the longitudinal location of the time slice  $t = t_c(z)$ . The only arbitrariness is the choice of the peak duration  $\tau$ . Because pulses can be shortened to 1/10 of their initial duration, the value  $\tau = 0.1$  was found to provide the best approximations of fluence patterns.

Modeling filament formation then requires a perturbation theory involving a steady-state solution, expressed as  $\tilde{\psi}_s(\vec{r}, z) = \phi(\vec{r})e^{i\lambda z}$ . Defined in the limit of no dissipation ( $v \rightarrow 0$ ),  $\phi$  satisfies the differential equation

$$-\lambda\phi + \vec{\nabla}_{\perp}^2 \phi + f(\phi^2)\phi = 0 \quad (66)$$

and  $\lambda = \text{const}$ . Stability of  $\phi$  is investigated from perturbations  $v + iw$  with small real-valued components ( $v, w$ ). Linearizing equations (65a) and (65b) yields the eigenvalue problem (Kuznetsov *et al* 1986)

$$\partial_z v = L_0 w, \quad L_0 = \lambda - \vec{\nabla}_{\perp}^2 - f(\phi^2), \quad (67a)$$

$$-\partial_z w = L_1 v, \quad L_1 = \lambda - \vec{\nabla}_{\perp}^2 - [f(\phi^2) + 2A] \quad (67b)$$

with  $A \equiv u f'(u)|_{u=\phi^2}$ , from which different kinds of instabilities can be investigated.

*Modulational instabilities.* Originally proposed by [Bespalov and Talanov \(1966\)](#), the modulational instability (MI) theory involves oscillatory perturbations that split the beam envelope approximated by a background uniform solution. Perturbative modes are chosen as  $v, w \sim \cos(k_x x) \cos(k_y y) e^{\gamma z}$  and they apply to a plane wave  $\phi$  which satisfies  $\nabla_\perp^2 \phi = 0$  and  $\lambda = f(\phi^2)$ . The growth rate  $\gamma$  is then given by

$$\gamma^2 = k_\perp^2 (2A - k_\perp^2). \quad (68)$$

Plane waves are unstable with  $\gamma^2 > 0$  in the range  $0 < k_\perp < \sqrt{2A}$  and the maximum growth rate  $\gamma_{\max} = A$  is attained for  $k_{\max} = \sqrt{A}$ . This instability promotes the beam breakup into arrays of small-scale filaments periodically distributed in the diffraction plane with the transversal spacing  $\lambda_{\text{mod}} \simeq 2\pi/k_{\max}$  and longitudinal length  $\sim \gamma_{\max}^{-1}$ . The number of filaments is close to the ratio  $P_{\text{in}}/P_{\text{fil}}$ , where  $P_{\text{fil}}$  is the power enclosed in one filament. Considering each filament with radial symmetry, the evaluation  $P_{\text{fil}} \simeq 2\pi \int_0^{\lambda_{\text{mod}}/2} r |\phi|^2 dr \simeq 2.65 P_c$  holds for unsaturated Kerr media [ $f(s) = s$ ].

Because plane waves constitute rough representations of physical beams, they can be replaced by the soliton modes of the NLS equation (66). Perturbations are, e.g. local in  $x$  and they promote the formation of bunches periodically distributed over the  $y$  axis. Numerical computations are then required for solving the spectral problem (67a) and (67b) ([Akhmediev et al 1992](#), [Rypdal and Rasmussen 1989](#), [Zakharov and Rubenchik 1974](#)).

*Azimuthal instabilities.* For broad beams, self-focusing takes place as a regular distribution of dots located upon ring diffraction patterns ([Feit and Fleck 1988](#)). To model this instability, the Laplacian in equation (65a) must be rewritten as  $\nabla_\perp^2 = r^{-1} \partial_r r \partial_r + r^{-2} \partial_\theta^2$ , where  $\theta$  denotes the azimuthal angle. Within a first approximation, unstable modes  $v, w \sim \cos(M\theta) e^{\gamma_M z}$  with azimuthal index number  $M$  break up a uniform spatial ring lying on a circular path with length  $s = \bar{r}\theta$ , and mean radius  $\bar{r}$ . Equations (67a) and (67b) then yield ([Atai et al 1994](#), [Soto-Crespo et al 1992](#))

$$\gamma_M^2 = \left(\frac{M}{\bar{r}}\right)^2 \left(2A - \frac{M^2}{\bar{r}^2}\right), \quad (69)$$

and the maximum number of modulations on the ring is provided by the integer part of  $M_{\max} = \bar{r}\sqrt{A}$ .

Ring-shaped waveforms can also exhibit a phase singularity with an integer number of windings,  $m$  (topological charge). Such structures are termed ‘optical vortices’. They convey a constant orbital angular momentum ([Firth and Skryabin 1997](#), [Kruglov et al 1992](#), [Kruglov and Vlasov 1985](#), [Michinel et al 2001](#), [Quigora-Teixeiro and Michinel 1997](#)) and are experimentally designed by means of phase masks and holographic techniques ([Desyatnikov et al 2005](#), [Tikhonenko et al 1996](#)). For cubic media, they undergo azimuthal MI, which make vortex solitons decay into  $M_{\max} \sim 2|m| + 1$  filaments ([Vinçotte and Bergé 2005](#), [Vuong et al 2006](#)). The orbital motion confers robustness to vortex solitons, which can propagate beyond several tens of Rayleigh distances, before they break up into filaments.

Figure 10 shows the multifilamentation of (a) a Gaussian beam, (b) a flat-phase, ring-shaped waveform and (c) an  $m = 2$  vortex breaking up into  $2|m| + 1$  filaments in a cubic medium. MI is triggered either from an initial defect or from random noise ([Bergé et al 2003](#)). Note the robustness of the Gaussian profile, whose shape definitively differs from that of a plane wave.

Modulational instabilities rather affect the early Kerr stage in the beam propagation. At later stages, the resulting filaments become fully nonlinear and they may interact mutually. From the interplay between diffraction and nonlinearity, two filaments can fuse, whenever their

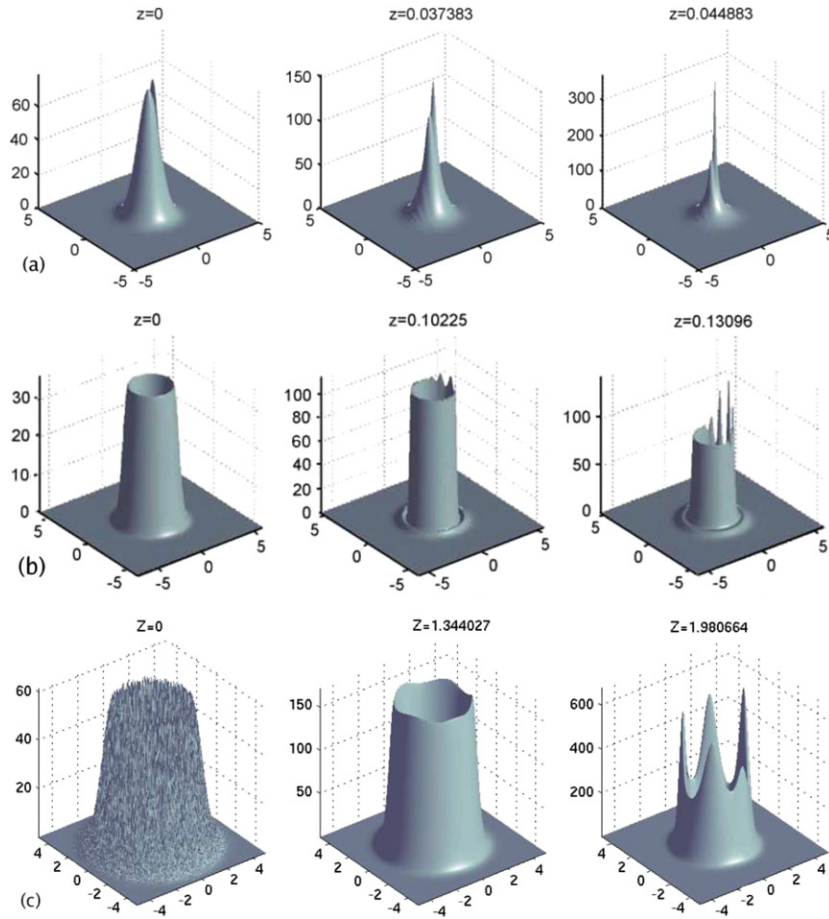


**Figure 10.** Multifilamentation patterns in Kerr focusing regime at powers above critical ( $P_{in} \leq 30P_{cr}$ ) for (a) a Gaussian beam ( $x_0 = 0.35$ ,  $y_0 = 0$ ,  $\epsilon = 0.1$ ) and (b) an annular ring with flat phase ( $x_0 = 1.7$ ,  $y_0 = 0$ ,  $\epsilon = 0.01$ ). These two beams feature initially a local defect with relative amplitude  $\epsilon$  located at the coordinates  $(x_0, y_0)$ . (c) Vortex-shaped beams with charge  $|m| = 2$  initially perturbed by a 10% random noise.

separation distance is below a critical value, a function of their individual powers (Bergé *et al* 1997, McKinstrie and Russell 1988). With no saturation, each filament whose power is above critical creates its own attractor, at which it freely collapses. By including saturation, filaments with powers above critical are able to coalesce into an intense central lobe and develop various patterns (Konno and Suzuki 1979). Without any control, multifilamentation happens as a harmful instability destroying the homogeneity of the energy distribution. It has detrimental consequences on the quality of the beam shape.

#### 4. Universal features of femtosecond filamentation

For an efficient propagation, the beam intensity and electron density must both remain below their so-called ‘laser-induced breakdown’ (LIB) limits. LIB means the breakdown of the

beam that results in damage or tremendous energy absorption in dielectrics as well as in liquids (Kennedy 1995). It involves three major processes, namely, (i) ionization, (ii) heating of the ‘free’ electrons by the radiation and (iii) transfer of plasma energy to the medium. Once generated, the electron plasma absorbs and scatters the remaining pulse energy. Assuming free electrons seeded by avalanche ionization,  $\partial_t \rho \simeq (\sigma/U_i)\rho I$ , an incident pulse launched in tightly focused geometry will be significantly attenuated by energy absorption at density levels above a critical value,  $\rho_{\text{cr}}$ . An estimate of the LIB intensity then follows as  $I_{\text{LIB}} \sim (U_i/\sigma t_p) \ln(\rho_{\text{cr}})$  (Feng *et al* 1995). For subpicosecond pulses, multiphoton processes mostly provide the dominant breakdown mechanism, such that the estimate  $I_{\text{LIB}} \sim (\rho_{\text{cr}}/\rho_{\text{nt}}\sigma_K t_p)^{1/K}$  applies (Feng *et al* 1997). Ranges of values for  $\rho_{\text{cr}}$  are often close to 10% of  $\rho_{\text{nt}}$  (e.g.  $\rho_{\text{cr}} = 10^{21} \text{ cm}^{-3}$  in silica or water) when using femtosecond pulses (Lenzner *et al* 1998, Noack and Vogel 1999).

In what follows, characteristics of ultrashort pulse propagation are mostly depicted for peak electron densities less than the LIB threshold. Density levels maintain the pulse in the self-channeled state without significant conversion of beam energy into the plasma.

#### 4.1. Radial self-focusing and temporal splittings

The self-channeling mechanism relies on the balance between Kerr focusing and plasma generation. The most illuminating example is given by ‘femtosecond filaments’ in air, as presented in figure 1. Atmospheric filaments form microstructures exhibiting  $\sim 100\text{--}150 \mu\text{m}$  in FWHM diameter and  $\sim 1 \text{ mJ}$  in energy at infrared wavelengths (800 nm). They are accompanied by a strong SPM-induced spectral broadening and cover several tens of metres, whenever the input pulse power exceeds  $\sim 10 \text{ GW}$  (Braun *et al* 1995, Brodeur *et al* 1997, Nibbering *et al* 1996). Propagation distances in excess of 200 m were even reported for 60 fs, 795 nm pulses with 4 mm diameter, traveling thus upon a few Rayleigh distances  $z_0$ . These experiments revealed, after a possible short stage of multiple filamentation, the emergence of one robust filament coupled to electron densities of a few times  $10^{16} \text{ cm}^{-3}$  (LaFontaine *et al* 1999b). Further measurements of infrared filaments specified a peak intensity of about  $5 \times 10^{13} \text{ W cm}^{-2}$  (Kasparian *et al* 2000a). Similar behaviors involving slightly higher peak intensities were also reported in  $\text{N}_2$  molecular gases at different pressures (Becker *et al* 2001).

The ‘moving-focus’ model was first revisited to yield qualitative explanations of this phenomenon (Brodeur *et al* 1997, Chin *et al* 1999a). Though pleasant and rather intuitive, this model, however, failed in describing the self-guiding of light that persists beyond the linear focus of convergent beams (Lange *et al* 1998b). The appropriate scenario for long-distance propagation, called ‘dynamical spatial replenishment’, was specified by numerical simulations. During the focusing stage, the beam generates a narrow plasma that strongly defocuses the trailing part of the pulse and creates one leading peak. Once the intensity decreases enough (via, e.g. MPA), plasma generation turns off. The back pulse can then refocus, which produces a two-spiked temporal profile (Mlejnek *et al* 1998a, 1998b). In space, plasma defocuses only the inner part of the beam intensity, so that the trailing edge decays into spatial rings (Kandidov *et al* 1994). With increasing propagation distances and as the front pulse intensity decreases, the spatial rings coalesce under Kerr compression and allow refocusing of the trail. Although the beam radius may look ‘quasi-static’, the temporal and spatial distributions of the pulse strongly fluctuate (see, e.g. figure 7). At high enough powers, self-channeling is supported by several focusing/defocusing cycles triggered from a dynamical interplay between multiple, stringent peaks alternating in the temporal pulse profile. ‘Pushed’ by steepening effects, these peaks are responsible for the formation of optical shocks

**Table 1.** Parameter values for dioxygen molecules (air) at 800 nm ( $U_i = 12.1$  eV,  $\rho_{nt} = 5.4 \times 10^{18}$  cm $^{-3}$ ), fused silica at  $\lambda_0 = 790$  nm and 1550 nm ( $U_i = 7.8$  eV,  $\rho_{nt} = 2.1 \times 10^{22}$  cm $^{-3}$ ), and water at 527 nm ( $U_i = 7$  eV,  $\rho_{nt} = 3.32 \times 10^{22}$  cm $^{-3}$ ).

$\lambda_0$ (nm)	$n_2$ (cm $^2$ W $^{-1}$ )	$k''$ (fs $^2$ cm $^{-1}$ )	$\sigma_K$ (s $^{-1}$ cm $^{2K}$ W $^{-K}$ )	$K$
800/O $_2$	$4 \times 10^{-19}$	0.2	$2.9 \times 10^{-99}$	8
248/O $_2$	$8 \times 10^{-19}$	1.21	$2 \times 10^{-28}$	3
790/SiO $_2$	$3.2 \times 10^{-16}$	370	$6.8 \times 10^{-56}$	5
1550/SiO $_2$	$2.2 \times 10^{-16}$	−280	$1.5 \times 10^{-119}$	10
527/H $_2$ O	$2.7 \times 10^{-16}$	560	$1.07 \times 10^{-28}$	3

in the medium. This complex dynamics was reported by several authors, dealing with pulse propagation either in air (Aközbek *et al* 2001, Bergé and Couairon 2000, Chiron *et al* 1999, Couairon *et al* 2002), in argon cells (Champeaux and Bergé 2003, Nurhuda *et al* 2002a), or even in fused silica (Tzortzakis *et al* 2001d).

Because the fundamental scenario for self-channeling is that aforementioned, estimates for peak intensities ( $I_{\max}$ ), electron densities ( $\rho_{\max}$ ) and filament radius ( $L_{\min}$ ) can be deduced from equating diffraction, Kerr and ionization responses. This yields the simple relations

$$I_{\max} \simeq \frac{\rho_{\max}}{2\rho_c n_0 \bar{n}_2}, \quad \rho_{\max} \simeq t_p \rho_{nt} W(I_{\max}), \quad (70a)$$

$$L_{\min} \sim \pi (2k_0^2 \bar{n}_2 I_{\max} / n_0)^{-1/2}, \quad (70b)$$

where

$$\bar{n}_2 = n_2(1 - x_K) + n_2 x_K \max_t G(t) \quad (71)$$

represents the effective Kerr index when the Raman-delayed response is maximum over the initial pulse profile and  $W(I_{\max})$  reduces to  $W(I_{\max}) = \sigma_K I_{\max}^K$  in MPI regime. Some parameter values for different materials used throughout this review have been indicated in table 1. From these values the above relations supply filament diameters of the order of 150  $\mu$ m in air at 800 nm and 10–20  $\mu$ m in dense transparent media (dielectrics, water), which agrees with current numerical data. Note that for laser wavelengths of about 1  $\mu$ m, the requirement (9) is always fulfilled. As inferred from table 1, the critical power for self-focusing exceeds the GW level in gases, but remains limited to a few MW in dense materials.

Plasma generation is mostly expected to stop the divergence of the beam caused by self-focusing, except for specific values of the parameters  $P_{in}/P_{cr}$  and  $\delta \sim k''$  that privilege collapse arrest by dispersion (see figure 6). For  $\lambda_0 = 800$  nm, nonlinear fluorescence techniques (Liu *et al* 2005b) recently revealed that small-scale filaments created in water at powers lower than  $8P_{cr}$  did not need plasma saturation. With 38 fs (FWHM), 110  $\mu$ m pulses and  $k'' \sim 300$  fs $^2$  cm $^{-1}$ , the plasma response may indeed be inhibited, following figure 6. Pulses are then subject to space-frequency coupling from the interplay among SPM, dispersion and phase mismatching, that produces conical emission (see below). The energy loss caused by the conical wave depends on the energy contained in the colored part of the spectrum. Liu *et al* (2005b) suggests that if the phase-matching width of light waves whose frequencies experience self-focusing is small enough compared with the spectral width of the on-axis laser pulse, the spectral energy going into the self-focusing components is small and the energy loss caused by conical emission becomes large. This phase-matching width is all the smaller as GVD is large and the spread of energy can stop the Kerr focusing without the help of plasma at powers moderately above critical.

Nonetheless, different scenarios have attracted attention in the past few years. For instance, research groups led by Di Trapani and Dubietis (Dubietis *et al* 2004a, 2003, Porras *et al* 2004)



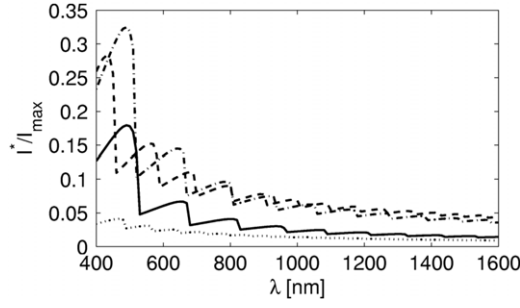


**Figure 11.**  $I^*/I_{\max}$  versus  $\lambda_0$  for different pulse durations  $t_p$  in air (70 fs, dotted curve), in fused silica (20 fs, dashed curve), and in water (170 fs, solid curve; 50 fs, dash-dotted curve).

emphasized the apparent absence of free electron emission in the self-guiding of 527 nm, 200 fs pulses with  $\sim 100 \mu\text{m}$  waist and powers up to  $10 P_{\text{cr}}$ , propagating in water in loosely focused geometry. Numerical simulations outlined the filament reshaping into a nonlinear  $X$  (biconical) wave, driven by the combination between linear diffraction, normal GVD, self-focusing and nonlinear losses (Kolesik *et al* 2004). Whereas GVD cannot halt the beam collapse in these configurations ( $\delta$  is too small), normal dispersion plays an important role by spreading the most intense time slices of the pulse. Instead of an extensive production of free electrons, the nonlinear losses (MPA) moreover dominate at laser wavelengths as low as 527 nm. From equations (70a), it is always possible to compute numerically the ratio  $I^*/I_{\max}$  that dictates the MPA efficiency [ $\sim U_i \rho_{\text{nt}} W(I)/I$ ] compared with plasma defocusing [ $\sim ik_0 \rho / \rho_c$ ] in equation (23). This ratio involves the quantity

$$I^* = n_0^2 \rho_c U_i / (k_0 t_p), \quad (72)$$

that scales like  $n_0 / (\lambda_0 t_p)$ . The resulting curve is displayed in figure 11 for fused silica, water and air at different pulse durations. The Keldysh ionization rate for crystals is used for dense media, while the PPT rate is employed for air ( $\text{O}_2$  molecules). This figure shows that the percentage of MPA over the emission of free electrons augments all the more as the laser wavelength is low and the pulse duration is short. In air, MPA becomes negligible compared with MPI. For dense materials, figure 11 points to a sudden change in the influence of MPA whenever  $\lambda_0 < 600 \text{ nm}$ . This mainly follows from the dependences over  $\lambda_0$  of both the critical plasma density (37) and the photo-ionization rate  $W(I)$ . As a result, self-focusing is stopped at lower intensities and the free electron density is maintained at weaker levels (Skupin *et al* 2006a).

#### 4.2. Robustness and multifilamentation

Femtosecond filaments are remarkably robust, in the sense that they can propagate over several metres and even reform after hitting an obstacle. In the atmosphere, aerosol particles, like water droplets or dust, may have dimensions comparable with the filament diameter, which could seriously harm the dynamical balance required to propagate filaments. However, even opaque droplets as large as  $100 \mu\text{m}$  in diameter do not block filamentation. More intriguingly, energy losses are limited to 15% of the filament energy (Courvoisier *et al* 2003). The filament rapidly self-heals and seems unaffected by the droplet, so that an energy balance between the filament core and the unfocused part of the beam was conjectured to explain the rebuilding of the pulse. Unfocused parts of the beam refer to the ‘photon bath’, i.e. the low amplitude background surrounding the filament core.

Numerical simulations constrained to the radial symmetry reproduced the smallness of the immediate energy losses in air and the interaction dynamics was similar whatever the pulse self-channels in the first (leading edge) or in the second (trailing edge) focusing stage (Kolesik and Moloney 2004b). From water experiments (Dubietis *et al* 2004a, 2004b), analogous conclusions were drawn, which insisted more on the linear contribution from the outer conical waves to the filament reconstruction. The ‘active zone’ of the photon bath must, however, keep time slices with power above critical to re-localize the beam at the center. The filament must also be somehow delocalized in space, in order to justify the smallness of energy losses during the collision. Answering this point, simulations revealed that the breakup of rotational symmetry of pulsed beams can push the focusing components, still untouched by the plasma, out of axis. The defocused time slices diffract to the low intensity background, but the focusing ones exit out of the center (Skupin *et al* 2003, 2002). A femtosecond filament thus consists of a ‘spatially-extended’ structure, whose most intense components can move within a zone of several hundreds of  $\mu\text{m}$  around the origin. Through a collision, just a few components are involved, which explains the smallness of the losses. Three-dimensional simulations enclosing the filament inside a circular disc of  $300\ \mu\text{m}$  in diameter clearly showed that over the 2 cm of self-healing the beam components outside this zone play no significant role in the filament reconstruction (Skupin *et al* 2004a). Some of these results are summarized in figure 12. Recent experiments using pinholes to block the photon bath confirmed these theoretical predictions. The energy reservoir actively feeding the filament core was measured within a diameter of  $220\text{--}440\ \mu\text{m}$  and was found to contain up to 50% of the pulse energy (Liu *et al* 2005c).

Whereas a single filament appears as a robust object, broad pulses having many critical powers become subject to modulational instability. The background energy reservoir favors energy exchanges between the different optical cells, that focus under Kerr compression and defocus by plasma generation. A sea of collapsing spots is thus nucleated, forming an ‘optically turbulent femtosecond light guide’ along which nonlinear dissipation consumes small energy per filament (Mlejnek *et al* 1999). Inside the bundle, the filaments are able to merge and relaunch recurrent collapse events at further distances. They gather into long-range clusters composed of secondary cells that occur around the primary filaments created from the initial beam defects (Bergé *et al* 2004, Skupin *et al* 2004b). For broad pulses ( $w_0 > 1\ \text{cm}$ ) enclosing more than  $100 P_{\text{cr}}$ , the self-focusing distance is close to the MI filamentation length  $z_{\text{fil}} \sim 1/n_2 I_0$ , which varies like  $1/P_{\text{in}}$  (Campillo *et al* 1974, Fibich *et al* 2005).

For narrower beams, experiments exploring mJ, mm-waisted pulses (Hosseini *et al* 2004a, Liu *et al* 2004, Tzortzakis *et al* 2001a) reported the beam breakup into two filaments that continue to increase in intensity by Kerr focusing. Depending on their separation distance and individual powers, these filaments can merge. An example of this fusion mechanism is shown in figure 13 for two (plasma-free) optical spots, resulting from the modulational instability of a 42 fs, 3 mm-waisted collimated pulse in air (Tzortzakis *et al* 2001a). In the presence of plasma defocusing, ‘parent’ filaments develop spatial rings whose radius increases with  $z$ . Two systems of rings can thus interfere to yield ‘child’ filaments. Each focusing spot triggers a plasma sequence that defocuses the trail pulse and locates the cells at specific negative instants. The number of ‘filaments’ is therefore higher in intensity than in the beam fluence, which sums up all the time slices (Champeaux and Bergé 2005).

Since multifilamentation emerges from the initial beam defects, several techniques to control this process in shot-to-shot, metre-range experiments have been proposed. Among these, we can mention the introduction of beam ellipticity (Dubietis *et al* 2004c, Grow and Gaeta 2005) or of a tilted lens (Fibich *et al* 2004) along the optical path. Strong field gradients or forcing aberrations through phase masks can also be used to control high intensities over long scales (Méchain *et al* 2004). Other techniques consist of monitoring



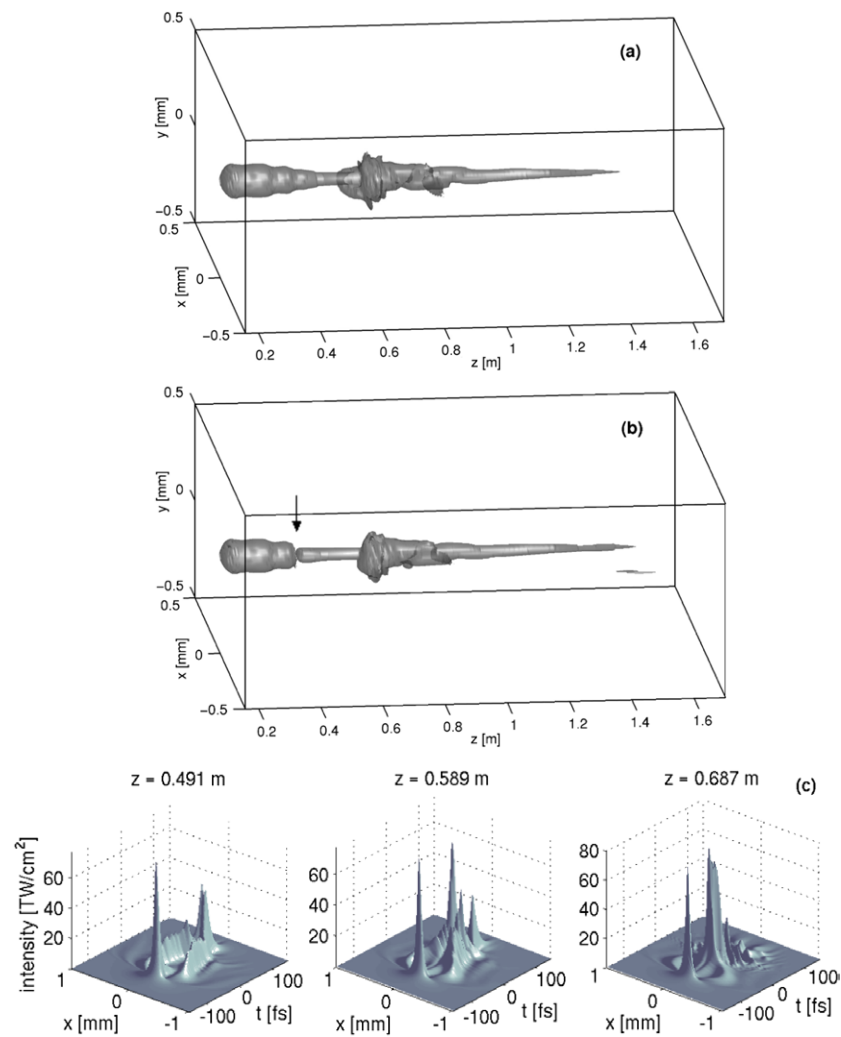


**Figure 12.** 3D surface plots of plasma strings in cases of (a) free propagation or (b) an impact with a 95 μm large droplet located at  $z = 0.4$  m (see arrow), computed from (3 + 1)-dimensional numerical simulations. Note the convected components at  $z \sim 0.65$  m, corresponding to the second focusing sequence when the trail peak takes over the front pulse and develops azimuthal instabilities in space. (c) Temporal profiles occupying an active zone of  $\sim 300$  μm in diameter.

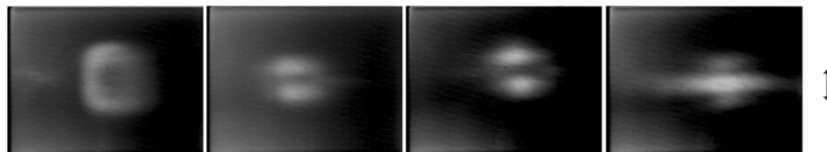


**Figure 13.** Merging of two filaments created from mm-waisted, fs pulses with 5 mJ energy. Arrow indicates a scale length of 2 mm.

the filamentation distance by changing the beam divergence angle with a deformable mirror (Jin *et al* 2005). By this method, a single filament has been produced with powers as high as 420 GW, usually yielding multiple filaments in collimated geometry. Alternative methods consist of tuning the focal distance of a telescope setup composed of divergent and convergent lenses (Fibich *et al* 2006, Liu *et al* 2006b). Interesting features have recently been published concerning the fusion, repulsion and spiral co-propagation of two filaments, depending on their relative phase shift and crossing angle, which may further be used to optimize the propagation range (Xi *et al* 2006). In the same spirit, arrays of diffractive microlenses (Cook *et al* 2005) or periodic meshes (Kandidov *et al* 2005) into the propagation path help in making the multifilamentation ‘more deterministic’. As a matter of fact, these methods amount to altering the background surface of the beam from which small-scale filaments can randomly emerge from modulational instability. Alternative ways may be provided by femtosecond optical vortices (Vinçotte and Bergé 2005) that keep the filaments rotating along a ring and are nowadays designed experimentally on fs time scales (Mariyenko *et al* 2005, Vuong *et al* 2006). Further explorations should concern optical smoothing techniques breaking the laser spatial or temporal coherence (Marklund and Shukla 2006).

#### 4.3. White-light generation and conical emission

Spectral broadening has been the topic of intense investigations for several decades (Alfano and Shapiro 1970). In 1995, Gil'denburg *et al* (1995) performed 2D numerical simulations of ultrashort focused electromagnetic waves creating breakdown plasma due to tunnel gas ionization. High blueshifts of the pulse spectrum up to  $\Delta\omega/\omega_0 \equiv \omega/\omega_0 - 1 > 40\%$  were reported. At that time, blueshift was attributed to plasma generation, as the growth of free electrons increases the plasma frequency by  $\omega_{pe}^2 = q_e^2 \rho(I)/m_e \epsilon_0$  and implies a positive frequency shift  $\Delta\omega_+ \sim \int_0^z \partial_t \rho \, dl$  (Penetrante *et al* 1992, Rae and Burnett 1992, Yablonovitch 1974). Later, experimental spectra revealed an ‘ultrafast white-light continuum’. This occurs in a wide variety of condensed and gaseous media, whenever the input beam power exceeds the self-focusing threshold (Brodeur and Chin 1998, 1999). Around the central wavelength of 800 nm, blueshifts ( $\Delta\omega_+$ ) down to 0.5  $\mu\text{m}$  in wavelength enlarged the spectra at intensities lower than  $10^{-2}$  times the central one. Spectral enlargements appeared asymmetric, with a limited redshift, which could not be explained by SPM theory alone. Continua emitted from gases were found narrower ( $\Delta\omega_+ \simeq 0.5 \omega_0$ ) than those for dense media ( $\Delta\omega_+ \simeq 0.8\text{--}1.6 \omega_0$ ).

Because this process mixes all spectral components in the visible range, the core of the filament evolves like a white spot, which gives rise to a ‘white-light laser’ (Chin *et al* 1999b). Noting by  $\varphi(\vec{r}, t)$  the phase of the field envelope, frequency variations with no steepening term are dictated by

$$\Delta\omega = -\partial_t \varphi \sim -k_0 \Delta z \partial_t (\bar{n}_2 I - \rho/2n_0 \rho_c), \quad (73)$$

which varies with the superimposed actions of the Kerr and plasma responses. Near the focus point, only the front leading edge survives from this interplay and a redshift is enhanced by plasma generation. At later distances, second focusing/defocusing sequences relax the spectra to the blue side while the redshifted components decrease in intensity. A salient blueshift around the central frequency follows from self-steepening that creates a shock edge at the back of the pulse and amplifies a ‘blue shoulder’ in the spectrum (Aközbek *et al* 2001). This spectral dynamics readily follows from equation (64). Asymmetries caused by the focusing events are important: they design the pulse spectrum which will be preserved after the nonlinear stage of the beam.

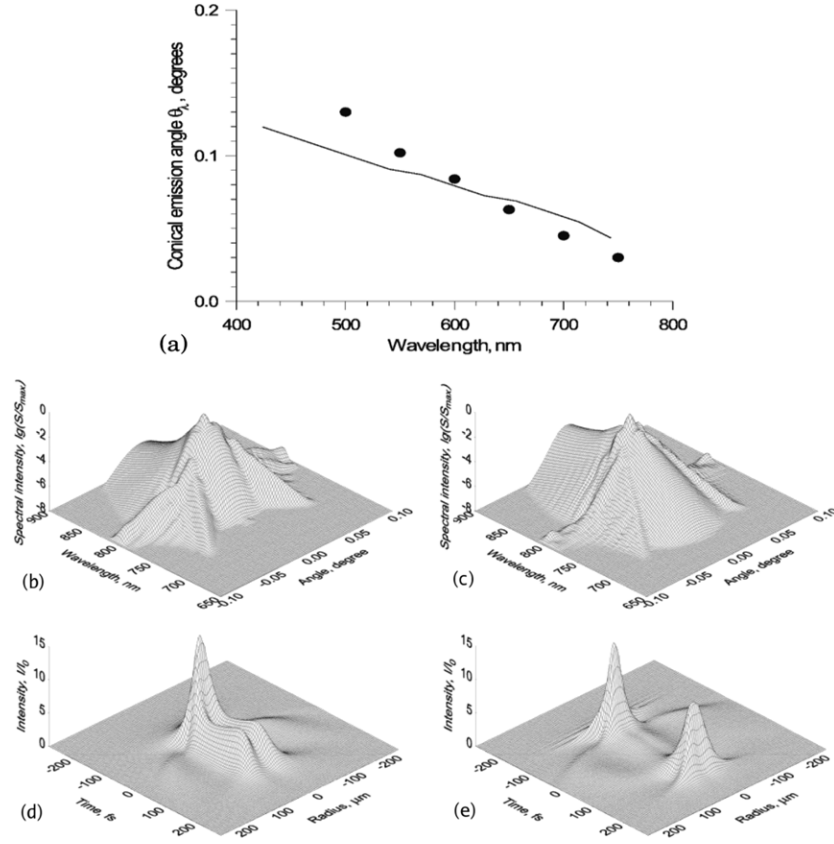


**Figure 14.** (a) Measured (symbols) and calculated (curve) CE angles in air. (b) and (c) Frequency angular spectra. (d) and (e) Spatio-temporal distributions of an atmospheric, fs filament starting from infrared pulses with 6.3 critical powers, 250 fs FWHM duration and 0.18 mm radius at two different propagation distances (b) and (d)  $z = 0.43z_0$ ; (c) and (e)  $z = 0.6z_0$  (Kandidov *et al* 2003). Courtesy of Kosareva.

The pulse spectrum is usually computed from the Fourier transform of the field intensity, either at  $r = 0$ , or being averaged over the filament radius,  $S_{\text{fil}}(\omega) = 2\pi \int_0^{r_{\text{fil}}} |\hat{\mathcal{E}}(r, \omega)|^2 r dr$ . More insights can be obtained by looking at the frequency–angular spectral function  $S(\theta_x, \theta_y, \omega, z) = |Q(\theta_x, \theta_y, \omega, z)|^2$ , defining

$$Q(\theta_x, \theta_y, \omega, z) = \int dx dy dt U(x, y, z, t) e^{i\omega t - i\theta_x kx - i\theta_y ky}, \quad (74)$$

where  $\theta_x = k_x/k$ ,  $\theta_y = k_y/k$  are the angles at which different frequency components  $\omega$  propagate in the medium. The dependence of the angle  $\theta = \theta_x = \theta_y$  on wavelength defines the supercontinuum cone emission and is obtained by means of the expression  $\lambda = 2\pi c/\omega$ . Surface plots of  $\ln S(\lambda, \theta)$  compared with the spatio-temporal intensity distributions reveal a conical emission (CE) driven by ‘wings’ directed to nonzero angles and connected with the plasma-induced spatial rings (Kandidov *et al* 2003, 2004). Nibbering *et al* (1996) and Kosareva *et al* (1997) first revealed the existence of this conical emission accompanying femtosecond filamentation in air at 800 nm. Recalled in figure 14(a), CE increases in the interval  $0 \leq \theta \leq 0.12^\circ$  with decreasing wavelengths  $800 \geq \lambda \geq 500$  nm and is independent of the position along the filament. This ‘conical emission’ corresponds to the angular divergence

of spectral components. The (half-) angle  $\theta$  at which the radiation propagates is determined by the spatial gradient

$$\theta(\vec{r}, t) = \arctan \left| k_0^{-1} \frac{\partial}{\partial r} \varphi(\vec{r}, t) \right|. \quad (75)$$

This angle depends on the spatial intensity distribution of the pulse, which strongly evolves in the self-channeling regime, as illustrated in figures 14(b)–(e). By comparing the radial dependences of the divergence angle  $\theta(r)$ , low-frequency components are located nearest the optical axis. High frequency components lie near the periphery rings and their radiation is directed out of the axis.

Besides Kerr and plasma effects, the material dispersion can play a relevant role in condensed media, for which the GVD coefficient is usually high. Kolesik *et al* (2003a, 2003b) compared the extension of supercontinuum wings generated in air ( $k'' = 0.2 \text{ fs}^2 \text{ cm}^{-1}$  at 800 nm) and in water ( $k'' = 500 \text{ fs}^2 \text{ cm}^{-1}$  at 400 nm). Numerical simulations accounting for the complete linear dispersion relation displayed evidence of chromatic dispersion becoming a key player (for dense materials above all) in determining the spectral extent of supercontinuum generation. Full chromatic dispersion included in  $k(\omega)$  encompasses the  $T, T^{-1}$  operators when passing to an envelope description (see section 2). These operators induce steepening of the pulse profile and strongly ‘blueshift’ the spectra.

On the other hand, spectral broadening becomes enhanced by harmonic generation. The question of coupling ultrafast infrared (IR) components with a self-induced third harmonic was raised ten years ago (Backus *et al* 1996). While conversion efficiency as high as 0.1% was first reported for third-harmonic (TH) generation in air, higher efficiencies up to 0.2% were next achieved by using focused pulses filamenting over only  $\sim 10$  cm. At 800 nm, the coupling of TH with the IR pump produces a ‘two-colored’ femtosecond filament from the threshold intensity  $I(\omega) \geq 2 \times 10^{13} \text{ W cm}^{-2}$  (Aközbek *et al* 2002, Alexeev *et al* 2005, Yang *et al* 2003). Along this process, the pump wave injects part of its energy into the third harmonic. The amount of pump energy depends on the linear wavevector mismatch parameter  $\Delta k = [3k(\omega) - k(3\omega)]^{-1}$  fixing the coherence length  $L_c = \pi/|\Delta k|$ . The smaller the coherence length, the weaker the TH fields, since most of the pump energy is periodically injected and depleted by the pump. In the self-channeling regime, the balance between TH, pump wave nonlinearities and the linear mismatch parameter makes the phase difference  $\Delta\varphi = 3\varphi(\omega) - \varphi(3\omega)$  be clamped at a constant value equal to  $\pi$  (Aközbek *et al* 2002). Along metre-range distances, the two-colored filament propagates over longer scales than an IR pulse alone, as the TH component stabilizes the pump wave and achieves 0.5% conversion efficiency (Bergé *et al* 2005). Experimental identification of the TH component reveals some central spot surrounded by ring structures absorbing most of the TH energy and having a half-divergence angle of 0.5 mrad (Théberge *et al* 2005a). This contributes to an enhancement of the total conical emission of the beam.

Manipulating intense filaments centered at 800 nm results in supercontinuum generation extending down to 230 nm in air and yielding a continuous spectral band of ultraviolet (UV) and visible wavelengths (Théberge *et al* 2005b). This phenomenon was observed over laboratory scales as well as over LIDAR propagation distances  $> 200$  m (Bergé *et al* 2005, Méjean *et al* 2006b). Resembling spectral dynamics have also been reported from 45 fs, 1 mJ infrared pulses propagating in argon at atmospheric pressure, after subsequent compression by chirped mirrors (Trushin *et al* 2005). Simulations of these experiments (Aközbek *et al* 2006) were performed from the one-component NEE model (45a) in the limit of negligible TH generation. It was found that temporal gradients inherent to the  $T, T^{-1}$  operators are sufficient to amplify

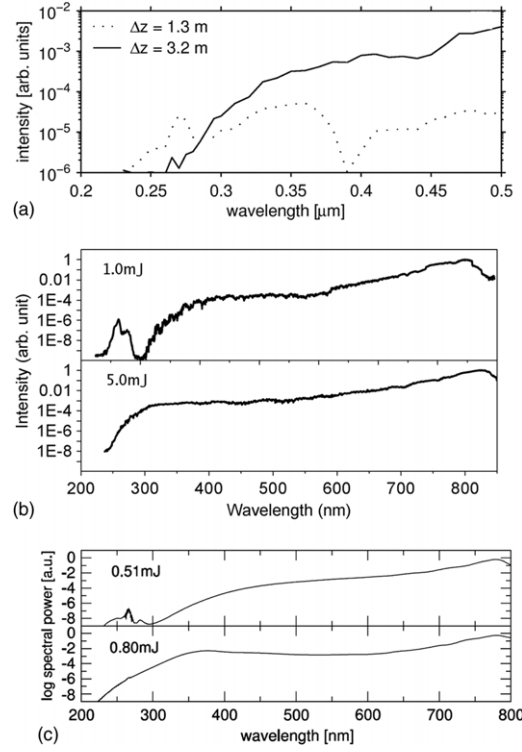


**Figure 15.** (a) UV-visible supercontinua measured in the laboratory over several metres in air. (b) Experimental spectra of the TH and fundamental fields at different pulse energies (Th  berge *et al* 2005b). Courtesy of Th  berge. (c) Angle-integrated spectra computed from the UPPE model equation (18) (Kolesik *et al* 2006). Courtesy of Kolesik.

UV shifts and cover the TH bandwidth for very short pulses ( $\leq 10 \text{ fs}$ ) over small propagation lengths.

Recently, numerical simulations (Kolesik *et al* 2006) confirmed this tendency that atmospheric propagation, i.e. TH generation, while it influences the pump dynamics to some extent, does not significantly change the spectra whose variations are mostly induced by the fundamental field. Whereas coupled equations derived for spectrally narrow envelopes ( $\Delta\omega_j/\omega_j \ll 1$ ) cannot correctly describe the spectral region where the two components overlap, more elaborate models including pulse steepening and/or chromatic dispersion emphasize the broad UV shift developed by the pump and assuring the junction with the TH bandwidth. Huge UV shifts developing from the fundamental have already been displayed for air propagation in figure 9(d). Experimental as well as numerical spectra details of the interaction between the TH and pump pulses are shown in figure 15. Figure 15(a) illustrates UV-visible spectral broadening in the wavelength domain  $200 \leq \lambda \leq 500 \text{ nm}$  for a metre-range propagation of one filament created in air from 9 mJ, 150 fs pulses at 800 nm, focused with a  $f = 5 \text{ m}$  convergent mirror (M  jean *et al* 2006b). Figure 15(b) shows a similar build-up of wavelengths for filaments created from 40 fs, 800 nm pulses in loose focusing geometry at the input energies of 1 mJ and 5 mJ. For comparison, figure 15(c) displays logarithms of the angle-integrated spectrum computed from equation (18). The numerical spectra reproduce well the previous behaviors at close, although lower energies, from input beam conditions similar to those used in the second experimental setup.

#### 4.4. Role of the laser wavelength

Whereas emphasis has been laid so far on optical pulses operating around 800 nm, one could wonder whether the propagation dynamics changes at different laser wavelengths. Besides the Rayleigh length  $z_0$ , several physical parameters become modified when varying  $\lambda_0$ .

- The Kerr index  $n_2$ , function of the cubic susceptibility  $\chi_{\omega_0}^{(3)}$ , decreases inversely proportional to  $\lambda_0$  (Agrawal 2001, Nibbering *et al* 1997).
- The photo-ionization rate and the number of photons consumed by MPI transitions  $\sim U_i/\hbar\omega_0$  vary with  $\lambda_0$ . Even though MPI gain and MPA losses cannot be separated from each other, their respective influence changes with  $\lambda_0$  and stresses more losses at low wavelengths (see figure 11).
- The value and sign of the GVD parameter,  $k'' = \partial^2 k / \partial \omega^2|_{\omega=\omega_0}$ , are modified at different laser wavelengths. Depending on the material considered,  $k''$  can turn from positive (normal GVD) to negative (anomalous GVD), which deeply modifies the spatio-temporal structure of the beam.

On this topic, propagation studies mostly concerned the differences between infrared pulses at 800 nm in the atmosphere and ultraviolet ones at, e.g. 248 nm, created by a hybrid, frequency-tripled Ti : Sa/KrF excimer chain. Long-distance propagation experiments employing ps, 248 nm pulses (Schwarz *et al* 2001, 2000) reported that after a transient stage of multiple filamentation, the beam relaxed to a single filament upon propagation ranges of more than 10 m. The filament length, defined as the spatial region where the plasma couples with the light channel, only covered  $\sim 1$  m, where the electron density, evaluated from the energy consumption per filament, attained  $3 \times 10^{15} \text{ cm}^{-3}$ . Computed from the MPI rate, the peak intensity was deduced to be about  $10^{12} \text{ W cm}^{-2}$ . Also associated with this filament, a narrow spectral bandwidth of  $\Delta\lambda \sim 10 \text{ nm}$  was measured around 248 nm. Later, Mysyrowicz's group (Tzortzakis *et al* 2000a, 2001b) observed the filamentation of UV pulses with durations from 5 ps down to 450 fs. Long, metre-range ( $\sim 2\text{--}4$  m) filaments coupled with  $10^{15}\text{--}10^{16} \text{ cm}^{-3}$  peak electron densities at intensities of  $\sim 10^{11} \text{ W cm}^{-2}$  were identified. The 'apparent' differences between UV and IR peak values follow from the pulse duration between UV and IR experiments, the plasma critical density  $\rho_c \sim 1/\lambda_0^2$  together with the number of photons involved in multiphoton transitions. This varies from  $K = 8$  at 800 nm to  $K = 3$  at 248 nm for  $\text{O}_2$  molecules. Numerical simulations, however, showed that, for 50 fs FWHM input pulses, the filament dynamics and length ( $< 5$  m), starting from the same nonlinear focus, were identical in both cases with peak intensities and electron densities attaining  $4\text{--}8 \times 10^{13} \text{ W cm}^{-2}$  and  $10^{17} \text{ cm}^{-3}$ , respectively. Even though the ionization parameters vary with  $\lambda_0$ , the peak values are fixed by the balance  $\rho_{\text{max}}/2\rho_c \sim n_2 I_{\text{max}}$ , which remains similar at the two wavelengths. Averaging the peak quantities over a given filament width can justify the different measurements made in this field (Couaeron and Bergé 2002).

Besides, changes in supercontinuum were numerically addressed by Aközbek *et al* (2003), who accounted for TH generation at other laser wavelengths such as 1064 nm and 1550 nm. The latter wavelength assures in principle eye safety and is particularly important for LIDAR applications. For these wavelengths, the GVD parameters for both pump and TH frequencies are close to each other. However, the wavevector mismatch strongly decreases from  $-5 \text{ cm}^{-1}$  (800 nm) to  $-0.65 \text{ cm}^{-1}$  (1550 nm), whereas the temporal walk-off parameter  $\Delta v = [v_g^{-1}(3\omega) - v_g^{-1}(\omega)]^{-1}$  increases from  $0.4 \text{ cm s}^{-1}$  to  $2.0 \text{ cm s}^{-1}$ , respectively. Consequently, the coherence length significantly augments at large wavelengths, which allows higher TH intensities and energy conversion efficiency.

More surprising features occur when the laser wavelength is selected in such a way that  $k''$  becomes negative and leads to anomalous dispersion. In that case, the pulse ceases to

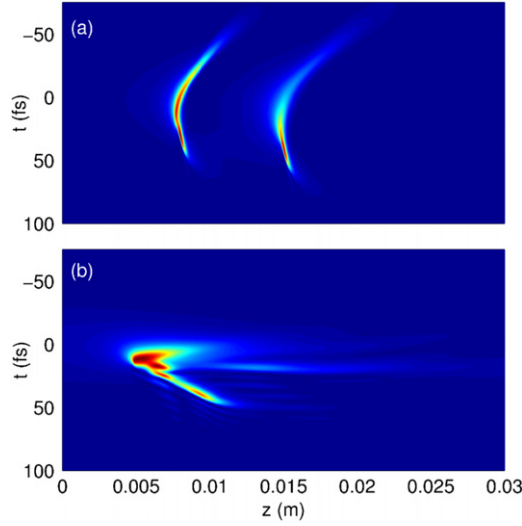


**Figure 16.** Temporal dynamics of 42.5 fs pulses with waist  $w_0 = 71 \mu\text{m}$  propagating in silica at the laser wavelength (a)  $\lambda_0 = 790$  nm with power  $P_{in} = 6P_{cr}$ , (b)  $\lambda_0 = 1550$  nm with  $P_{in} = 3P_{cr}$ . Note that the physical value of  $P_{cr}$  changes with  $\lambda_0$ .

be dispersed in time and undergoes a temporal compression, in addition to the spatial Kerr focusing. This happens, e.g. in fused silica at  $\lambda_0 = 1550$  nm, for which  $k'' \simeq -280 \text{ fs}^2 \text{ cm}^{-1}$  (see table 1). Recent experiments at this wavelength have shown that collapse events looked ‘extended’ along the  $z$ -axis, unlike the localized events promoted by normal GVD. Plasma halts the collapse at powers above critical, but anomalous GVD continues to transfer energy into the collapse region, resulting in the formation of longer filaments before the beam eventually defocuses (Moll and Gaeta 2004). The pulse can thus remain confined along several diffraction lengths and develops very narrow, isolated temporal peaks. A strong temporal compression produces optical spots whose duration is shrunk to the few-cycle limit (Bergé and Skupin 2005, Liu *et al* 2006a). Sharp shock profiles emerge from this 3D collapsing dynamics and pulse steepening along each focusing/defocusing event tremendously amplifies the blue part of the spectrum. Figure 16 displays the temporal distributions of a femtosecond filament created in fused silica at 790 nm ( $k'' = 370 \text{ fs}^2 \text{ cm}^{-1} > 0$ ) and at 1550 nm ( $k'' < 0$ ). At 790 nm, normal GVD stretches the pulse along the time direction. Conversely, at 1550 nm, anomalous GVD compresses it temporally. Third-order dispersion and self-steepening push the pulse centroid towards the region  $t > 0$ . Other works examining angle-frequency spectra in the normal/anomalous dispersion regimes are discussed in section 6.3. The arrest of 3D supercritical collapses in the self-channeling of ultrashort pulses should inspire more investigations in the future.

## 5. Ultrashort filaments in gases

This section is devoted to novel trends opened by the self-guiding of femtosecond pulses over small distances ( $< 1$  m), such as pulse shortening and high harmonic generation. Most of these applications are conducted in pressurized gas cells, in which the rise of plasma excitations can be controlled by changing the medium pressure.



### 5.1. Novel perspectives for pulse shortening

In the last decade, an important challenge has consisted of testing powerful techniques of ultrabroadband dispersion control, in order to compress pulses to durations of a few optical cycles only ( $\tau_{\text{o.c.}} = \lambda_0/c$ ). Ten years ago, Nisoli *et al* (Nisoli *et al* 1997a, 1997b, 1998) achieved the shortest pulse durations from  $\sim 1$  mJ, 20 fs pulses by manipulating the spectral broadening attained along a 60 cm long fused-silica hollow fiber filled with atomic (Ar, Kr) or molecular ( $\text{N}_2$ ) gases. Conditions for optimum pulse compression outlined an appropriate combination of SPM and gas dispersion managed by external chirped compensation systems. Pulses as short as 4.5 fs with output energies up to  $70 \mu\text{J}$  could be delivered at 800 nm and 1 kHz repetition rate after using a chirped-mirror delay line. The potential scalability of this system to higher pulse energies was claimed to hold provided that two conditions are fulfilled: (i) the laser peak power must be smaller than  $P_{\text{cr}}$ ; (ii) the peak intensity must not exceed the ionization threshold, to preserve a flat spectral phase for an efficient recompression. These two requirements could at that time be satisfied by a delicate tuning of the pressure parameter. For a gaseous medium with pressure  $p$ , the coefficients affecting equation (45a) indeed vary as follows:

$$k'' \sim p, \quad \beta^{(K)} \sim p, \quad P_{\text{cr}} \sim 1/n_2 \sim 1/p, \quad \rho_{\text{nt}} \sim p. \quad (76)$$

An optimal compression length can be estimated by  $L_{\text{opt}} \approx (6L_{\text{NL}}L_{\text{disp}})^{1/2}$  where  $L_{\text{disp}} \sim t_{\text{p}}^2/k''$  and  $L_{\text{NL}} \simeq n_2\omega_0 P_{\text{in}}/cS_{\text{eff}}$  are the dispersion and nonlinearity lengths, respectively, with  $S_{\text{eff}}$  being the effective area of the beam mode (Nisoli *et al* 1997a). This distance is tuned by the cell length and the local pressure  $p$ , in order to reach the smallest possible pulse duration. Stability of the beam was insured by selecting the  $\text{EH}_{11}$  hybrid mode with intensity  $I(r) = I_0 J_0^2(2.405r/a)$ , where  $I_0$  is the peak intensity,  $J_0$  is the zero-order Bessel function and  $a$  is the capillary radius (Tempea and Brabec 1998b). Keeping the beam stable inside the waveguide requires to limit the excitation of higher order modes owing to the nonlinear spatio-temporal dynamics. The spectral broadening thus inherently depends on how close the initial peak power of the beam is to  $P_{\text{cr}}$  (Homoelle and Gaeta 2000). Sub-10 fs pulses are routinely produced through similar techniques (Mével *et al* 2003, Steinmeyer *et al* 1999). A recent record reported pulses compressed to 3.4 fs (Yamane *et al* 2003).

In this scope, plasma generation may not constitute a drawback for pulse compression. Tempea and Brabec (1998a) mentioned the possibility of producing few-cycle optical pulses by compensating the spectral chirp generated by the plasma nonlinearity with a dispersive line delay for intense pulses propagating in filled-gas hollow fibers. This scenario was experimentally confirmed by a JILA team (Wagner *et al* 2004), who succeeded in compressing 30 fs pulses to 13 fs in hollow argon capillaries, even without any external dispersion compensation. It was recently improved to deliver 5 fs, high energy (1 mJ) pulses following the same scheme supplemented by amplifier systems and chirped-mirror compressors (Verhoeef *et al* 2006). In section 3, figure 7(d) recalled the basic property of pulse compression through the combined effects of Kerr nonlinearity and self-induced ionization. Chromatic dispersion and nonlinear losses, however, saturate the defocusing action of free electrons on the leading edge and enable the rear pulse to refocus at later distances. This produces a two-peaked temporal distribution whose time extent is often of the order of the input pulse duration. Achieving an efficient pulse compression, instead, requires to isolate one dominant peak shrunk in time (Champeaux and Bergé 2003).

To realize this challenge, Hauri *et al* used a configuration of two cascaded gas-filled cells with intermittent dispersion compensation for producing sub-mJ light pulses with durations down to 5.7 fs at  $\sim 800$  nm (Hauri *et al* 2004). The cells were operated at different pressures. It was later suggested that this scheme could be improved when a single cell with a pressure



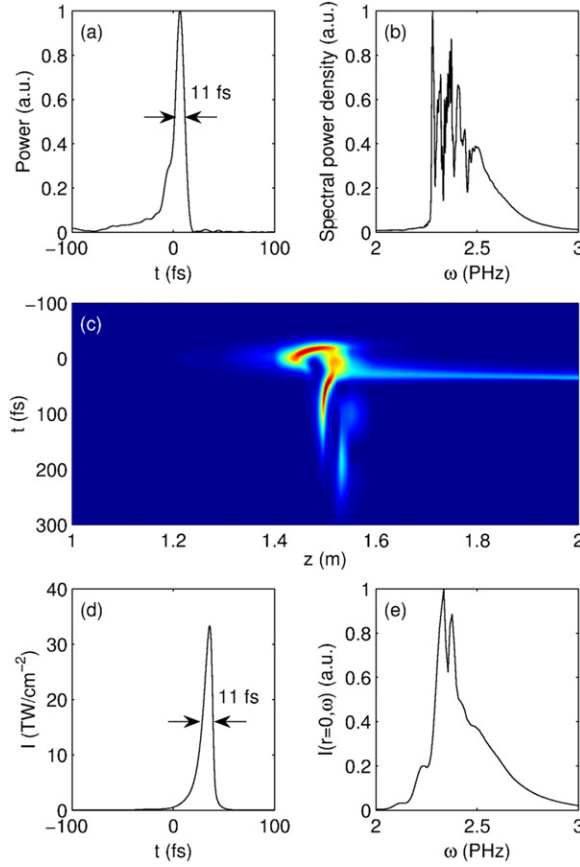


**Figure 17.** (a) Experimental pulse shape for the self-compression mechanism in a 50 kPa argon cell, (b) associated spectrum. (c) On-axis numerically computed temporal evolution of 45 fs pulses in the  $(t, z)$  plane for a similar setup. (d) On-axis intensity and (e) spectral intensity at  $z = 2$  m (exit window of the argon cell).

gradient is used instead, in order to monitor the refocusing stage of the trail and create waveforms with a single-cycle temporal signature (Couairon *et al* 2005, 2006a). Despite first results mainly directed to higher pulse energies (Suda *et al* 2005), further efforts are needed to adjust the pressure gradient for optimum compression to extremely short pulse duration. Alternatively, Stibenz *et al* (2006) recently demonstrated an efficient pure self-compression obliterating the need for any kind of dispersion compensation, pressure gradients or capillaries for beam guiding. The experimental setup involves beams in convergent geometry with energy up to 5 mJ,  $w_0 = 11$  mm,  $f = 1.5$  m, FWHM durations of 45 fs and input powers equal to 5 times critical. The beam is initially focused and propagates inside a 1 m long, 50 kPa argon cell whose center is positioned at the location of the geometrical focus. Output pulses reach durations down to about 10 fs and develop a strong blue-shift, as reported in figures 17(a) and (b). Figure 17(c) details this self-compression mechanism, reproduced numerically from equations (45a) and (45b). First, near  $z_c \simeq 1.45$  m, the front pulse focuses and plasma depletes its rear part. Second, at the linear focus ( $z \simeq 1.5$  m), the plasma density decreases, and the back pulse rises again. Finally, from  $z \simeq 1.6$  m, only the components close to the center, keeping intensity levels above  $10^{13}$  W cm $^{-2}$ , are effectively trapped in the filament, whereas the temporal wings diffract rapidly. A robust, temporally compressed

structure of 11 fs forms in the core region of the filament (figure 17(d)). The pulse center relaxes to a narrow ‘waveguide’, preserving its energy at low plasma density levels ( $<10^{14} \text{ cm}^{-3}$ ) after the linear focus. Figure 17(e) shows the on-axis intensity spectra, corresponding to this temporal compression. Not shown here, the spectral phase at the cell exit ( $z = 2 \text{ cm}$ ) becomes nearly flat in the blue wavelengths with tiny variations comprised in the same proportions as those measured by spectral phase interferometry for direct electric-field reconstruction (SPIDER). The robustness for this self-compression mechanism was numerically found to be limited to rather long  $f/w_0$  ratios and powers around  $5 P_{\text{cr}}$ , in order to avoid another focusing sequence (Skupin *et al* 2006b).

Let us mention that Chen *et al* (2006) also succeeded in achieving pulse self-compression from 50 to 20 fs, by making 800 nm pulses with energy  $<1 \text{ mJ}$  pass through a thin BK7 glass plate, with no subsequent dispersion compensation. SPIDER and spectral measurements revealed that self-compression takes place as long as the front pulse focuses while plasma cuts off the tail part. At this stage, the spectrum is marked by a strong redshift. By increasing the input peak intensity, the back pulse refocuses and blueshifts the spectrum. Accounting on the balance between plasma-induced negative chirps and SPM-induced positive chirps, the spectral output phase was, again, observed to be flat. All these methods represent new promising techniques to produce high energy few-cycle laser sources in the future.

Recently, Théberge and co-workers (2006a) reported the generation of few-cycle ( $\sim 10 \text{ fs}$ ) coherent sources in the visible spectral region, produced by four-wave mixing (4 WM) between a near-IR, mJ filament and a collinearly propagating  $\mu\text{J}$  seed pulse, emitted at different IR wavelengths. The output frequency of the generated pulse, determined by the relationship  $\omega_{4\text{WM}} = 2\omega_{\text{pump}} - \omega_{\text{seed}}$ , gives rise to visible ultrashort pulses in the range of 475 to 650 nm, which reach few-cycle durations after a post-compression stage. Up to 40% of the IR seed can be converted into the new tunable source, over cm as well as metre-scale propagation distances in various gases (argon, air). These tunable ultrashort pulses have very low energy fluctuations and exhibit an excellent mode quality due to the process of intensity clamping and self-filtering in the filament. Delivering few-cycle pulses being agile in wavelength can be of benefit to photochemistry, photobiology and other important fields of applications. Figure 18(a) shows the conversion efficiency of generated 4 WM pulses in air and argon for different IR seed pulses. Figure 18(b) details their normalized spectra generated in air across the tuning range. Figures 18(c) and (d) display an example of the normalized 4 WM pulse spectrum and its transform-limited time profile.

## 5.2. High-order harmonic generation

The possibility of reducing pulse durations to a single optical cycle provides ideal conditions for high harmonic generation and laser-assisted x-ray photo-ionization (Drescher *et al* 2001). Several fundamental atomic processes such as inner-shell electronic relaxation or ionization take place within a fraction of the oscillation period of visible or near-infrared radiation and they require very short probes for being investigated. For this purpose, bursts of attosecond pulses ( $1 \text{ as} = 10^{-18} \text{ s}$ ) need to be isolated. This is now feasible by combining single bursts emitted at extreme ultraviolet (XUV) wavelengths and ultrashort lasers, in order to preserve the coherence properties at such short time scales. In this microcosm, the ionization processes become crucial, and more particularly the transient stage of about half laser period along which an electron is liberated. Developments in attosecond x-ray science have been addressed in several excellent reviews (Brabec and Krausz 2000, Pfeifer *et al* 2006, Scrinzi *et al* 2006). Subfemtosecond light pulses down to 130 as in duration can be experimentally obtained by making several high harmonics emit synchronously (Mairesse *et al* 2003).

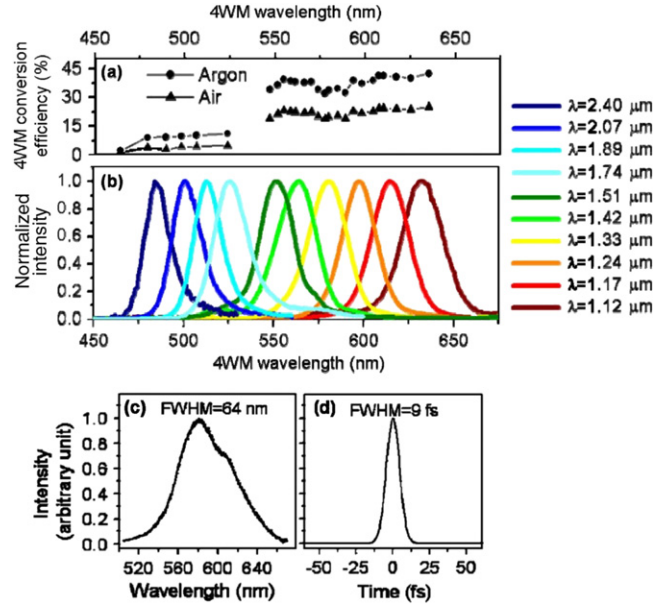


**Figure 18.** (a) 4 WM conversion efficiency of a seed pulse coupled to a near-IR filament in air and in argon. (b) Generated 4 WM pulse spectrum for different wavelengths of the seed pulse. (c) and (d) Examples of normalized 4 WM pulse spectrum and associated duration in air (Th  berge *et al* 2006a). Courtesy of Th  berge.

High harmonic generation (HHG) describes the process by which laser light at central frequency  $\omega_0$  is converted into integer multiples of  $\omega_0$  during the highly nonlinear interaction with the medium. In 1993, Corkum (1993) proposed a quasi-classical theory for this process, which can be divided into three steps.

- (i) The electron is freed by ionization and driven away from the parent ion.
- (ii) Since the laser field changes its sign over times about  $\tau_{0.c.}/2$ , this electron slows down, stops at a certain position and then re-accelerates towards the ion.
- (iii) When the electron recombines with the nucleus, a photon with energy equal to  $U_i$  plus the electron kinetic energy is emitted. This gives rise to high harmonic orders.

Figure 19 illustrates a typical HHG spectrum. The harmonic intensity rapidly decreases after an almost flat plateau ( $\lambda < 15 \text{ nm}$ ). It is terminated by a cut-off, signaling the highest harmonics that can be generated. Among all possible electron trajectories, there indeed exists a maximum kinetic energy corresponding to the maximum photon energy absorbed by this process. Numerically solving for the electron trajectories leads this maximum kinetic energy to be  $\sim 3.17 \times U_p$  (Corkum 1993, Zeng *et al* 2003). Here,  $U_p = q_e^2 E_p^2 / 4m_e \omega_0^2$  denotes the ponderomotive energy of the electron in the wave field (see appendix B). Electrons thus produce harmonic photons up to the cut-off energy

$$\hbar\omega_c = 3.17 \times U_p + U_i. \quad (77)$$

The laser pulses employed in HHG experiments are generally short ( $< 40 \text{ fs}$ ), with the elementary profile  $E(t) = E_0 \cos(\omega_0 t + \varphi_{CE})$ , where the carrier-envelope phase  $\varphi_{CE}$  becomes an important parameter for the conversion efficiency into HHG when approaching the optical cycle (Srinzi *et al* 2006).

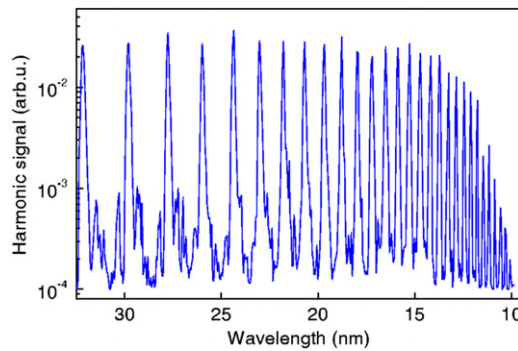


**Figure 19.** Harmonic spectrum generated in neon by a 800 nm Ti : Sa laser. 25th to 81st harmonics are displayed (Salières and Lewenstein 2001). Courtesy of Salières.

In ionized media with symmetry inversion, harmonic peaks exist only at odd integer multiples of  $\omega_0$ . The above three-step process repeats every half-cycle of the laser field, so that the Fourier sum in the spectra makes even harmonics cancel each other along one cycle. The analytical description of this process requires a quantum-mechanical approach of the dipole moment associated with the harmonics. To this aim, Lewenstein *et al* (1994) derived the time-dependent dipole moment  $\vec{d}(t) = q_e \langle \psi(\vec{r}, t) | \vec{r} | \psi(\vec{r}, t) \rangle$  that represents the expected position of the electron in the quantum state  $|\psi(\vec{r}, t)\rangle$ . Details for computing  $\vec{d}(t)$  have been given in appendix C. The dipole takes into account ionization at time  $t'$ , energy gain computed from a phase integrand and recombination at time  $t$ . Stationary phase conditions yield information about the electron trajectories. By Fourier transforming the dipole moment, the harmonic spectrum can be calculated and it restores the cut-off law (77).

The challenging issue is then to describe HHG by accounting for the propagation physics of ultrashort pulses having initially a few fs durations. Lange *et al* (1998a) employed self-guided fs pulses to produce HHG up to the 15th harmonic in noble gases and maintain the longitudinal coherence of the generated harmonics. Tamaki *et al* (1999) demonstrated experimentally efficient HHG through the phase-matched propagation of laser beams in pressurized Ne with peak intensities up to  $10^{15} \text{ W cm}^{-2}$ . By changing the propagation length, phase-matching magnifies the conversion efficiency around the 49th harmonic by 40 times near the cut-off region. Tosa *et al* (2003) reported the H13 harmonic triggered by the self-guided propagation of a focused pulse inside a 14 cm long cell filled with Xe, in which the Kerr response was negligible. More recently, direct evidence of laser filamentation was recorded under conditions optimized for generating high harmonics in He gas cells (Painter *et al* 2006). Harmonics 45 to 91 were kept phase matched over many millimetres between two focusing cycles. From these results, we easily guess that the next step in ‘attosecond’ investigations should concern the optimization of HHG spectra by means of self-compressed filaments. The promising feature of pulse shortening induced by the balance Kerr/plasma could become an excellent technique to produce an isolated XUV pulse. Moreover, the ability to keep the laser pump clamped at sufficiently high intensity over several centimetres may magnify the harmonic signal. For instance, figure 20 illustrates the amplitude of the atomic dipole computed numerically for a plane-wave pulse traversing an argon cell pressurized at 60 kPa for two different pump intensities. The HHG spectrum becomes magnified at intensity levels close to  $100 \text{ TW cm}^{-2}$ . Besides, numerically solving the dipole moment using spatio-temporal profiles of filaments recently indicated that self-compression can improve the time structure and collimation of the XUV radiation (Chakraborty *et al* 2006). These preliminary results

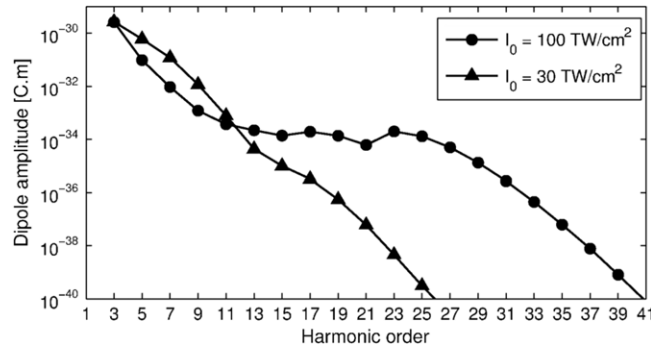


**Figure 20.** Harmonic spectrum computed from the dipole moment  $\vec{d}(t)$  in pressurized argon for two different pump intensities.

give us confidence for obtaining optimized harmonic signals and confined attosecond pulses at high energy level by means of self-compressed filaments.

## 6. Ultrashort filaments in dense media

Below, we review the major physical aspects of ultrashort filaments in solids and in liquids.

### 6.1. Pulse propagation in dielectrics and damages

Transparent dielectrics such as  $\text{SiO}_2$  samples were routinely examined during the 1990s, in the frameworks of the optical breakdown (see section 4) and of the carrier trapping dynamics of band-gap crystals. One of the key parameters being the potential gap (which is the energy difference between valence and conduction band), several investigations were led to identify this gap in silicon dioxide and to measure the ultrafast excitation and relaxation of an electron gas pumped into the conduction band by intense fs laser pulses (Audebert *et al* 1994, Martin *et al* 1997, Tohmon *et al* 1989).

Meanwhile, other studies concerned laser-induced breakdown (LIB) in dielectrics. The threshold damage fluence varying as  $\sqrt{t_p}$  for long pulses in thermal conduction regimes was seen to deviate from this scaling with fs pulses, for which electrons have no time to efficiently couple to the lattice. Du *et al* (1994) reported a damage threshold fluence higher than the  $\sqrt{t_p}$  prediction rule for pulse durations  $< 10$  ps. They furthermore underlined that short-pulse damage exhibits a deterministic nature, unlike long pulses. A theoretical model accounting for MPI, avalanche ionization and Joule heating stressed the dominant role of photo-ionization at fs time scales (Stuart *et al* 1996). However, both photo-ionization and avalanche come into play during the occurrence of damage. Although the role of the former is initially dominant (Rayner *et al* 2005), it can be masked by an avalanche from an initially high electron density ( $> \rho_c/100$ ) (Tien *et al* 1999). To complete these two processes, the rapid electron decay over  $\sim 100$  fs scales through recombination softens the maximum electron density for LIB (Li *et al* 1999).

Investigations mixing propagation and damage in dielectrics started from the early 2000s. Tzortzakis *et al* (2001d) observed the 1 cm long self-channeling of a 160 fs focused pulse conveying 3 critical powers at 800 nm. The pulse traveled across a fused silica sample like a narrow waveguide with a  $\sim 20 \mu\text{m}$  waist. Local heating caused by the high repetition rate (200 kHz) and damage by local intensities  $> 10 \text{ TW cm}^{-2}$  were avoided by making the sample

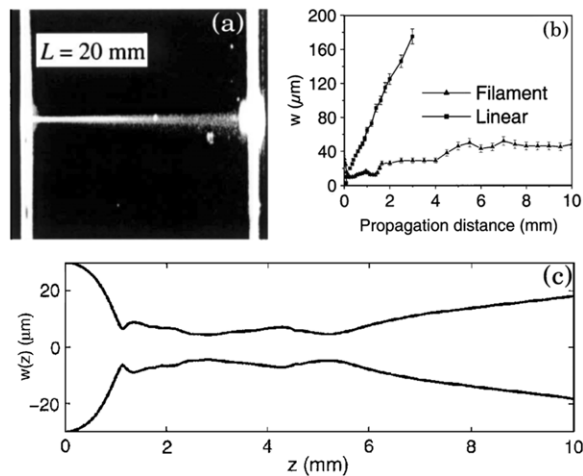


**Figure 21.** (a) Transverse photograph of a single filament propagating (from left to right) in fused silica. (b) Measured diameter of the beam comparing high (linear) and low (nonlinear) divergences. (c) Numerically computed diameter of the nonlinear filament (Tzortzakis *et al* 2001d).

move in the  $(x, y)$  plane. Auto-correlation traces revealed a two-peaked structure and spectra were asymmetrically broadened, which signaled a pulse splitting driven by plasma. Earlier, Brodeur and Chin (1999) noticed a similar supercontinuum in glasses and explained it from the multiphoton excitation of electrons into the conduction band at the focus point. The low beam divergence was attributed to the Kerr-lens effect. As an example, figure 21(a) shows a transverse photograph of the self-guided filament measured at input energy of  $2 \mu\text{J}$  in fused silica. Figure 21(b) details the filament waist in the nonlinear propagation regime and figure 21(c) reproduces this waist numerically computed from equations (45a) and (45b).

At higher local intensities, the breakdown limit is approached. Because the plasma generated during breakdown remains at the threshold, a precise control of the interaction region can be reached with ultrashort pulses. This property can be used for material processing, medical laser applications as well as solid-state microelectronics. The major qualitative differences between damages caused by short ( $< 10 \text{ ps}$ ) and longer pulses ( $> 50 \text{ ps}$ ) appear in the damage morphology: short pulses ablate the material, whereas long pulses produce conventional melting, boiling and fracture. With tightly focused fs pulses, permanent birefringent structures embedded in bulk fused silica have been realized over microscopic dimensions (Sudrie *et al* 1999, 2001). Arrays of parallel grooves formed transmission diffraction gratings with periodically modified index changes. Two distinct types of damages can be created, namely, those consisting of local isotropic increase of the refractive index at subcritical powers, and those inducing local birefringence at powers above critical. The damage track consists of diffusing zones of  $\sim 20 \mu\text{m}$  transverse width. The total damage region can extend over a distance reaching  $80 \mu\text{m}$  along the optical path. Numerical simulations accounting for photo-ionization, avalanche, electron recombination and Kerr self-focusing reproduced experimental damage tracks (Sudrie *et al* 2001, 2002). Electron densities up to  $3 \times 10^{20} \text{ cm}^{-3}$  resulted from the combined actions of photo- and impact ionization. Accounting moreover for Ohmic heating and thermal cooling by collisional ionization, Peñano *et al* (2005) numerically solved the 1D electromagnetic wave equation to quantify the transmission, reflection and absorption of 100 fs laser pulses by a thin plasma layer formed at the surface of



a dielectric. With a fluence of  $3.2 \text{ J cm}^{-2}$ , the interaction fully ionizes the surface and heats the plasma to  $\sim 10 \text{ eV}$ . A significant transmission up to 30% of the laser energy is possible even when the plasma density is above critical ( $\omega_{pe} > \omega_0$ ). In the layer, the electron density becomes supercritical and implies a sharp rise in the reflected pulse amplitude. Compared with MPI alone, collisional ionization increases the plasma density by 30%.

## 6.2. Pulse propagation in liquids and applications

Similarly to LIB in solids, the optical breakdown in fluids gained considerable interest, because it finds various therapeutic applications for, e.g. plasma-mediated laser surgery and prevention of ocular damage. First simulations in water (Feng *et al* 1997) emphasized the dominant role of cascade ionization for long pulses, while multiphoton ionization was expected to prevail for shorter pulses. Further studies (Noack and Vogel 1999) evaluated the absorption coefficients during the LIB process for 100 ns down to 100 fs pulses. It was established that a critical density threshold for LIB was  $\rho_{cr} = 10^{20} \text{ cm}^{-3}$  for long (ns) pulses, but  $\rho_{cr} = 10^{21} \text{ cm}^{-3}$  for short (ps) ones. In water and for 100 fs durations, LIB results in bubble formation supported by thermoelastic effects at pulse powers above the self-focusing threshold. This process also causes refractive index changes in the beam path upstream over several hundreds of microns. Within water droplets the tight focusing and the nonlinearities of the LIB process moreover generate a nanosized plasma hot enough to emit in the visible, and preferentially in the backward direction (Favre *et al* 2002).

The first experiments on fs pulse self-guiding versus the optical breakdown limit in water were performed by Liu and co-workers for different focusing geometries (Liu *et al* 2002). It was found that the shorter the focal length, the larger the transverse size of the optical breakdown plasma. Self-focusing drives the initial localization of the plasma towards the beam axis. White-light is generated along a short ( $< 1 \text{ mm}$ ) filament and deflected at a small constant angle only. The supercontinuum sources for the high frequencies were identified in the rings formed by plasma defocusing and amplified by the back of the pulse, where shocklike dynamics blueshift the spectrum (Kandidov *et al* 2003, 2004). This scenario applies to pulses with peak power rather close to critical.

Increasing the pulse power further leads to multiple filamentation, which has been addressed in a few papers (Cook *et al* 2003, Heck *et al* 2006, Schroeder *et al* 2004). By using a cylindrical planoconvex lens, Cook *et al* produced horizontal arrays of stable white-light filaments in water at 800 nm, allowing interference effects between neighboring cells. Similarly to a pair of Young's slits, a filament pair creates interference patterns, which is the signature for a constant phase relationship between the supercontinua generated by the filaments (the same property applies to atmospheric filaments; see section 7.1.4). They thus appear as coherent sources of white light. Besides, Schroeder *et al* demonstrated the possibility of arranging filaments into 1D arrays of parallel, nonoverlapping spots by clipping the impinging laser beam by a slit aperture built from razorblades. Metallic wire meshes can also be used to generate space-controlled 2D arrays of filaments. Recently, Heck *et al* demonstrated the efficiency of an adaptive control over the position and extent of filaments in water tanks, through a closed feedback loop setup employing a spatial light modulator and a genetic algorithm that allow manipulation of the amplitude and phase of the input pulse.

Apart from water, other fluids can support femtosecond filamentation, such as alcohols like ethanol or methanol. Dyes may be introduced into these liquids, in order to visualize the filamentary evolution through one, two or three-photon fluorescence and modify the multifilamentation patterns by varying the dye concentration (Guyon *et al* 2006, Liu *et al* 2003, 2005a, Schroeder and Chin 2004). Relying on the dye nonlinear absorption, the



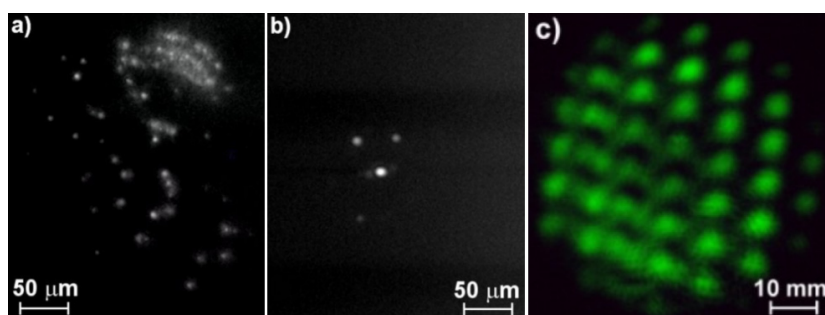


**Figure 22.** Filamentation pattern obtained from a 1 cm long cell of (a) pure ethanol, (b) dilute solution of ethanol/coumarin 153 at  $4 \text{ g L}^{-1}$ , (c) far-field fluence distribution of excited states of coumarin emitting simultaneously in phase.

structural changes of the filamentation become visible to the eyes, due to the fluorescence from the dye molecules excited by multiphoton excitations at visible wavelengths. From a dilute solution of methanol and rhodamine B, Schroeder and Chin figured out that femtosecond filaments propagate straight, may die off prematurely or fuse into new spots. Along the propagation axis, ‘mature’ filaments ending after the bright fluorescence zone were identified. By means of the same techniques, Liu *et al* observed multi-focusing events by increasing the beam energy in methanol doped with 0.13% of coumarin 440 at 800 nm. The photon bath surrounding the  $20 \mu\text{m}$  large filament core was numerically examined. It was found that the near-axis region takes energy from a ring-shaped region limited to  $r < 60 \mu\text{m}$  around the filament core. Outside, the peripheral domain ( $r > 60 \mu\text{m}$ ) acquires energy. The resulting energetic balance preserves an almost constant energy in the near-axis region. Nonlinear fluorescence techniques were recently used to discriminate between multiphoton absorption and conical emission by  $z$ -scan analysis using metal meshes (Liu *et al* 2005a). It appears that the energy loss caused by conversion into CE (40%) is much higher than that caused by MPA ( $\sim 3\%$ ) at powers  $< 8P_{\text{cr}}$  (see also section 4.1). Finally, Guyon *et al* employed coumarin 153 in dye-doped cells of ethanol. At high dye concentration ( $4 \text{ g L}^{-1}$ ), the filamentation pattern was shown to self-organize into a latticelike (hexagonal) figure, by letting the two-photon absorption of coumarin switch out filamentary sites in the  $(x, y)$  plane. Pump-dump experiments furthermore revealed that, at all filamentary sites, excited coumarin molecules could coherently relax by fluorescence and emit in-phase light stimulated by the dump pulse, i.e. a collection of filaments can be used as microscopic laser sources in dense media. Figure 22 summarizes some of these observations.

### 6.3. X/O waves and far-field spectra

Far below LIB limits, the self-guided propagation of femtosecond filaments in water was thoroughly examined by Dubietis, Di Trapani and their collaborators a few years ago (Dubietis *et al* 2003). By launching a  $\sim 3 \mu\text{J}$ , 170 fs clean beam with  $\sim 100 \mu\text{m}$  FWHM diameter onto a water-filled cuvette in loosely focused ( $f \geq 5 \text{ cm}$ ) geometry, a single filament formed at the wavelength of 527 nm. It was capable of covering up to 4 cm along the propagation axis, while keeping a mean FWHM diameter of a few tens of  $\mu\text{m}$ . The filament dynamics was not sustained by a balance between Kerr self-focusing and plasma-induced defocusing. Numerical simulations outlined, instead, the spontaneous reshaping of the beam into a Bessel-type X-wave fulfilling the requirements of minimum nonlinear losses, maximum

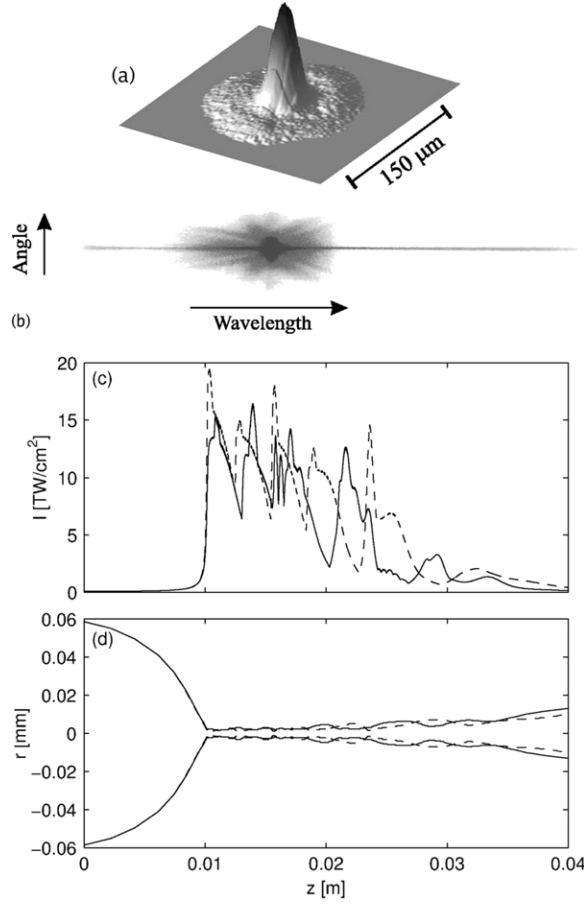


**Figure 23.** (a) Normalized 3D beam profile at the output of the water cell (31 mm); (b) spectral-angular distribution of the radiation (Dubietis *et al* 2003). Courtesy of Dubietis. (c) Peak intensities computed numerically with (—) and without (---) plasma gain from 170 fs, 100 μm-waisted pulses focused with  $f = 5$  cm ( $P_{\text{in}} = 10 P_{\text{cr}}$ ) in water; (d) corresponding FWHM radius.

stationarity and localization (see section 4.1). For this purpose, figure 23(a) illustrates the pulse fluence along the self-guiding range measured at the exit plane of a 31 mm long cuvette for  $P_{\text{in}} = 6.6 P_{\text{cr}}$ . Figure 23(b) shows the X-shaped spectral-angular distribution of the radiation. Plots (c) and (d) represent peak intensities and FWHM diameters reached from similar pulse parameters with and without plasma gain. They evidence the weak influence of plasma defocusing in this dynamics (Kolesik *et al* 2004, Skupin *et al* 2006a).

The conical emission (CE) develops an X-like angular distribution of wavelengths in the far-field. Early interpretations of this phenomenon favoured a spatio-temporal modulational instability leading to hyperbolic or elliptic contours in the angle-frequency plane for normal or anomalous dispersion, respectively (Liou *et al* 1992, Luther *et al* 1994c). In contrast, recent analyses, either theoretical or experimental, reported the important influence of chromatic dispersion and phase-matching conditions (Conti *et al* 2003, Dubietis *et al* 2004a, 2003, Faccio *et al* 2007, Kolesik *et al* 2003a, 2004, Porras *et al* 2004). Created from ultrashort filamentary pulses, nonlinear X waves are conical waves being stationary, nondispersive and

nondiffracting along the propagation axis (Conti *et al* 2003). The filamentation dynamics and the X-shaped spectrum observed in the plane  $(k_{\perp}, \omega - \omega_0)$  are explicit manifestations of these nonlinear X waves (Couairon *et al* 2006b, Faccio *et al* 2005a, 2005b). Therefore, Kolesik *et al* (2004, 2005) proposed that angle-resolved (far-field) spectra can provide efficient experimental diagnostics, as their characteristic patterns reflect in detail the complex dynamics of femtosecond pulses. The double X shapes ‘marking’ the frequency-resolved spectrum depend on the relative velocities of the leading/trailing optical peaks resulting from the nonlinearities. Their slope and mutual shifts, which look quasi-stationary along the filament path, may yield quantitative information on the nonlinear evolution of the pulse. In anomalous GVD regimes, counterparts of X waves are O waves, which, instead of hyperbolae, generate elliptic lines in the angle-frequency spectrum (Porrás *et al* 2005).

Several investigations have been devoted to quantifying the X/O contours characterizing the  $(k_{\perp}, \bar{\omega})$  surfaces in a rich variety of media (Faccio *et al* 2005b, 2006a, 2006b, 2006c, Kolesik *et al* 2005, Porrás and Di Trapani 2004, Porrás *et al* 2005). Here,  $k_{\perp}$  is the transverse wave number of the mode and  $\bar{\omega} = \omega - \omega_0$  denotes the detuning between the generated frequency and that of the pump wave. The propagation angle with respect to the longitudinal axis is defined by  $\theta \equiv k_{\perp}/k_0$  and it was proposed to have the simple analytical form (Longhi 2004, Porrás and Di Trapani 2004)

$$\theta = \sqrt{\frac{2}{k_0}(\beta + \alpha\bar{\omega} + \hat{D})}, \quad (78)$$

where  $\hat{D}$ , defined by equation (20), stands for chromatic dispersion. The parameters  $(\beta, \alpha)$  originate from the longitudinal wave number  $k_z(\bar{\omega}) = k_{z0} + k'_{z0}\bar{\omega}$ , where the quantities  $k_{z0} = k_0 - \beta$  and  $k'_{z0} = k'_0 - \alpha$  determine the propagation constant and group velocity of the X/O mode. Equation (78) follows from a direct expansion of the transverse dispersion relation  $k_{\perp} = \sqrt{k^2(\bar{\omega}) - k_z^2(\bar{\omega})}$ , where  $k(\bar{\omega}) = \sqrt{\epsilon(\bar{\omega})}\bar{\omega}/c$  contains all information about the material dispersion. Rather good agreements between equation (78) and experimental CE spectra can be obtained in the limit of large frequency shifts (Faccio *et al* 2006c). Difficulties in fitting equation (78) with experimental spectra, however, still prevent an accurate identification of the couple  $(\alpha, \beta)$  in the presence of nonlinearities (Faccio *et al* 2006b). Evaluating the parameter  $\alpha$  is currently achieved from visual inspection of numerical data in the propagation range where the pulse splits into leading and trailing peaks: two daughter waves have different group velocities, which create distinct lines in the  $(k_{\perp}, \bar{\omega})$  plane. This approach meets the three-wave mixing scenario proposed in Kolesik *et al* (2004, 2005), following which the X/O modes with frequency  $\omega$  are generated from the scattering of a wave created at frequency  $\bar{\omega}$  by the material nonlinear response with the pump wave at  $\omega_0$ . The angular spectrum then results from the phase-matching condition

$$k_z(\bar{\omega}) \simeq k_z(\omega_0) + \frac{\bar{\omega}}{v_r}, \quad (79)$$

which identifies the longitudinal wave numbers of the input and output waves, up to the ratio of  $\bar{\omega}$  over the group velocity  $v_r$  acquired by the response peak along the filament path. Different X arms correspond to different daughter pulses having their own group velocity.

Angular far-field spectra open novel opportunities for capturing the nonlinear pulse dynamics. They will certainly reach a high impact in the field of nonlinear focusing and supercontinuum generation when, e.g. the inverse problem of directly mapping the nonlinear response from the far-field spectrum is resolved. For example, figures 24(a) and (b) show X/O patterns experimentally measured in water from the angle-wavelength spectra of self-focused 1 ps pulses at 527 nm ((a) X waves) and at 1055 nm ((b) O waves) (Porrás *et al* 2005). For

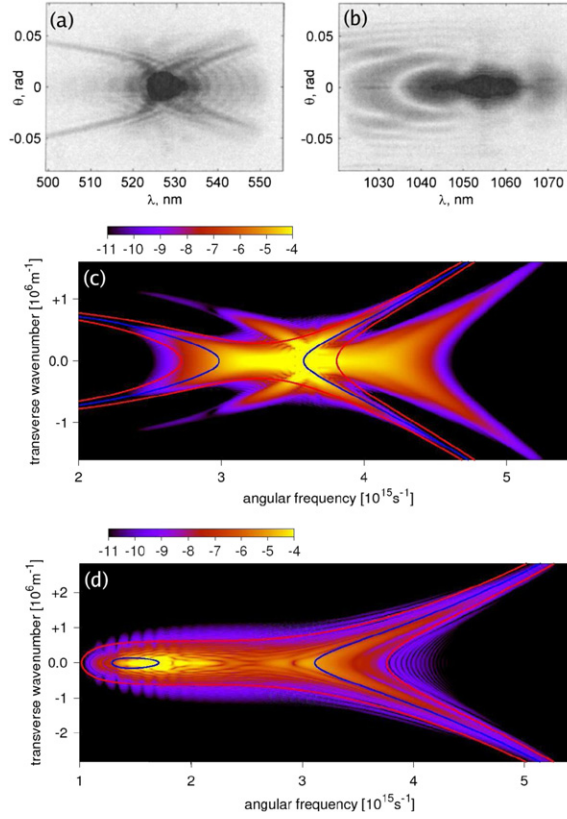


**Figure 24.** Experimental angle-wavelength spectra of pulses at 527 nm in water: (a)  $\lambda_0 = 527$  nm,  $E_{\text{in}} = 1.6 \mu\text{J}$ ; (b)  $\lambda_0 = 1055$  nm,  $E_{\text{in}} = 14.5 \mu\text{J}$  (Porrás *et al* 2005). Courtesy of Dubietis. (c) Logarithmic far-field spectra of a 94 fs pulse with  $0.6 \mu\text{J}$  energy at 527 nm. (d) Same with  $2.3 \mu\text{J}$  energy at 1100 nm. Courtesy of Kolesik. Phase-matched regions induced by the leading peak of the nonlinear response are shown (Kolesik *et al* 2005).

comparison, figures 24(c) and (d) display quite similar logarithmic far-field spectra for close laser beam parameters. Lines indicate phase-matching regions (equation (79)) for the leading peak emerging in nonlinear self-focusing regime. The conical component prolonging the elliptic distributions at high frequencies concerns the part of the spectrum that extends deep into the normal GVD region.

Similar dynamics were reported in fused silica (Polesana *et al* 2006), where nonlinear Bessel beams experience a spontaneous reshaping due to the combined action of self-focusing and nonlinear losses. Besides, recent experiments using  $\chi^{(2)}$  crystals have led to the introduction of the novel concept of X-shaped spatiotemporal coherence, skewed along specific X-like trajectories in space and time (Jedrkwicz *et al* 2006). While nonlinear X waves are inherently localized structures, the pulse spectrum can exhibit specklelike substructures reflecting the partially incoherent nature of the total field.

## 7. Filaments in the atmosphere: conveying intense structures over kilometres

The final section is devoted to the medium which originally served as the ‘birthplace’ for the science of femtosecond light filaments, namely, the atmosphere. Special emphasis is laid on

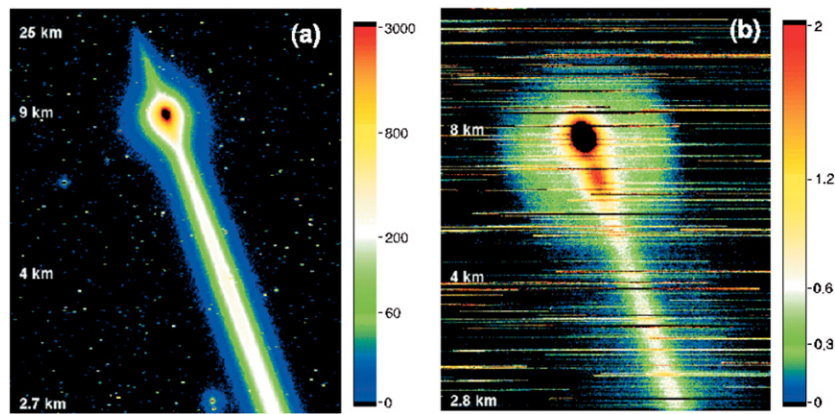


**Figure 25.** Typical fs beam image of the Teramobile laser beam from Tautenburg observatory. (a) Fundamental wavelength; (b) blue–green band of the continuum. The horizontal stripes across the pictures come from stars passing through the telescope field of view. Note the strongly nonlinear altitude scale due to triangulation.

experimental diagnostics. From the theoretical point of view, filamentation in air is modeled from equations (45a) and (45b), using classical dispersion relation in air (Peck and Reeder 1972). Although of weaker percentage (20% versus 80% in air), dioxygen molecules have a lower ionization potential than nitrogen and they provide the dominant species prevailing through ionization (Couairon *et al* 2002).

### 7.1. Long-distance propagation and white-light supercontinuum

**7.1.1. Temporal chirping and spatial lensing.** The propagation of high power femtosecond laser pulses in air has attracted considerable attention from the pioneering observation of the white-light supercontinuum beyond 10 km (Wöste *et al* 1997). A number of important practical applications have been suggested, including remote sensing (Rairoux *et al* 2000), directed energy delivery and artificial lightning (LaFontaine *et al* 1999a) among others. Because the filament onset and length are key parameters for spectroscopic measurements and for depositing high intensities on remote targets, monitoring these parameters is of utmost importance. To achieve high intensities at remote distances, a negative frequency chirp can be introduced in the laser pulse (Alexeev *et al* 2004, Wille *et al* 2002). In addition to transverse self-focusing, the pulse undergoes a temporal compression as it compensates the normal group-velocity dispersion along the propagation axis. Chirping effects can be measured by evaluating differences in the conical emission with and without pulse chirping (Rodriguez *et al* 2004). For instance, the vertical propagation of the Teramobile beam, presented in appendix D, was examined from the ground using the 2 m astronomical telescope of the Thüringer Landessternwarte (Thuringia State Observatory, Germany). Collected images were a combination of both (i) cross-section images of the beam impinged on the bottom of clouds or haze layers acting as screens, and (ii) side imaging of the Rayleigh-scattered light over large altitude ranges. Some of these images are shown in figure 25 at both the fundamental wavelength and the white-light continuum. In this case, the altitude was retrieved using triangulation. Figure 25(b) demonstrates the efficiency of the supercontinuum generation, since its blue spectral signal has been detected from altitudes beyond 18 km for appropriate chirping. These experiments showed for the first time the possibility of delivering high intensities and

generating white-light upon variable km distances, by means of GVD/chirp precompensation techniques. The same observation assessed that the conical emission bears two-thirds of the overall white-light energy, while the on-axis, forward-directed central component carries the remaining one-third.

To modify the filamentation distance, a chirp is usually introduced by changing the distance between the gratings of CPA laser compressors. Applied to the Gaussian pulse (46), this technique modifies the second-order phase contribution  $\varphi'' = d^2\varphi/d\omega^2|_{\omega=\omega_0}$  through the chirp parameter  $C$ . It enhances the input pulse duration and decreases the beam power as

$$t_p^C = t_p^{C=0} \sqrt{1+C^2}, \quad P^C = P^{C=0} / \sqrt{1+C^2} \quad (80)$$

at equal spectral content. As it linearly propagates, the pulse competes with normal GVD and reaches the minimal duration  $t_{\min} = t_p^{C=0}$  at the distance

$$z_{\min} = \frac{|C|}{1+C^2} \frac{t_p^2}{2k''}. \quad (81)$$

Pulse chirping mixes two essential modifications. The first one is dictated by the phase  $\sim e^{-iCr^2/t_p^2}$ . For input powers above  $P_{\text{cr}}$ , a positive chirp  $C > 0$  delays the occurrence of the self-focus point, whereas this occurs earlier along the optical path for a negative chirp ( $C < 0$ ). The second one results in diminishing the effective pulse power, which pushes the first focus to later propagation distances and reduces the number of filaments in the case of multifilamentation, whatever the sign of  $C$  may be. In usual experimental conditions, this second effect prevails over the first one. Despite the strong nonlinearities driving the filament dynamics, the chirped-induced linear compression still persists with  $C < 0$ . It gives rise to additional focusing events and keeps the beam localized at distances close to  $z_{\min}$  (Golubtsov *et al* 2003, Nuter *et al* 2005). Moreover, the generation efficiency of the supercontinuum may vary by several orders of magnitude compared with that of a transform-limited pulse.

The onset distance and longitudinal extent of filaments are also conditioned by the initial spatial focusing geometry. No simple analytical rule exists on this point, because of the complex spatial distortions destroying the initial homogeneity of the beam. The filament length, moreover, depends on the energy consumed by plasma excitation and on the accessible peak intensity. However, most of the experiments emphasize the use of rather large ratios  $f/w_0$ , in order to avoid an immediate plasma defocusing in a tightly focused configuration (Théberge *et al* 2006b). This property can be refound by integrating the dynamical equations derived from the two-scale variational method (equation (55)) (Champeaux and Bergé 2005). The variational principle indicates that at given  $P_{\text{in}}/P_{\text{cr}}$  the ratio  $f/z_0$  must be large enough to ensure the self-trapping condition  $z_c \leq f$ . Otherwise, for  $f/z_0 \ll 1$ , the beam diffracts just after the focal point. Figure 26(a) shows the beam diameter of 100 fs, 1 mm waisted pulses in air at  $P_{\text{in}} = 10 P_{\text{cr}}$  and various focal lengths  $f$ , which confirms the previous belief. Figure 26(b) represents the beam extent along the  $z$  axis of temporally chirped pulses with waist  $w_0 = 3$  mm, input energy of 1.9 mJ and the same power ratio, for which  $t_p^C = 100$  fs while  $t_p^{C=0} = 70$  fs.

**7.1.2. Plasma and optical field measurements.** Plasma detection relies on the existence of a difference of potential produced by the current generated by ionization of air molecules. Working in a free atmospheric medium makes it easy to measure the conductivity of the plasma channel, which causes a drastic reduction of air resistivity after the passage of a self-guided filament. This conducting column can be directly evidenced by letting the filament pass between two copper electrodes drilled in their center and between which a dc voltage



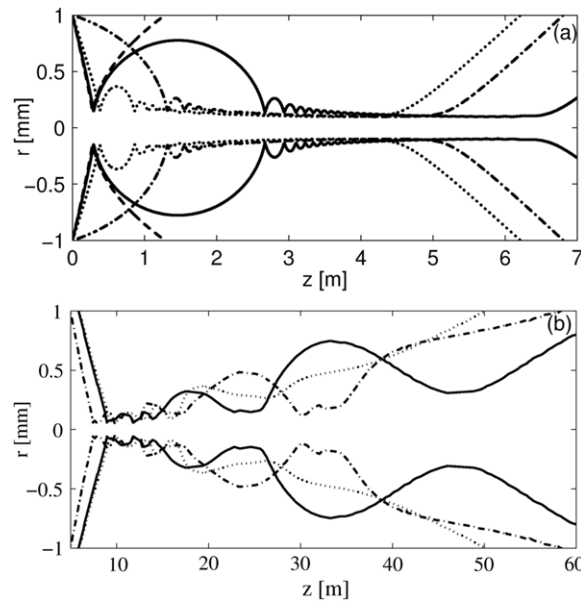


**Figure 26.** (a) Beam diameter of pulses spatially focused with  $w_0 = 1$  mm,  $f = 35$  cm (---),  $f = 37$  cm (—),  $f = 50$  cm (.....),  $f = 5$  m (— · —). Results follow from a two-scale variational approach. (b) Beam diameter versus  $z \geq 5$  m for temporally chirped, 3 mm waisted pulses with  $C = 0$  (— · —),  $C = 1.02$  (.....) and  $C = -1.02$  (—). Results are obtained from numerical integrations of the NEE model.

of typically 1000 V is applied (see figure 27). The current circulating through the plasma column is then measured by recording the voltage induced across an external load resistance (Tzortzakis *et al* 1999, 2001c). Knowing the current density per ion ( $i = 3 \times 10^{-14}$  A cm $^{-2}$ ) and taking into account the volume occupied by a plasma filament, peak electron densities of  $10^{16}$ – $10^{17}$  cm $^{-3}$  have been reported in air at 800 nm. Another technique consists of resolving in time small local changes in the atmospheric refractive index by diffractometry (Tzortzakis *et al* 2000b). The principle here is to use a probe beam that crosses the filament path under a small angle. The far-field image of the probe forms fringe patterns that yield a direct measurement of the accumulated phase containing the plasma-induced defocusing effect. Let us also mention sonographic methods that take advantage of the sound signals along the plasma column (Hao *et al* 2005b, Hosseini *et al* 2004b, Yu *et al* 2003). This ‘acoustic’ diagnostics employs a microphone placed perpendicularly to the channel and records the sound signals by a digital oscilloscope. The sound emitted from a plasma string is a portion of the pressure modulation of an acoustic wave from which the absorbed optical energy and plasma density are deduced from the electric peak voltage at a given distance  $z$ . By doing so, the variations in the electron density can then be plotted along the propagation axis.

Plasma lengths attained from single  $\sim$  mJ femtosecond pulses currently remain of the order of the metre. The combination of twin pulses, launched collinearly in convergent geometry and separated from each other by a suitable time delay, can, however, double this length (Couairon *et al* 2003, Tzortzakis *et al* 2003). This process, called ‘concatenation’ of plasma filaments, relies on locking together the ionized channels generated by each individual pulse. By tuning their focal lenses ( $f_2 - f_1 \sim 1$  m) and their time separation ( $\simeq t_p$ ), the less powerful time slice ending the self-guiding of the first pulse coincides with the most powerful one of the second pulse starting a new plasma column (Bergé 2004).



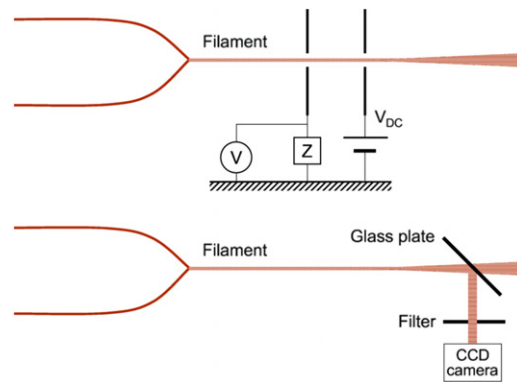


**Figure 27.** Schemes of experimental setups for (top) conductivity measurements and (bottom) CCD imaging for optical field measurements.

Experiments over a horizontal path provided more information about the length over which ionized plasma channels are formed (Méchain *et al* 2005a). The influence of an initial negative chirp enlarging the pulse duration from 0.2 to 9.6 ps, corresponding to 190 and 4  $P_{cr}$  at constant energy (190 mJ), respectively, was especially examined upon distances up to 2350 m. Whereas ionization is clearly observed over propagation scales  $<50$  m for short-pulse durations (0.2 ps), it becomes more and more sporadic for durations of above 3 ps and ceases for 9.6 ps pulses, i.e. at powers becoming close to critical. In this case, a few low-intensity ( $\sim 10^{12}$  W cm $^{-2}$ ), mm-waisted spots survive inside the photon bath, still capable of covering several hundred metres. The bundle does not convey enough power to trigger full ionization. Instead, the beam evolves in a regime along which GVD is able to take over MPI and sustain the beam in a confined state over distances of the order of the input Rayleigh length (Champeaux and Bergé 2005, Eisenmann *et al* 2007). When the initial power is too weak, broad beams may produce a few bright spots by modulational instability, but none of these is capable of developing extensive plasma sequences (see figure 6).

Several diagnostics exist for optical field measurements. The first consists of recording intensity profiles by a thick glass plate placed on the propagation axis at  $\sim 45^\circ$  angle (figure 27). The weak reflection from the glass is then imaged with a high aperture lens onto a linear charge coupled device (CCD) camera (Tzortzakis *et al* 2001a). Detection is performed out of the highest-intensity region close to the nonlinear focus, in order to leave the entrance window of the glass plate undamaged and keep up the reflected beam undistorted. Also, the high repetition rate of the laser source may not avoid multi-spot measurements. For this reason, Bernstein *et al* (2003) reported on single-shot measurements of self-focusing pulses that do not have the intensity required to produce ionization. Besides a CCD camera, a spectrometer and second-harmonic frequency-resolved optical gating (FROG) device allowed measurement of the spatial, spectral and temporal distributions of the pulse, respectively. The data, collected from an initially collimated Gaussian beam, showed spatial and temporal narrowing and spectral broadening at discrete energy levels preceding the ionization stage. They confirmed a critical power value for nonlinear compression effects of 11.5 GW for 800 nm pulses, i.e. about  $\sim 10$ –15 GW. Nowadays, several diagnostics such as SPIDER and crossed (X)FROG traces complete standard auto-correlation pictures and spectra to catch the spatio-temporal structure of a pulse in the  $(\omega, t)$  plane. To explore the filamentation stage along which intensities as high as  $5 \times 10^{13}$  W cm $^{-2}$  are attained, Gordon *et al* (2006) and Ting *et al* (2005a, 2005b) elaborated on a new method following which the filament is propagated into a helium chamber through

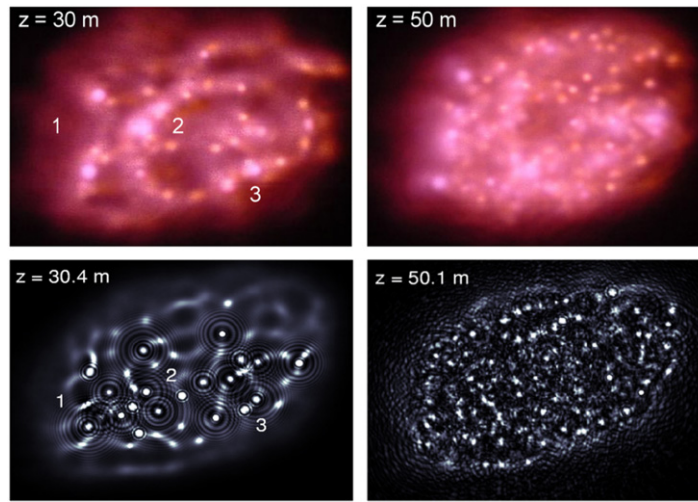


**Figure 28.** Filamentation patterns from the Teramobile beam with  $w_0 = 2.5$  cm, FWHM duration of 100 fs and input power equal to  $700 P_{\text{cr}}$  at different distances  $z$ . (top) Experiments; (bottom) numerical computations.

a nozzle that creates a sharp air–helium interface. Because helium has a lower Kerr index and a higher ionization potential than air, nonlinear focusing and plasma defocusing are arrested at the transition in the chamber. The filament then expands due to diffraction to larger sizes and lower intensities. A calibrated portion of energy can safely be collected and imaged either directly by a CCD array or through an imaging spectrometer.

**7.1.3. Multifilamentation.** Open-air terawatt laser facilities make it possible to observe optical focal spots formed by a myriad of filamentary cells for input powers containing several thousands of critical powers in air. The 2D reduced model (65a) using the experimental fluence as initial condition actually reproduces the evolution of the multifilamentation pattern over long scales, saving computational resources when one neglects the temporal dimension. As an example, figure 28 shows the overall envelope of the Teramobile bundle (see appendix D) launched in parallel geometry. The initial pulse contains 700 critical powers and its transverse profile is scanned at different propagation distances. Filaments rise from the initial beam defects, form a crown of dots growing from the diffraction ring and then excite clusters of cells. These clusters, some of which are identified by the labels (1), (2) and (3), are faithfully reproduced by the numerics. The modulational instability that seeds multiple filaments through the 2D reduced model gives a very reasonable qualitative picture of the relative placement of the individual intense light intensities within the broad beam. The filament number remains in the order of  $P_{\text{in}}/P_{\text{fil}}$ , where  $P_{\text{fil}} \simeq 3 - 5 P_{\text{cr}}$  is the power in one filament. At large distances, the primary brightest spots decay into secondary filaments by exchanging power through the energy reservoir formed by the background field (Bergé *et al* 2004).

When the focusing geometry is changed, the filamentation pattern becomes severely modified (Hao *et al* 2006). Figure 29 shows a longitudinal visualization of the filaments nucleated in a beam with  $760 P_{\text{cr}}$  and focal length  $f = 40$  m. The beam is directed towards an open cloud chamber scattering a weak-density cloud. After the focal point, only three strings of light emerge and cover about  $\sim 8$  m each, while the same beam should produce more than one hundred filaments in parallel geometry. Numerical computations for this configuration reveal

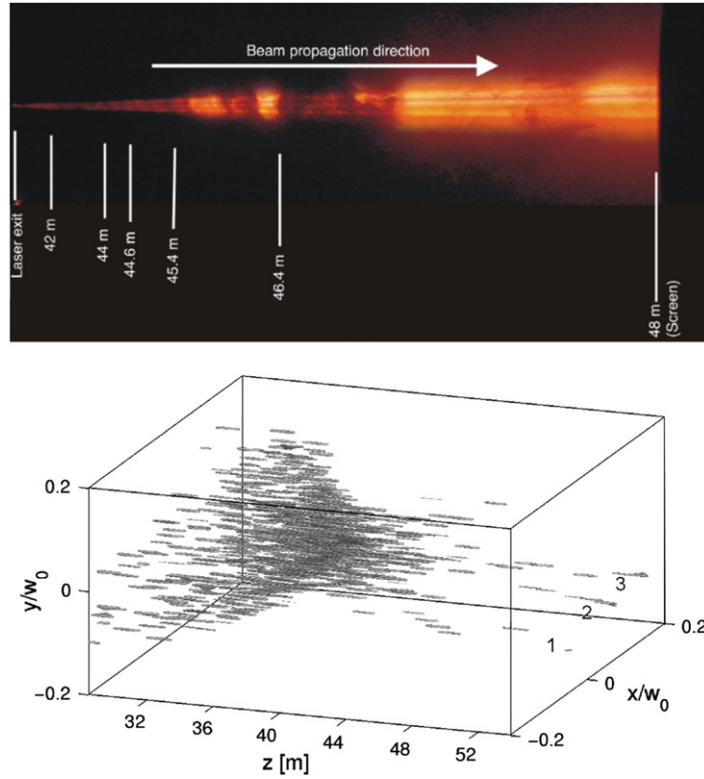


**Figure 29.** Teramobile fluence of a focused beam ( $f = 40$  m) with 760 critical powers, yielding three filamentary strings beyond the linear focal point: (top) experiment, (bottom) numerical computation from the 2D model (65a) and (65b).

that many filaments are created before the linear focus. These filaments then fuse near the focus into three strings of light acquiring a high directivity afterwards (Skupin *et al* 2004b). The same experimental setup (figure 30) put in evidence the robustness of femtosecond filaments through a multitude of  $1\text{ }\mu\text{m}$  large water droplets randomly distributed at various densities in the 10 m long cloud chamber. A filament is still transmitted through a cloud with an optical thickness as high as 3.2. For a cloud optical density of 1.2 or below, corresponding to cumulus or stratocumulus, the filamentation does not seem affected. Filaments remain visible at the exit of the fog even for a droplet concentration so high ( $8.6 \times 10^4\text{ cm}^{-3}$ ) that each filament hits on average 2000 droplets per propagation metre. The corresponding extinction coefficient is  $0.2\text{ m}^{-1}$ . Hence, filamentation can be transmitted through a fog over distances comparable with the visibility length. Energy losses due to random collisions imply an exponential decrease of power, which modifies the number and position of the filaments in the bundle (Méjean *et al* 2005). Such experiments, whose results are recalled in figure 31, permitted estimation of the power per filament to about  $5 P_{\text{cr}} \sim 15\text{ GW}$  in air (see bottom panel).

Pulse propagation in adverse weather becomes an important topic for LIDAR applications. In this context, Kandidov *et al* (1999) addressed the point of the nucleation of filaments in a turbulent atmosphere supporting statistical fluctuations of the refractive index. These fluctuations naturally arise as the medium becomes, e.g. locally heated. On the basis of a phase screen model, the cubic NLS equation including statistical variations of the linear optical



**Figure 30.** Open cloud chamber. The cloud spans over 10 m.

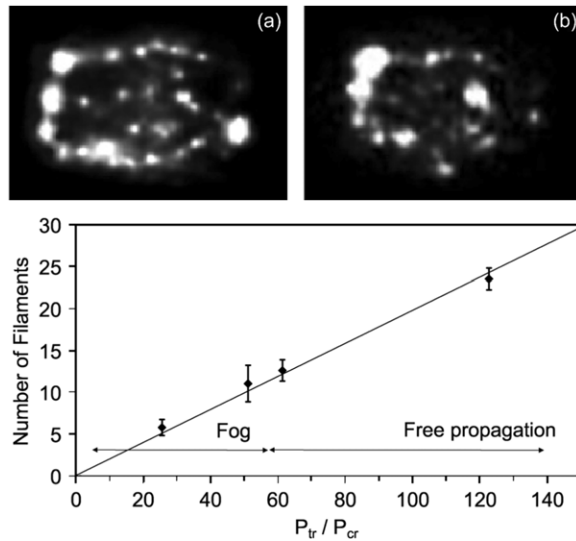


**Figure 31.** Modification of a filamentation pattern with  $\sim 120P_{cr}$  over 50 m: (a) in dry air and (b) after traversing a 10 m long tube of fog. The bottom panel reports the filament number versus the transmitted power over critical.

index (Kolmogorov turbulence) describes random paths for the nucleation and position of the nonlinear focus. This focus appears on the average shorter compared with unperturbed air and the beam centroid moves along a random path in the  $(x, y)$  plane. This induces a transverse deflection of the beam axis by several mm, which was later observed from experimental averaged data (Chin *et al* 2002b). Besides this beam wandering, femtosecond filaments keep their position stable relatively to the bundle in highly turbulent regions, as the index variation caused by the nonlinearity exceeds turbulent-induced refractive-index gradients by two orders of magnitude (Ackermann *et al* 2006b).

Furthermore, the influence of pressure variations on TW laser pulses was recently investigated. This issue is timely, as filaments propagating vertically over several km undergo

an exponential decrease of the local pressure,  $p(z) = p_0 e^{-z/L_a}$ , where  $L_a = 8$  km is the attenuation length for air density (Sprangle *et al* 2002). Pressure variations induce proportional changes in the GVD coefficient, the Kerr refractive index and molecule density available for ionization, as recalled by equation (76). At reduced pressure (0.7 atm), experiments performed at 3230 m altitude above sea level revealed farther filamentation onset and reduction of the filament number linked to the decrease of  $n_2(p)$  by 30% (Méchain *et al* 2005b). The filamentation process, especially the filament length, was shown to be qualitatively unaffected. Numerical simulations in this field specified that a single atmospheric filament does not indeed significantly change its self-channeling range and keeps an almost constant peak intensity. In contrast, the plasma level, the filament width (equations (70a) and (70b)) and the nonlinear focus (50) evolve with  $p$  and  $\sqrt{p}$ , respectively, due to the effective increase of  $P_{cr}(n_2)$ . Multifilamentation patterns have their onset distance governed by the maximum rate for modulation instability  $\gamma_{\max} \sim 1/n_2(p)I_0$  (see equation (68)). This length thus varies linearly with air pressure (Champeaux and Bergé 2006).

**7.1.4. White-light generation.** The white-light continuum generated in air by ultrashort laser pulses is essential in view of LIDAR applications, since it constitutes the light source used in multipollutant remote sensing. This white-light was characterized over recent years with progressively extending bandwidths. The supercontinuum was first characterized in the visible (Alfano and Shapiro 1970, Nishioka *et al* 1995). Kasparian *et al* (2000b) then investigated the infrared region. Two different terawatt CPA laser systems (A: 60 mJ energy, 35 fs minimal pulse duration, 25 mm FWHM beam diameter; B: 100–200 mJ, 100 fs minimal pulse duration, 35 mm FWHM diameters) produced spectra measured at a total distance of  $\sim 30$  m from the lens, as the laser beam was diffracting after 20 m of filament propagation. Illustrated in figure 32(a), the continuum band developed from laser system A is very broad, extending at least to  $4.5 \mu\text{m}$ . An almost exponential decay over 4 orders of magnitude up to  $2.5 \mu\text{m}$  is observed, followed by a slower decay of one order of magnitude only. As shown from the inset plotting results from laser system B, variations in the input energy make the spectral intensity change by only one decade in certain wavelength regions. The spectral shape of the different pulses remains, nevertheless, quite similar. Extension to the UV-visible domain down to 230 nm (figure 15) is not represented, as it was detected later. For comparison, figure 32(b) shows the numerically computed spectrum of a 2 mm waisted,  $4P_{cr} \sim 10$  GW, 127 fs pulse after a single femtosecond filament has been generated in air from the full FME model (43). The experimental and numerical spectral shapes are similar up to  $1.2 \mu\text{m}$ . Differences, however, occur at larger wavelengths, as space-time focusing and self-steepening shorten the red parts of the spectrum. Discrepancies at relative spectral intensities  $< 10^{-3}$  in the red wings may be attributed to differences in the input pulse, which can be chirped or not, as well as to uncertainties in the experimental measurements at such low intensity levels. Recovering quantitative agreements between experimental data and numerical simulations over long distances in air is still an open issue.

The similarity of white-light spectra emitted by TW laser pulses (experiments) and GW pulses suggests that the multifilamentation produces a spectrum analogous to that generated by a single filament. This conclusion is consistent with Chin *et al*'s (2002a) experimental observations about the coherence properties of femtosecond filaments. Observation of the interference pattern produced by two or more filaments allowed to predict that they emerge in phase from the background field and they possess the same phase relationship. This means that the laser spectrum around the central wavelength in the

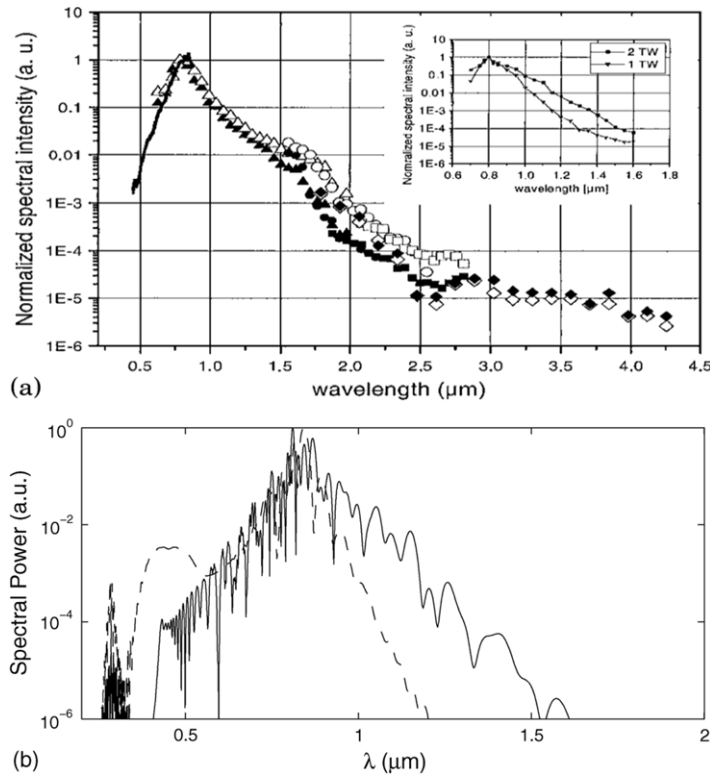


**Figure 32.** (a) Measured white-light spectrum by 2TW laser pulses (laser system A). Chirp settings correspond to 35 fs initial pulse duration without chirp (filled symbols) and 55 fs initial pulse duration with negative chirp (open symbols). Inset: spectrum measured from laser system B. The two curves have the same normalization factor. (b) Power spectrum integrated over a radius of 150  $\mu\text{m}$  around a single filament at  $z = 8\text{ m}$  (---) and  $z = 17\text{ m}$  (—), numerically computed from equation (43).

conditions of multiple filamentation is in principle identical to that developed by an isolated filament.

The previous property is important for LIDAR applications, because it suggests that the comprehension of the spectral dynamics of one filament is sufficient for understanding that of multifilamented beams. In addition to the wide spectral region covered by nonlinear femtosecond pulses, the strong enhancement of the backscattered photons in the filamentation regime makes ultrashort laser pulses quite promising tools for the remote identification of multipollutants in aerosols. Indeed, the supercontinuum emitted by a filament is enhanced in the backward direction (see equation (14)), i.e., towards the laser source. Measured at a small angle ( $\sim 3^\circ$ ) from the backward axis (located at  $180^\circ$  from the forward-scattering axis), the white-light emitted by femtosecond filaments was found to be greater by at least a factor 2 than the linear Rayleigh–Mie scattering (Yu *et al* 2001). It is expected to be even higher at exactly  $180^\circ$ , as the estimated ratio between the self-reflection factor and Rayleigh backscattering efficiency can approach 40. This nonlinear enhancement has been attributed to laser-induced longitudinal refractive index changes. It partly compensates the decrease in  $1/r^2$  ( $r$  being the observation distance) of linearly backscattered LIDAR signals. This explains why, as mentioned above (section 7.1.1), the white-light generated by femtosecond sources can be observed up to the stratosphere (Béjot *et al* 2007, Rodríguez *et al* 2004).



## 7.2. Remote sensing (LIDAR) applications

**7.2.1. Principle of LIDAR: towards ‘femtolidars’.** The LIDAR (light detection and ranging) technique (Fujii and Fukuchi 2005, Measures 1984, Theopold *et al* 2005, Wolf 2000) was demonstrated shortly after the advent of the first lasers. A laser pulse is emitted into the atmosphere. The backscattered light is collected on a telescope and detected as a function of time, with a typical resolution of 1–10 ns. This temporal window yields a high spatial resolution, since the flight time of the detected photons is directly proportional to the distance where they have been backscattered. Such a spatial resolution, combined with the possibility of sweeping the laser beam, provides two- and three-dimensional maps of measured atmospheric species. This is the main advantage of LIDAR over other measurement methods for atmospheric trace gases. One of the most popular LIDAR techniques is called DIAL (differential absorption LIDAR). It allows selective measurement of the concentration of gaseous pollutants by comparing the LIDAR signals at two nearby wavelengths, one being on an absorption line of the pollutant, and the other just beneath. However, this method is basically limited to pollutants that exhibit a narrow absorption line without interference from the absorption spectra of other atmospheric compounds. Moreover, the need to tune the laser wavelength on the absorption line forbids simultaneous identification of more than one pollutant within one acquisition.

Femtosecond LIDARs (or so-called ‘femtolidars’) overcome classical DIAL limitations. Exploiting the ‘femtosecond atmospheric lamp’ discovered in 1997 by Wöste *et al* (1997), high power ultrashort laser pulses can be shined vertically into the sky, where they generate white-light through the filamentation mechanism. The backscattered light, recorded with a telescope linked to a time-gated spectrometer, then provides a fascinating vector for atmospheric research over km ranges (Rairoux *et al* 2000, Rodriguez *et al* 2004). The spectral bandwidth developed by fs filaments is very broad, since it spans at least from 230 nm in the ultraviolet to 4.5  $\mu\text{m}$  in the mid-infrared (figure 33). On the spectrum, the absorption band of water between 1.8 and 2.5  $\mu\text{m}$  is clearly visible, showing the potential of white-light for optical remote sensing in the atmosphere. It also covers the absorption band of volatile organic compounds (VOCs) between 3 and 3.5  $\mu\text{m}$ . VOCs constitute a family of organic compounds with strongly overlapping absorption spectra, which prevents any measurement by classical DIAL techniques. In addition, the flat continuum spanning from the visible down to 230 nm (see figure 15) provides a promising light source for the measurement of trace gases that absorb in the blue or the UV, such as ozone, toluene, benzene,  $\text{SO}_2$  or nitrogen oxides. Recently, femtosecond laser-induced filaments were also applied for greenhouse gas methane ( $\text{CH}_4$ ) in air (Xu *et al* 2006a). Intense filaments dissociate pollutant molecules into small fragments, which emit characteristic fluorescence. This can be used to remotely measure the pollutant concentration at characteristic spectral lines.

Besides, multiparameter measurements are necessary to monitor the dynamics of atmospheric physico-chemistry or to remotely analyze a cocktail of species emitted during a chemical accident. They are also requested to characterize the nucleation and maturation of clouds. Such processes play an important role in atmospheric modeling, both on meteorological and climatological scales. In particular, the droplet growth and related density have a key influence on the forecast of both precipitations and earth albedo. Their characterization requires continuous measurements of the size distribution inside the clouds, with a temporal resolution of a few tens of minutes, compatible with the evaporation and growth time ranges. While airborne measurements are too expensive for routine monitoring, radiosounding does not provide the adequate repetition of probing. Therefore, optical techniques are promising, and they can be made optimal with fs laser pulses. As an example, a high resolution absorption



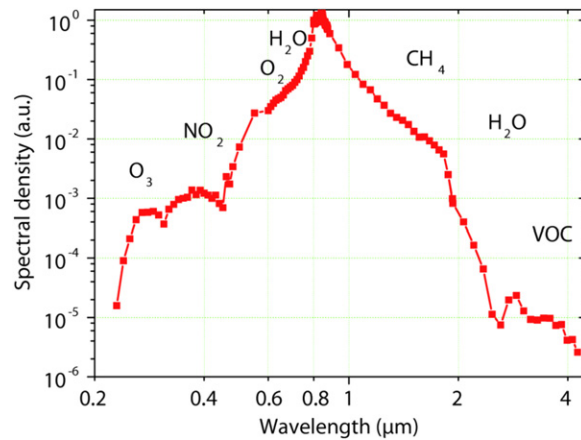


**Figure 33.** Spectrum of the white-light continuum assembled from five spectral regions. Main atmospheric absorption bands are marked above the curve.

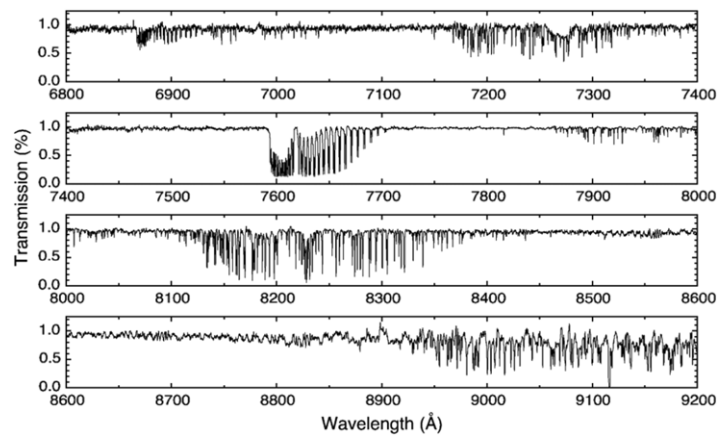


**Figure 34.** High resolution atmospheric absorption spectrum from an altitude of 4.5 km measured in a LIDAR configuration. The broad spectrum allowed to simultaneously measure the air temperature and humidity.

spectrum over a spectral interval larger than 200 nm is shown in figure 34, based on the white-light continuum, providing both the water vapor concentration and the temperature of air (Bourayou *et al* 2005, Kasparian *et al* 2003). Once combined, these two parameters supply the relative humidity, which is the relevant factor for atmospheric dynamics. Moreover, angular measurements of the multiple scattering yield the size distribution and concentration within the clouds, through an inversion of the laws of multiple Mie scattering based on a genetic algorithm. These measurements require the same laser source and two independent detectors. With fs LIDAR setups, they can be implemented simultaneously so as to yield a complete characterization of the cloud microphysics.

‘Femtolidars’ are not restricted to the white-light LIDAR. The high intensities carried in the filaments can generate nonlinear effects *in situ* on a target. Such nonlinear processes, which include ablation, ionization and multiphoton-excited fluorescence (M-PEF), constitute a supplementary information channel for remote sensing. An example of this technique has

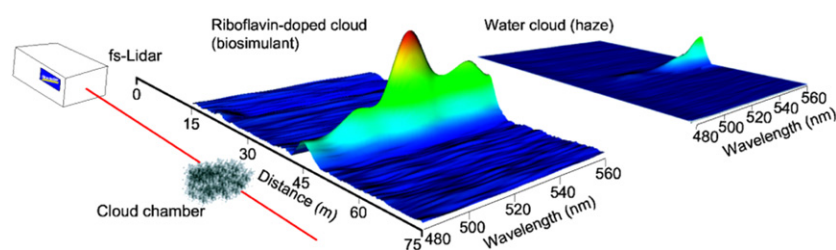


**Figure 35.** Remote detection and identification of bioaerosols. The femtosecond laser illuminates a plume of riboflavin containing microparticles 45 m away (left). The backward emitted 2-photon excited fluorescence (2-PEF), recorded as a function of distance and wavelength, exhibits the specific fluorescence signature of riboflavin for the bioaerosols (middle) but not for haze (right).

been provided by the remote detection and identification of biological aerosols through 2-PEF LIDAR (Méjean *et al* 2004). Here, the purpose was to detect and locate rapidly a suspect emission, to map the emitted cloud, and to identify potentially pathogenic agents among the multiple background atmospheric aerosols, including organic compounds such as soot or pollen. The 2-PEF allowed, for the first time, to remotely identify aerosols simulating biological agents in air by nonlinear LIDAR (figure 35). Moreover, collected signals based on N-PEF become more efficient than LIDAR signals based on 1-PEF for distances above a few kilometres. This is due to two effects: (i) the directional emission of the N-PEF from the aerosol particles minimizes the decrease of the collection efficiency with increasing distances (Boutou *et al* 2002), and (ii) the visible or near-infrared wavelengths used for exciting N-PEF, compared with the UV wavelength required for 1-PEF, experience less attenuation in the atmosphere because of the  $1/\lambda^4$  dependence of the Rayleigh scattering.

**7.2.2. Remote filament-induced breakdown spectroscopy.** The ability of the filaments to remotely deliver intensities as high as  $50 \text{ TW cm}^{-2}$  also opens the way to innovative exploration techniques, such as ‘remote filament-induced breakdown spectroscopy’ (R-FIBS) (Stelmaszczyk *et al* 2004). This consists of a combination of LIDAR and LIB spectroscopy (LIBS). LIBS (Cremers and Knight 2000, Cremers and Radziemski 2006) is a versatile tool allowing an elemental analysis of surfaces of materials such as metals (Angel *et al* 2001), plastics (Niessner 1994, Jong-Il *et al* 2002), minerals (Knight *et al* 2000, Sharma *et al* 2003, Wiens *et al* 2002), aerosols, biological materials (Kyuseok *et al* 1997) or liquids as well. It relies on the local ionization of the surface by a strongly focused pulsed laser, typically a Nd:YAG laser. The emission spectrum of the plasma generated at the surface allows a fast analysis, either qualitative or quantitative, with detection limits down to a few parts per million (ppm) for some elements. The use of subpicosecond laser pulses significantly enhances the reproducibility of the measurements, because the lower pulse energy limits the heating of the sample (Albert *et al* 2003, Angel *et al* 2001, Dou *et al* 2003, Rohwetter *et al* 2003). The use of broadband detection systems makes LIBS a flexible technique which requires neither preparation of the sample, nor *a priori* knowledge of the elements to be found. Applications such as the identification of highly radioactive nuclear waste or real-time monitoring of melted alloys in industrial processes need a remote analysis technique. LIBS, which is suitable for raw samples, is a good candidate in this regard, since it requires only a direct view of the sample. However, due to the limited size of the optical components, diffraction intrinsically limits the intensity that can be focused on a remote target. On the contrary, self-guided filaments can deliver much higher intensities than the ablation threshold of many species, at distances of

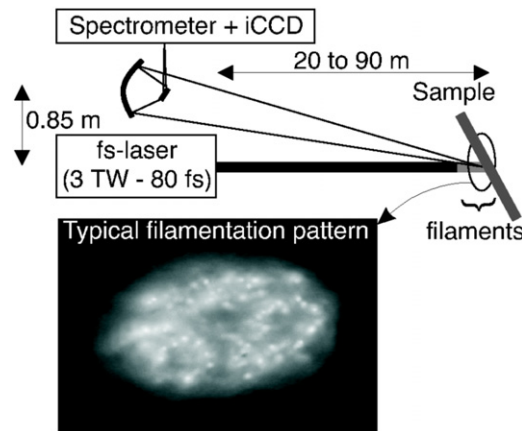


**Figure 36.** Principle of remote filament-induced breakdown spectroscopy (R-FIBS). Bottom: beam profile near the sample showing multifilamentation with typically 30 filaments across the beam (Stelmaszczyk *et al* 2004).

hundreds of metres or even kilometres. So, in R-FIBS techniques, the laser-generated filaments are launched on a remote target, and the light emitted by the excited plasma plume is collected through a detection setup comparable to a LIDAR-based one (figure 36). Although issued from 180 m distances (Stelmaszczyk *et al* 2004), the data suggest that measurements can be dimensioned up to the kilometre range (Rohwetter *et al* 2003). This technique is currently being developed for various applications, e.g. the monitoring of heritage (Tzortakis *et al* 2006) or bacteria (Baudalet *et al* 2006, Xu *et al* 2006b).

### 7.3. Towards a laser lightning rod

Besides remote sensing applications, ultrashort filaments may give access to the control of lightning strikes. Classical techniques to trigger lightning have employed rocket-pulled wires since the 1970s. However, the number of rockets available per storm is necessarily limited and rockets must be launched synchronously with the rise of the ambient electric field. Moreover, the wire falling down may pollute the measurement as well as the environment. Therefore, the idea emerged to apply lasers to control lightning by ionizing the ambient air along the beam and forming a conducting plasma ‘wire’. First attempts used nanosecond pulses (Ball 1974, Koopman and Wilkerson 1971, Miki *et al* 1993). They were unsuccessful, because such lasers could not produce continuously ionized plasma channels. More recently, this field was renewed by the advent of CPA lasers providing higher intensities in shorter pulses, therefore avoiding laser absorption by inverse bremsstrahlung. Encouraging results have been obtained using focused ultrashort laser pulses to trigger and guide high voltage discharges over several metres in the laboratory (Comtois *et al* 2000, Pépin *et al* 2001, Ting *et al* 2005a). Others have been obtained on smaller scales using UV ultrashort lasers (Rambo *et al* 2001). Since the filaments provide a conducting path over several metres or even longer, they are particularly suitable for the atmosphere. Spectacular experiments with the Teramobile laser installed in a high voltage facility showed that ultrashort filaments can guide discharges over up to 4.5 m (Ackermann *et al* 2006a). Instead of their usual erratic path, discharges are guided along the triggering laser beam (figure 37). Moreover, the breakdown voltage is typically

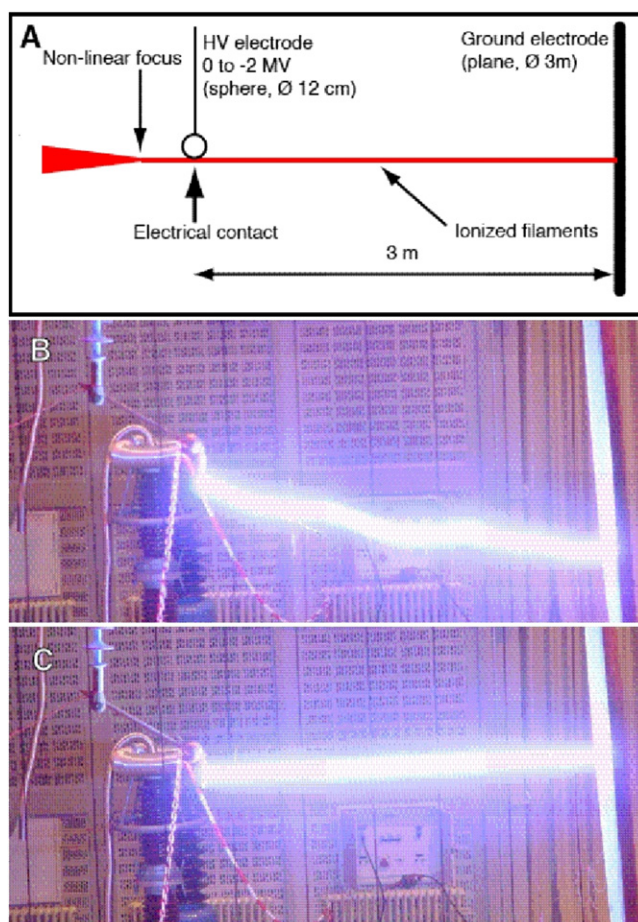


**Figure 37.** Laser control of high voltage discharges. (A) Experimental setup. (B) Free discharge over 3 m, without laser filaments. Note the erratic path. (C) Straight discharge guided along laser filaments (Kasparian *et al* 2003).

reduced by 30% (Rodriguez *et al* 2002). Partly guided discharges also occur in sphere-plane gaps, yielding valuable information about the mechanism of the initiation and propagation of laser-triggered streamers, with, e.g. plasma lifetimes of about  $1 \mu\text{s}$  (Ackermann *et al* 2006a). Furthermore, an artificial rain does not prevent the laser filaments from triggering such discharges (Ackermann *et al* 2004). Current research now focuses on the possibility of extending the plasma lifetime, in order to increase the guiding length and improve scalability to the atmosphere. This approach relies on re-heating and photodetaching electrons of the plasma channel by subsequent pulses, either in the nanosecond (Rambo *et al* 2001) or in the femtosecond regime (Hao *et al* 2005a). Although high laser powers are usually believed to efficiently detach electrons from  $\text{O}_2^-$  ions in the plasma, it was recently demonstrated that a subsequent Nd : YAG laser pulse of moderate energy (sub-Joule) at 532 nm efficiently supports the triggering of discharges by an infrared, femtosecond laser (Méjean *et al* 2006a). This effect was interpreted as resulting from a positive retroaction loop where Joule heating of the plasma channel enhances photodetachment, while the resulting higher electron density boosts in turn the Joule effect.

## 8. Outlook

Femtosecond lasers opened up beam parameter ranges from which universal, robust ultrashort filamentary structures conveying high intensities can propagate over long distances in a rich variety of transparent media. These ‘femtosecond filaments’ are characterized by sizes of a few tens up to hundreds of microns and can reach ultrashort FWHM durations down to the optical cycle limit. They design new objects, which can be exploited for delivering few-cycle pulses at very high power levels in the future. Ionization processes do not break this property. They even amplify it by cutting the back time slices of the pulse. An accurate control of plasma generation should push the frontiers in nonlinear optics and allow for a precise monitoring of high-order harmonics. The basic scenario of a dynamical balance between Kerr focusing and plasma defocusing explains the existence and the long life of femtosecond filaments in most of the propagation configurations. This scenario must, however, be revised at visible wavelengths in dense materials, in which chromatic dispersion and nonlinear absorption drive the self-guiding mechanism through an important conical emission managed by X-shaped waveforms in normally dispersive regimes. This aspect requires more investigations. Also, propagation regimes of anomalous dispersion, which promote temporal compression and may further improve self-compression techniques, should be probed.

In recent years, impressive progress has been made in the understanding of the nonlinear propagation of high power laser pulses over long distances in the atmosphere. For broad beams, multiple filamentation becomes more and more controllable by the use of deformable mirrors and genetic algorithms. Besides classical techniques of linear focusing and phase chirping, this will soon enable experimentalists to optimize the propagation range of very powerful pulses. Filaments can therefore be used to remotely deliver high intensities generating *in situ* nonlinear effects. The spectrum of the white-light continuum is much broader than that expected a few years ago, especially in the ultraviolet where the mixing between the fundamental and third harmonic wavelengths together with the spectral amplification caused by pulse steepening gives rise to a spectral plateau extending down to 230 nm. Progress in these areas opens the way to applications such as remote sensing of gaseous pollutants and aerosols by LIDAR, LIBS analysis of solid samples or the control of high voltage electric discharges and lightning strikes. Due to its mobility, the Teramobile allowed to demonstrate the feasibility of many of these techniques. These applications will probably be pushed forward in the future by technological improvements involving more compact systems, diode pumping, as well as spatial and temporal pulse shaping. Novel active media, such as ytterbium doping or optical parametric chirped-pulse amplifiers, also open the way to new spectral regions, especially the infrared. This spectral domain, where eye safety constraints are easier to fulfill, is nearer the absorption region of many pollutants, such as volatile organic compounds. These more flexible systems will be easier to operate, allowing routine uses for future industrial or atmospheric applications.

## Acknowledgments

The Teramobile project is funded by the Centre National de la Recherche Scientifique (CNRS, France) and the Deutsche Forschungsgemeinschaft (DFG, Germany), with contributions by the French and German ministries of Foreign Affairs and the Agence Nationale de la Recherche (ANR, France). The authors gratefully acknowledge its team members, formed by the groups of L. Wöste at the Freie Universität Berlin, R. Sauerbrey at the Friedrich Schiller Universität

Jena, A Mysyrowicz at Laboratory for Applied Optics, Palaiseau (France) and the LASIM team led by J-P Wolf.

## Appendix A. List of abbreviations

Abbreviations	Meaning
4 WM	four-wave mixing
ADK	Ammosov, Delone, Krainov
CCD	charge coupled device
CE	conical emission
CPA	chirped-pulse amplification
DIAL	differential absorption lidar
EMP	electromagnetic pulse
FME	forward Maxwell equation
FWHM	full width at half maximum
GVD	group-velocity dispersion
HHG	high harmonic generation
IR, UV	infrared, ultraviolet
LIB(S)	laser-induced breakdown (spectroscopy)
LIDAR	light detection and ranging
M-PEF	multiphoton-excited fluorescence
MI	modulational instability
MPA	multiphoton absorption
MPI	multiphoton ionization
NEE	nonlinear envelope equation
NLS	nonlinear Schrödinger (equation)
PPT	Perelomov, Popov, Terent'ev
R-FIBS	remote filament-induced breakdown spectroscopy
SPIDER	spectral phase interferometry for direct electric-field reconstruction
SPM	self-phase modulation
TH	third harmonic
UPPE	unidirectional pulse propagation equation
VOC	volatile organic compound
(X)FROG	(crossed) frequency resolved optical gating
XPM	cross-phase modulation
XUV	extreme ultraviolet

## Appendix B. Ionization rates for atoms and molecules

This appendix details different photo-ionization theories for gases and dense materials.

### Appendix B.1. Ionization in gases

*Appendix B.1.1. Keldysh theory.* To model the generation of free electrons by an intense light field interacting with a gas, Keldysh first derived a photo-ionization rate for atomic systems ([Keldysh 1965](#)). Keldysh theory is limited to hydrogenoid atoms in their fundamental

electronic state and does not consider the Coulomb interaction between the leaving electron and the residual ion. The ionization rate of an atom irradiated by a laser field  $\vec{E}(t) = \vec{E}_p \cos(\omega t)$  is evaluated by

$$W = \frac{q_e^2}{\hbar^2} \lim_{t \rightarrow \infty} \int \frac{d\vec{p}}{(2\pi\hbar)^3} \frac{d}{dt} \left| \int_0^t dt' \cos(\omega t') \langle \Psi_{\vec{p}}(\vec{r}, t') | \vec{r} \cdot \vec{E}_p | \Psi_g(\vec{r}, t') \rangle \right|^2, \quad (\text{B1})$$

where  $q_e$  is the electron charge and the ground state of the hydrogenlike atom, characterized by the energy  $E_g = -U_i$  (ionization potential), is

$$\Psi_g(\vec{r}, t) = \frac{1}{\sqrt{\pi a^3}} e^{-\frac{r}{a}} e^{-\frac{i}{\hbar} E_g t}. \quad (\text{B2})$$

Here,  $a = a_B/Z$  includes the Bohr radius  $a_B$  of hydrogen. The continuum electronic states are described with the Volkov functions

$$\Psi_{\vec{p}}(\vec{r}, t) = e^{\frac{i}{\hbar} [(\vec{p} + q_e \vec{A}(t)) \cdot \vec{r} - \frac{1}{2m_e} \int_0^t dt' [\vec{p} + q_e \vec{A}(t')]^2]}, \quad (\text{B3})$$

where  $\vec{A}(t)$  is the vector potential of the laser field. Insertion of (B2) and (B3) into equation (B1) and integration over the spatial coordinates result in the expression

$$W = \frac{2}{\hbar^2} \lim_{t \rightarrow \infty} \text{Re} \left[ \int \frac{d\vec{p}}{(2\pi\hbar)^3} \times \int_0^t dt' \cos(\omega t) \cos(\omega t') L(\vec{p}, t') L^*(\vec{p}, t) \right], \quad (\text{B4})$$

where  $*$  means complex conjugate and

$$L(\vec{p}, t) = V_0 \left[ \vec{p} - \frac{q_e}{\omega} \vec{E}_p \sin(\omega t) \right] e^{\frac{i}{\hbar} \left\{ U_i t + \frac{1}{2m_e} \int_0^t dt' \left[ \vec{p} - \frac{q_e}{\omega} \vec{E}_p \sin(\omega t') \right]^2 \right\}}, \quad (\text{B5a})$$

$$V_0(\vec{p}) = -i8q_e \sqrt{\pi a^3} \hbar \vec{E}_p \cdot \vec{\nabla}_{\vec{p}} \left[ \frac{1}{\left( 1 + \frac{a^2 p^2}{\hbar^2} \right)^2} \right]. \quad (\text{B5b})$$

The function  $L(\vec{p}, t)$  is periodic, with period equal to  $T = 2\pi/\omega$ . It can then be decomposed into Fourier series. Plugging this series into equation (B4) leads to

$$W = \frac{2\pi}{\hbar} \int \frac{d\vec{p}}{(2\pi\hbar)^3} |L(\vec{p})|^2 \sum_{n=-\infty}^{+\infty} \delta \left( U_i + \frac{p^2}{2m_e} + \frac{q_e^2 E_p^2}{4m_e \omega^2} - n\hbar\omega \right), \quad (\text{B6})$$

with

$$L(\vec{p}) = 16iq_e \frac{\sqrt{\pi a^3}}{\hbar\pi} U_i^3 \int_{-1}^1 du \frac{\vec{E}_p \cdot \left( \vec{p} - \frac{q_e}{\omega} \vec{E}_p u \right)}{\left[ U_i + \frac{1}{2m_e} \left( \vec{p} - \frac{q_e}{\omega} \vec{E}_p u \right)^2 \right]^3} \times e^{\frac{i}{\hbar\omega} \int_0^u \frac{dv}{\sqrt{1-v^2}} \left[ U_i + \frac{1}{2m_e} \left( \vec{p} - \frac{q_e}{\omega} \vec{E}_p v \right)^2 \right]}. \quad (\text{B7})$$

Assuming that the electron leaves the atom with a small kinetic energy ( $\frac{p^2}{2m_e} \ll U_i$ ), the poles in the denominator of  $L(\vec{p})$  are written as

$$u_s^{\pm} = i\gamma \left[ \pm 1 + i \frac{p \cos(\theta)}{\sqrt{2m_e U_i}} \pm p^2 \frac{\sin^2(\theta)}{2m_e U_i} \right], \quad (\text{B8})$$

where  $\theta$  is the angle between the impulsions vector  $\vec{p}$  and the electric field  $\vec{E}(t)$ .  $\gamma = \omega \sqrt{2m_e U_i} / (|q_e| E_p)$  is the adiabaticity *Keldysh parameter*. It involves the ratio of the



ionization potential over the ponderomotive energy  $U_p \equiv q_e^2 E_p^2 / 4m_e \omega^2$ . By means of the saddle point method and the residue theorem, equation (B7) is next integrated to yield

$$W = 4\sqrt{2}\omega\sqrt{\frac{U_i}{\hbar\omega}} \left[ \frac{\gamma}{\sqrt{1+\gamma^2}} \right]^{\frac{3}{2}} e^{-\frac{2\tilde{U}_i}{\hbar\omega} \left[ \sinh^{-1}(\gamma) - \frac{\gamma\sqrt{1+\gamma^2}}{1+2\gamma^2} \right]} S\left(\gamma, \frac{\tilde{U}_i}{\hbar\omega}\right), \quad (\text{B9})$$

where  $\tilde{U}_i \equiv U_i + U_p$  and  $S(\gamma, x)$  is defined by

$$S(\gamma, x) = \sum_{n=0}^{+\infty} e^{-2 \left[ \sinh^{-1}(\gamma) - \frac{\gamma}{\sqrt{1+\gamma^2}} \right] ((x+1)-x+n)} \int_0^{\sqrt{\frac{2\gamma}{\sqrt{1+\gamma^2}} ((x+1)-x+n)}} e^{y^2 - \frac{2\gamma}{\sqrt{1+\gamma^2}} ((x+1)-x+n)} dy. \quad (\text{B10})$$

To take electron-ion correlation into account, Keldysh eventually multiplies the ionization rate by the factor  $(U_i/\hbar\omega)\gamma/\sqrt{1+\gamma^2}$ . Expressed in atomic units (a.u.)  $m_e = |q_e| = \hbar = a_B = 1$  (Bransden and Joachain 2003), the resulting ionization rate expresses

$$W = 2\sqrt{2} \left( \frac{2E_0}{E_p\sqrt{1+\gamma^2}} \right)^{\frac{1}{2}} e^{-2\nu \left[ \sinh^{-1}(\gamma) - \frac{\gamma\sqrt{1+\gamma^2}}{1+2\gamma^2} \right]} U_i \frac{\gamma^2}{1+\gamma^2} \sum_{\kappa \geq \nu_0}^{+\infty} e^{-\alpha(\kappa-\nu)} \Phi_0(\sqrt{\beta(\kappa-\nu)}), \quad (\text{B11})$$

where  $E_0 = (2U_i)^{3/2}$ ,  $\gamma = \omega\sqrt{2U_i}/E_p$ ,  $\nu = \tilde{U}_i/[\hbar\omega]_{\text{a.u.}}$ ,  $\beta = 2\gamma/\sqrt{1+\gamma^2}$ ,  $\alpha = 2[\sinh^{-1}(\gamma) - \gamma/\sqrt{1+\gamma^2}]$ ,  $\nu_0 = \langle \nu + 1 \rangle$  and  $\Phi_m(x) = e^{-x^2} \int_0^x (x^2 - y^2)^{|m|} e^{y^2} dy$ . Equation (B11) differs from the original Keldysh formulation by a factor of 4, originating from a corrected version of the residue theorem.

This theory was the first one able to describe atom ionization by an alternating field in the low intensity regime ( $\gamma \gg 1$ ) as well as in the high intensity regime ( $\gamma \ll 1$ ). The former regime refers to multiphoton ionization (MPI), through which the electron is freed as the atom absorbs  $K = \langle U_i/(\hbar\omega) + 1 \rangle$  photons. The latter one corresponds to the tunnel regime, for which the electron leaves the ion by passing through the Coulomb barrier. In MPI regime, the ionization rate is obtained by taking the limit  $\gamma \rightarrow +\infty$  in equation (B11), which reduces to

$$W = \sigma^{(K)} \times I^K, \quad (\text{B12})$$

where  $I$  is the laser intensity and  $\sigma^{(K)}$  is the photo-ionization cross-section

$$\sigma^{(K)} = 4\sqrt{2}\omega \left( \frac{U_i}{[\hbar\omega]_{\text{a.u.}}} \right)^{2K+3/2} \frac{e^{2K-U_i/[\hbar\omega]_{\text{a.u.}}}}{E_0^{2K}} \Phi_0 \left( \sqrt{2K - \frac{2U_i}{[\hbar\omega]_{\text{a.u.}}}} \right). \quad (\text{B13})$$

Expressed in  $\text{s}^{-1} \text{cm}^2/\text{W}^K$ , the above ‘cross-section’ parameter must be converted as  $\sigma^{(K)} \rightarrow \sigma_K \equiv \sigma^{(K)}[\text{a.u.}]/[2.42 \times 10^{-17} \times (3.51 \times 10^{16})^K]$ .

*Appendix B.1.2. The PPT theory.* Later, Perelomov *et al* (1966, 1967) developed a more accurate model. First, they included the Coulomb interaction between the ion and the electron, when the latter leaves the atomic core. Second, they considered any atomic bound states as initial. The resulting rate is then

$$W = \frac{4\sqrt{2}}{\pi} |C_{n^*, l^*}|^2 \left( \frac{2E_0}{E_p\sqrt{1+\gamma^2}} \right)^{2n^* - \frac{3}{2} - |m|} \frac{f(l, m)}{|m|!} e^{-2\nu \left[ \sinh^{-1}(\gamma) - \frac{\gamma\sqrt{1+\gamma^2}}{1+2\gamma^2} \right]} \times U_i \frac{\gamma^2}{1+\gamma^2} \sum_{\kappa \geq \nu_0}^{+\infty} e^{-\alpha(\kappa-\nu)} \Phi_m(\sqrt{\beta(\kappa-\nu)}), \quad (\text{B14})$$

where  $n^* = Z/\sqrt{2U_i}$  is the effective quantum number,  $Z$  is the residual ion charge,  $l^* = n^* - 1$  and  $n, l, m$  are the principal quantum number, the orbital momentum and the magnetic quantum number, respectively. The factors  $|C_{n^*,l^*}|$  and  $f(l, m)$  are

$$|C_{n^*,l^*}|^2 = \frac{2^{2n^*}}{n^* \Gamma(n^* + l^* + 1) \Gamma(n^* - l^*)}, \quad (\text{B15a})$$

$$f(l, m) = \frac{(2l+1)(l+|m|)!}{2^{|m|} |m|! (l-|m|)!}. \quad (\text{B15b})$$

Even if equation (B14) is usually presented as the PPT formula, the coefficients  $|C_{n^*,l^*}|$  are in fact extracted from the tunneling theory derived by Ammosov *et al* (1986). Differences between PPT and ADK coefficients essentially lie in the fact that ADK theory employs electron wavefunctions in a Coulomb potential (Volkov states), which are connected by continuity with the continuum states at large distances ( $r \gg 1/\sqrt{2U_i}$ ).

*Appendix B.1.3. The ADK molecular theory.* The PPT rate (equation (B14)) holds to describe photo-ionization of atoms. It can lead to some discrepancy when it is applied to molecular systems, because the coefficients  $|C_{n^*,l^*}|$ , originally evaluated from atomic wavefunctions, cannot reproduce molecular peculiarities, such as, for example, the suppression of ionization observed from the molecule  $\text{O}_2$  (DeWitt *et al* 2001). To overcome such limitations, we may extend the molecular tunneling theory by Tong *et al* (2002) by plugging molecular coefficients into the tunnel limit of the PPT formula and prolonging the latter to low intensity MPI regimes analytically. By doing so, equation (B14) is able to describe molecule ionization after the substitution

$$|C_{n^*,l^*}|^2 f(l, m) \rightarrow \left[ \sum_l \frac{C_l}{(2U_i)^{(n^*/2)+(1/4)}} \sqrt{\frac{(2l+1)(l+|m|)!}{2^{|m|} |m|! (l-|m|)!}} \right]^2, \quad (\text{B16})$$

where the coefficients  $C_l$  have been established for different molecules. For dioxygen,  $C_2 = 0.683$  and  $C_4 = 0.033$  while  $C_1=C_3=0$ , and  $m = 1$  (Tong *et al* 2002).

### Appendix B.2. Ionization in dense media

Plasma generation in dense media is described with the rate for crystals developed by Keldysh (1965). Its analytical evaluation is identical to that applying to atoms, except that the initial states are now modeled by Bloch wave functions. Following a similar procedure, the ionization rate for crystals with energy gap  $E_g$  irradiated by an electromagnetic field  $E_p \cos(\omega t)$  is

$$W = \frac{2\omega}{9\pi} \left( \frac{\sqrt{1+\gamma^2} m^* \omega}{\gamma \hbar} \right)^{\frac{3}{2}} Q \left( \gamma, \frac{\tilde{\Delta}}{\hbar \omega} \right) e^{-\pi \left( \frac{\tilde{\Delta}}{\hbar \omega} + 1 \right) \times \left[ \frac{\tilde{\kappa} \left( \frac{\gamma^2}{1+\gamma^2} \right) - \tilde{\varepsilon} \left( \frac{\gamma^2}{1+\gamma^2} \right)}{\tilde{\varepsilon} \left( \frac{1}{1+\gamma^2} \right)} \right]} \quad (\text{B17})$$

with  $\gamma = \omega \sqrt{m^* E_g} / (|q_e| E_p)$ ,  $m^{*-1} = m_e^{-1} + m_h^{-1}$ ,

$$\tilde{E}_g = \frac{2}{\pi} E_g \frac{\sqrt{1+\gamma^2}}{\gamma} \tilde{\mathcal{E}} \left( \frac{1}{1+\gamma^2} \right), \quad (\text{B18a})$$

$$Q(\gamma, x) = \sqrt{\frac{\pi}{2\tilde{\mathcal{K}} \left( \frac{1}{1+\gamma^2} \right)}} \times \sum_{n=0}^{+\infty} e^{-\pi n \left[ \frac{\tilde{\mathcal{K}} \left( \frac{\gamma^2}{1+\gamma^2} \right) - \tilde{\mathcal{E}} \left( \frac{\gamma^2}{1+\gamma^2} \right)}{\tilde{\mathcal{E}} \left( \frac{1}{1+\gamma^2} \right)} \right]} \times \Phi_0 \left( \sqrt{\frac{\pi^2}{4} \frac{2\langle x+1 \rangle - 2x + n}{\tilde{\mathcal{K}} \left( \frac{1}{1+\gamma^2} \right) \tilde{\mathcal{E}} \left( \frac{1}{1+\gamma^2} \right)}} \right). \quad (\text{B18b})$$

Here, the functions  $\tilde{\mathcal{K}}(x) \equiv \int_0^{\pi/2} (1 - x \sin^2 \theta)^{-1/2} d\theta$  and  $\tilde{\mathcal{E}}(x) \equiv \int_0^{\pi/2} (1 - x \sin^2 \theta)^{1/2} d\theta$  are the complete elliptic integrals of the first and second kind (Abramovitz and Stegun 1972) and  $m^*$  is the reduced mass for the electron/hole pair. The above equation corrects a slip of pen in the original Keldysh's formula. Whereas  $W$  for gas (equation (B11)) is expressed per time unit,  $W$  for condensed media (equation (B17)) is expressed per time unit and per cubic metre. This ionization rate reduces at low intensities to its multiphoton limit ( $\gamma \rightarrow +\infty$ ) taking the form

$$W = \sigma^{(K)} \times I^K, \quad (\text{B19})$$

where

$$\sigma^{(K)} = \frac{2\omega}{9\pi} \left( \frac{m^* \omega}{\hbar} \right)^{\frac{3}{2}} \Phi_0 \left( \sqrt{2 \left( K - \frac{E_g}{\hbar \omega} \right)} \right) e^{2K} \left( \frac{q_e^2}{8m^* \omega^2 E_g \epsilon_0 c n_0} \right)^K. \quad (\text{B20})$$

### Appendix C. Atomic dipole for high harmonic generation

The nonlinear polarization vector  $\vec{P}_{\text{NL}}(\vec{r}, t)$  used to describe HHG in gases is expressed as

$$\vec{P}_{\text{NL}}(\vec{r}, t) = \rho_{\text{nt}} \vec{d}(\vec{r}, t), \quad (\text{C1})$$

where  $\vec{d}(\vec{r}, t)$  is the time-dependent atomic dipole calculated by Lewenstein *et al* (1994). For a single electron interacting with a linearly polarized laser field  $\vec{E}(t) = E_p \hat{x} \cos(\omega t)$ , the atomic dipole is defined by

$$\vec{d}(\vec{r}, t) = q_e \langle \psi(\vec{r}, t) | \vec{r} | \psi(\vec{r}, t) \rangle. \quad (\text{C2})$$

Solving the time-dependent Schrödinger equation,  $\psi(\vec{r}, t)$  denotes the electronic wavefunction

$$|\psi(\vec{r}, t)\rangle = e^{i \frac{U_i t}{\hbar}} \times \left[ |0\rangle + \int d^3 v b(\vec{v}, t) |v\rangle \right], \quad (\text{C3})$$

where  $U_i$  is the ionization potential of the atom,  $|0\rangle$  is the ground state and  $b(\vec{v}, t)$  is the amplitude of the continuum states  $|v\rangle$ , respectively. In equation (C3), several assumptions have been made, which limits the validity domain of this theory.

- All excited electronic states are ignored, reducing the model to harmonic orders  $2K + 1 \geq \frac{U_i}{\hbar \omega}$ .
- The depletion of the ground state is neglected such that the ground state amplitude is equal to 1.

- Electrons in the continuum are treated as free particles moving in an oscillating laser field, with no Coulomb potential. This assumption is valid when the ponderomotive energy  $U_p$  is higher than  $U_i$ .

Inserting (C3) into equation (C2), we obtain

$$\begin{aligned} \vec{d}(t) = & i \frac{q_e^2 E_p \hat{x}}{\hbar \omega} \int_0^{\omega t} d(\omega t') \cos(\omega t') \int d^3 p \, d_x^*[\vec{p} + q_e \vec{A}(t)] \\ & \times e^{-i \frac{S(\vec{p}, t, t')}{\hbar \omega}} \times d_x[\vec{p} + q_e \vec{A}(t')] + \text{c.c.}, \end{aligned} \quad (\text{C4})$$

where  $\vec{d}(\vec{p} + q_e \vec{A}(t))$  is the field-free dipole transition matrix element between the ground state and the continuum state characterized by the momentum  $\vec{v} = \vec{p} + q_e \vec{A}(t)$ . Here,  $\vec{p}$  is the canonical momentum and  $\vec{A}(t)$  is the vector potential of the laser field [ $\vec{E}(t) = -\partial \vec{A}(t)/\partial t$ ]. Its formulation for transition from state  $|1s\rangle$  is

$$\vec{d}(\vec{p}) = -i\hbar \frac{2^{7/2}}{\pi} (2m_e U_i)^{5/4} \frac{\vec{p}}{(\vec{p}^2 + 2m_e U_i)^3}, \quad (\text{C5})$$

where  $m_e$  is the electron mass.  $S(\vec{p}, t, t')$  is the quasi-classical action describing the motion of an electron freely moving in the laser field with constant momentum  $\vec{p}$  as

$$S(\vec{p}, t, t') = \int_{\omega t'}^{\omega t} \left\{ U_i + \frac{[\vec{p} + q_e \vec{A}(t'')]^2}{2m_e} \right\} d(\omega t''). \quad (\text{C6})$$

The harmonic amplitude  $\vec{d}_{2K+1}$  follows from Fourier transforming the time-dependent dipole moment  $\vec{d}(t)$

$$\vec{d}_{2K+1} = \frac{1}{T} \int_0^T \vec{d}(t) e^{i(2K+1)\omega t} dt. \quad (\text{C7})$$

For isotropic media, only odd harmonics are produced. The dominant contributions to  $\vec{d}_{2K+1}$  come from the stationary points of the Legendre-transformed quasi-classical action, for which the derivatives of  $S(\vec{p}, t, t') - (2K+1)\hbar\omega \times \omega t$  with respect to  $\vec{p}$ ,  $t$  and  $t'$  vanish. Introducing the returning time  $\tau = t - t'$ , the saddle point equations read

$$\vec{\nabla}_{\vec{p}} S = \vec{p}_{\text{st}} \omega \tau + q_e \int_{\omega(t-\tau)}^{\omega t} \vec{A}(t'') d(\omega t'') = 0 \quad (\text{C8a})$$

$$\frac{\partial S}{\partial(\omega \tau)} = U_i + \frac{[\vec{p}_{\text{st}} + q_e \vec{A}(t - \tau)]^2}{2m_e} = 0 \quad (\text{C8b})$$

$$\frac{\partial S}{\partial(\omega t)} = \frac{[\vec{p}_{\text{st}} + q_e \vec{A}(t)]^2}{2m_e} - \frac{[\vec{p}_{\text{st}} + q_e \vec{A}(t - \tau)]^2}{2m_e} = (2K+1)\hbar\omega. \quad (\text{C8c})$$

Equation (C8a) reduces to  $\vec{\nabla}_{\vec{p}} S(\vec{p}, t, t') = \vec{x}(t) - \vec{x}(t') = \vec{0}$ , where  $\vec{x}(t) \equiv \int_0^t \vec{v}(t') dt'$ . This relation imposes that the electron trajectories return at time  $t$  to the same point they left at the time  $t'$  of ionization. Using equations (C8b) and (C8c) together with the Fourier expansion of  $[(\vec{p}_{\text{st}} + q_e \vec{A}(t - \tau))^2 / (m_e \hbar \omega) + 2U_i / (\hbar \omega)]^{-3}$  yields the final expression for the Fourier

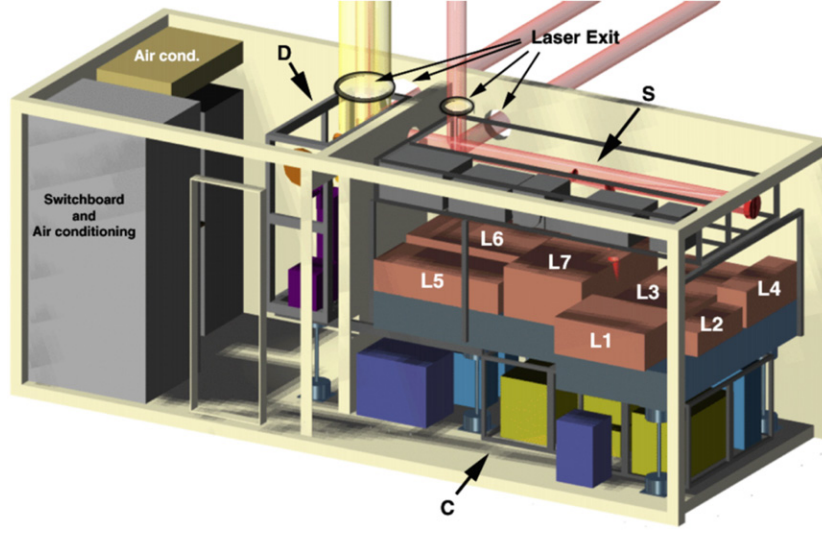


**Figure 38.** Three-dimensional view of the Teramobile. (L): Laser system: Ti : Sa oscillator and its Nd : YAG pump laser (L1), stretcher (L2), regenerative amplifier, multipass preamplifier (L3) and their Nd : YAG pump laser (L4); Multipass main amplifier (L5) pumped by two Nd : YAG units (L6); Compressor (L7). (S) Beam expanding system; (C) power supplies; (D) LIDAR detection system.

component of the dipole, i.e.

$$\begin{aligned} \vec{d}_{2K+1} = & -i \frac{q_e \left( \frac{U_p}{\hbar\omega} \right)^{\frac{3}{2}} \frac{32\hbar}{\pi^2} \left( \frac{2U_i}{\hbar\omega} \right)^{\frac{5}{2}}}{(2K+1)^3 \sqrt{m_e \hbar\omega}} \sum_{M=-\infty}^{\infty} \int_0^{+\infty} d\Phi \left[ \frac{\pi}{\epsilon + i\frac{\Phi}{2}} \right]^{\frac{3}{2}} b_M(\Phi) e^{-i\frac{F_K(\Phi)}{\hbar\omega}} i^{K-M} \\ & \times \left\{ -B(\Phi) J_{K-M+2} \left( \frac{U_p C(\Phi)}{\hbar\omega} \right) - i B(\Phi) e^{i\Phi} J_{K-M-1} \left( \frac{U_p C(\Phi)}{\hbar\omega} \right) \right. \\ & + i [B(\Phi) e^{i\Phi} + D(\Phi)] J_{K-M+1} \left( \frac{U_p C(\Phi)}{\hbar\omega} \right) \\ & \left. + [B(\Phi) + D(\Phi) e^{i\Phi}] J_{K-M} \left( \frac{U_p C(\Phi)}{\hbar\omega} \right) \right\}, \end{aligned} \quad (C9)$$

where  $F_K(x) = (U_i + U_p - K\hbar\omega)x - 2U_p[1 - \cos(x)]/x$ ,  $B(x) = -\frac{1}{2} + \sin(x)/x - 2\sin^2(x/2)/x^2$  and  $D(x) = -2B(x) - 1 + \cos(x)$ .  $J_j(\cdot)$  refers to the Bessel function of  $j$ th order. The function  $b_M(\Phi)$  has a cumbersome expression, whose analytical methods to compute it can be found in (Antoine *et al* 1996).

#### Appendix D. The Teramobile laser

Field experiments are required to characterize the filamentation over long distances as well as to develop atmospheric applications in real scale. Such experiments demand mobility to perform investigations at adequate locations. Studies of high power fs laser beam propagation over km-range distances can only be performed outdoors, where relevant aerosol pollutants are present, e.g. in urban areas or at industrial sites. Laser-induced lightning investigations require spots where the lightning probability is high, as well as test experiments at high voltage

facilities. These considerations clearly define the need for a mobile fs-TW laser system, embedded in a standard freight container-integrated laboratory equipped with the necessary LIDAR detection, power and cooling supplies, temperature stabilization, vibration control, and an additional standard LIDAR system to assure eye safety. These specifications were first achieved by the Teramobile system (Wille *et al* 2002). The laser itself is based on a Ti:sapphire CPA oscillator and a Nd:YAG pumped Ti:Sa amplification chain. It provides 350 mJ pulses with 70 fs duration resulting in a peak power of 5 TW at around 800 nm and with a repetition rate of 10 Hz. Its integration in the reduced space of the mobile laboratory required a particularly compact design (figure 38). The classical compressor setup has been improved into a chirp generator to pre-compensate the group velocity dispersion in air. Combined with an adjustable focus, this permits control of the location of filamentation onset and its length. Mechanical and thermal stabilities of the mobile laboratory are kept under control, so that the Teramobile can be transported to any place in the world and operated even under adverse weather conditions.

The Teramobile container also includes a LIDAR detection chain based on a 40 cm receiving telescope, a high-resolution spectrometer equipped with a set of gratings and detectors allowing simultaneous temporal and spectral analysis of the return signal in a wavelength range from 190 nm to 2.5  $\mu\text{m}$ .

## References

- Abramovitz M and Stegun I A 1972 *Handbook of Mathematical Functions* (New York: Dover)
- Ackermann R *et al* 2004 *Appl. Phys. Lett.* **85** 5781
- Ackermann R *et al* 2006a *Appl. Phys. B* **82** 561
- Ackermann R, Méjean G, Kasparian J, Yu J, Salmon E and Wolf J-P 2006b *Opt. Lett.* **31** 86
- Agostini P, Fabre F, Mainfray G, Petite G and Rahman N K 1979 *Phys. Rev. Lett.* **42** 1127
- Agrawal G P 2001 *Nonlinear Fiber Optics* 3rd edn (San Diego: Academic)
- Akhmediev N N, Korneev V I and Nabiev R F 1992 *Opt. Lett.* **17** 393
- Aközbek N, Scalora M, Bowden C M and Chin S L 2001 *Opt. Commun.* **191** 353
- Aközbek N, Iwasaki A, Becker A, Scalora M, Chin S L and Bowden C M 2002 *Phys. Rev. Lett.* **89** 143901
- Aközbek N, Becker A, Scalora M, Chin S L and Bowden C M 2003 *Appl. Phys. B* **77** 177
- Aközbek N *et al* 2006 *New J. Phys.* **8** 177
- Albert O, Roger S, Glinec Y, Loulergue J C, Etchepare J, Boulmer-Leborgne C, Peerièrè J and Millon E 2003 *Appl. Phys. A* **76** 319
- Alexeev I, Ting A, Gordon D F, Briscoe E, Peñano J R, Hubbard R F and Sprangle P 2004 *Appl. Phys. Lett.* **84** 4080
- Alexeev I, Ting A C, Gordon D F, Briscoe E, Hafizi B and Sprangle P 2005 *Opt. Lett.* **30** 1503
- Alfano R R and Shapiro S L 1970 *Phys. Rev. Lett.* **24** 584
- Ammosov M V, Delone N B and Krainov V P 1986 *Sov. Phys.—JETP* **64** 1191
- Anderson D and Bonnedal M 1979 *Phys. Fluids* **22** 105
- Anderson D and Lisak M 1983 *Phys. Rev. A* **27** 1393
- Angel S M, Stratis D N, Eland K L, Lai T, Berg M A and Gold D M 2001 *Fresenius J. Anal. Chem.* **369** 320
- Antoine P, L'Huillier A, Lewenstein M, Salières P and Carré B 1996 *Phys. Rev. A* **53** 1725
- Arévalo E and Becker A 2005 *Phys. Rev. E* **72** 026605
- Askar'yan G A 1962 *Sov. Phys.—JETP* **15** 1088
- Atai J, Chen Y and Soto-Crespo J M 1994 *Phys. Rev. A* **49** R3170
- Audebert P *et al* 1994 *Phys. Rev. Lett.* **73** 1990
- Augst S, Meyerhofer D D, Strickland D and Chin S L 1991 *J. Opt. Soc. Am. B* **8** 858
- Backus S, Peatross J, Zeek Z, Rundquist A, Taft G, Murnane M M and Kapteyn H C 1996 *Opt. Lett.* **21** 665
- Ball L M 1974 *Appl. Opt.* **13** 2292
- Baudelet M, Guyon L, Yu J, Wolf J-P, Fréjafon T A E and Laloi P 2006 *J. Appl. Phys.* **99** 084701
- Becker A, Aközbek N, Vijayalakshmi K, Oral E, Bowden C M and Chin S L 2001 *Appl. Phys. B* **73** 287
- Béjot P *et al* 2007 *Appl. Phys. Lett.* **90** 151106
- Bergé L 1998 *Phys. Rep.* **303** 259
- Bergé L 2004 *Phys. Rev. E* **69** 065601
- Bergé L and Couairon A 2000 *Phys. Plasmas* **7** 210



- Bergé L and Couairon A 2001a *Phys. Rev. Lett.* **86** 1003
- Bergé L and Couairon A 2001b *Physica D* **152–153** 752
- Bergé L and Skupin S 2005 *Phys. Rev. E* **71** 065601
- Bergé L, Schmidt M R, Rasmussen J J, Christiansen P L and Rasmussen K Ø 1997 *J. Opt. Soc. Am. B* **14** 2550
- Bergé L, Germaschewski K, Grauer R and Rasmussen J J 2002 *Phys. Rev. Lett.* **89** 153902
- Bergé L, Gouédard C, Schjødt-Eriksen J and Ward H 2003 *Physica D* **176** 181
- Bergé L *et al* 2004 *Phys. Rev. Lett.* **92** 225002
- Bergé L, Skupin S, Méjean G, Kasparian J, Yu J, Frey S, Salmon E and Wolf J P 2005 *Phys. Rev. E* **71** 016602
- Berkovsky A N, Kozlov S A and Shpolyanskiy Y A 2005 *Phys. Rev. A* **72** 043821
- Bernstein A C, Diels J-C, Luk T S, Nelson T R, McPherson A and Cameron S M 2003 *Opt. Lett.* **28** 2354
- Bespalov V I and Talanov V I 1966 *JETP Lett.* **3** 307
- Bourayou R *et al* 2005 *J. Opt. Soc. Am. B* **22** 369
- Boutou V, Favre C, Hill S C, Pan Y L, Chang R K and Wolf J-P 2002 *Appl. Phys. B* **75** 145
- Boyd R W (ed) 1992 *Nonlinear Optics* (San Diego: Academic)
- Brabec T and Krausz F 1997 *Phys. Rev. Lett.* **78** 3282
- Brabec T and Krausz F 2000 *Rev. Mod. Phys.* **72** 545
- Bransden B H and Joachain C J 2003 *Physics of Atoms and Molecules* (London: Pearson Education)
- Braun A, Korn G, Liu X, Du D, Squier J and Mourou G 1995 *Opt. Lett.* **20** 73
- Brodeur A and Chin S L 1998 *Phys. Rev. Lett.* **80** 4406
- Brodeur A and Chin S L 1999 *J. Opt. Soc. Am. B* **16** 637
- Brodeur A, Chien C Y, Ilkov F A, Chin S L, Kosareva O G and Kandidov V P 1997 *Opt. Lett.* **22** 304
- Buryak A V, Steblina V V and Sammut R A 1999 *Opt. Lett.* **24** 1859
- Campillo A J, Shapiro S L and Suydam B R 1973 *Appl. Phys. Lett.* **23** 628
- Campillo A J, Shapiro S L and Suydam B R 1974 *Appl. Phys. Lett.* **24** 178
- Cerullo G, Dienes A and Magni V 1996 *Opt. Lett.* **21** 65
- Chakraborty H S, Gaarde M B and Couairon A 2006 *Opt. Lett.* **31** 3662
- Champeaux S and Bergé L 2003 *Phys. Rev. E* **68** 066603
- Champeaux S and Bergé L 2005 *Phys. Rev. E* **71** 046604
- Champeaux S and Bergé L 2006 *Opt. Lett.* **31** 1301
- Chen X, Leng Y, Liu J, Zhu Y, Li R and Xu Z 2006 *Opt. Commun.* **259** 331
- Cheng C-C, Wright E M and Moloney J V 2001 *Phys. Rev. Lett.* **87** 213001
- Cheng C-C, Wright E M and Moloney J V 2002 *Phys. Rev. Lett.* **89** 139302
- Chernev P and Petrov V 1992a *Opt. Lett.* **17** 172
- Chernev P and Petrov V 1992b *Opt. Commun.* **87** 28
- Chiao R Y, Garmire E and Townes C H 1964 *Phys. Rev. Lett.* **13** 479
- Chin S L, Brodeur A, Petit S, Kosareva O G and Kandidov V P 1999a *J. Nonlinear Opt. Phys. Mater.* **8** 121
- Chin S L, Petit S, Borne F and Miyazaki K 1999b *Japan. J. Appl. Phys.* **38** L126
- Chin S L, Hosseini S A, Liu W, Luo Q, Théberge F, Aközbek N, Becker A, Kandidov V P, Kosareva O G and Schroeder H 2005 *Can. J. Phys.* **83** 863
- Chin S L, Petit S, Liu W, Iwasaki A, Nadeau M-C, Kandidov V P, Kosareva O G and Andrianov K Y 2002a *Opt. Commun.* **210** 329
- Chin S L, Talebpour A, Yang J, Petit S, Kandidov V P, Kosareva O G and Tamarov M P 2002b *Appl. Phys. B* **74** 67
- Chiron A, Lamouroux B, Lange R, Ripoche J-F, Franco M, Prade B, Bonnaud G, Riazuelo G and Mysyrowicz A 1999 *Eur. Phys. J. D* **6** 383
- Christodoulides D N, Efremidis N K, Di Trapani P and Malomed B A 2004 *Opt. Lett.* **29** 1446
- Comtois D *et al* 2000 *Appl. Phys. Lett.* **76** 819
- Conti C, Trillo S, Di Trapani P, Valiulis G, Piskarskas A, Jedrkiewicz O and Trull J 2003 *Phys. Rev. Lett.* **90** 170406
- Cook K, Kar A K and Lamb R A 2003 *Appl. Phys. Lett.* **83** 3861
- Cook K, McGeorge R, Kar A K, Taghizadeh M R and Lamb R A 2005 *Appl. Phys. Lett.* **86** 021105
- Corkum P B 1993 *Phys. Rev. Lett.* **71** 1994
- Corkum P B, Burnett N H and Brunel F 1989 *Phys. Rev. Lett.* **62** 1259
- Cornaggia C and Hering P 2000 *Phys. Rev. A* **62** 023403
- Couairon A 2003a *Phys. Rev. A* **68** 015801
- Couairon A 2003b *Eur. Phys. J. D* **27** 159
- Couairon A and Bergé L 2002 *Phys. Rev. Lett.* **88** 135003
- Couairon A and Mysyrowicz A 2007 *Phys. Rep.* **441** 47
- Couairon A, Tzortzakakis S, Bergé L, Franco M, Prade B and Mysyrowicz A 2002 *J. Opt. Soc. Am. B* **19** 1117

- Couairon A, Méchain G, Tzortzakis S, Franco M, Lamouroux B, Prade B and Mysyrowicz A 2003 *Opt. Commun.* **225** 177
- Couairon A, Franco M, Mysyrowicz A, Biegert J and Keller U 2005 *Opt. Lett.* **30** 2657
- Couairon A, Biegert J, Hauri C P, Kornelis W, Helbing F W, Keller U and Mysyrowicz A 2006a *J. Mod. Opt.* **53** 75
- Couairon A, Gaižauskas E, Faccio D, Dubietis A and Di Trapani P 2006b *Phys. Rev. E* **73** 016608
- Courvoisier F, Boutou V, Kasparian J, Salmon E, Méjean G, Yu J and Wolf J P 2003 *Appl. Phys. Lett.* **83** 213
- Cremers D A and Knight A K 2000 *Encyclopedia of Analytical Chemistry* (Chichester: Wiley) p 9595
- Cremers D A and Radziemski L J 2006 *Handbook of Laser-Induced Breakdown Measurements* (Chichester: Wiley)
- Desaix M, Anderson D and Lisak M 1991 *J. Opt. Soc. Am. B* **8** 2082
- Desyatnikov A, Torner L and Kivshar Y S 2005 *Prog. Opt.* **47** 291
- DeWitt M J, Wells E and Jones R R 2001 *Phys. Rev. Lett.* **87** 153001
- Dou K, Knobbe E T, Parkhill R L, Irwin B, Matthews L and Church K H 2003 *Appl. Phys. A* **76** 303
- Drescher M, Hentschel M, Kienberger R, Tempea G, Spielmann C, Reider G A, Corkum P B and Krausz F 2001 *Science* **291** 1923
- Du D, Liu X, Korn G, Squier J and Mourou G 1994 *Appl. Phys. Lett.* **64** 3071
- Dubietis A, Tamošauskas G, Diomin I and Varavavičius A 2003 *Opt. Lett.* **28** 1269
- Dubietis A, Gaižauskas E, Tamošauskas G and Di Trapani P 2004a *Phys. Rev. Lett.* **92** 253903
- Dubietis A, Kučinska E, Tamošauskas G, Gaižauskas E, Porras M A and Di Trapani P 2004b *Opt. Lett.* **29** 2893
- Dubietis A, Tamošauskas G, Fibich G and Ilan B 2004c *Opt. Lett.* **29** 1126
- Eisenmann S, Pukhov A and Zigler A 2007 *Phys. Rev. Lett.* **98** 155002
- Esarey E, Sprangle P, Krall J and Ting A 1997 *IEEE J. Quantum Electron.* **33** 1879
- Faccio D, Di Trapani P, Minardi S, Bramati A, Bragheri F, Liberale C, Degiorgio V, Dubietis A and Matijosius A 2005a *J. Opt. Soc. Am. B* **22** 862
- Faccio D, Matijosius A, Dubietis A, Piskarskas R, Varanavičius A, Gaizauskas E, Piskarskas A, Couairon A and Di Trapani P 2005b *Phys. Rev. E* **72** 037601
- Faccio D, Averchi A, Couairon A, Dubietis A, Piskarskas R, Matijosius A, Bragheri F, Porras M A, Piskarskas A and Trapani P D 2006a *Phys. Rev. E* **74** 047603
- Faccio D, Porras M A, Dubietis A, Bragheri F, Couairon A and Di Trapani P 2006b *Phys. Rev. Lett.* **96** 193901
- Faccio D, Porras M A, Dubietis A, Tamošauskas G, Kučinskas E, Couairon A and Di Trapani P 2006c *Opt. Commun.* **265** 672
- Faccio D, Averchi A, Dubietis A, Polesana P, Piskarskas A, Di Trapani P and Couairon A 2007 *Opt. Lett.* **32** 184
- Favre C, Boutou V, Hill S C, Zimmer W, Krenz M, Lambrecht H, Yu J, Chang R K, Woeste L and Wolf J-P 2002 *Phys. Rev. Lett.* **89** 035002
- Feit M D and Fleck J A 1974 *Appl. Phys. Lett.* **24** 169
- Feit M D and Fleck J A 1988 *J. Opt. Soc. Am. B* **5** 633
- Feng Q, Moloney J V, Newell A C and Wright E M 1995 *Opt. Lett.* **20** 1958
- Feng Q, Moloney J V, Newell A C, Wright E M, Cook K, Kennedy P K, Hammer D X, Rockwell B A and Thompson C R 1997 *IEEE J. Quantum Electron.* **33** 127
- Fibich G 1996 *Phys. Rev. Lett.* **76** 4356
- Fibich G, Eisenmann S, Ilan B, Erlich Y, Fraenkel M, Henis Z, Gaeta A L and Zigler A 2005 *Opt. Express* **13** 5897
- Fibich G, Eisenmann S, Ilan B and Zigler A 2004 *Opt. Lett.* **29** 1772
- Fibich G and Ilan B 2001a *Opt. Lett.* **26** 840
- Fibich G and Ilan B 2001b *Physica D* **157** 112
- Fibich G and Ilan B 2004 *Opt. Lett.* **29** 887
- Fibich G, Ilan B and Tsynkov S 2002 *J. Sci. Comput.* **17** 351
- Fibich G and Papanicolaou G 1999 *SIAM J. Appl. Math.* **60** 183
- Fibich G and Papanicolaou G C 1997 *Opt. Lett.* **22** 1379
- Fibich G, Ren W and Wang X-P 2003 *Phys. Rev. E* **67** 056603
- Fibich G, Sivan Y, Ehrlich Y, Louzon E, Fraenkel M, Eisenmann S, Katzir Y and Ziegler A 2006 *Opt. Express* **14** 4946
- Firth W J and Skryabin D V 1997 *Phys. Rev. Lett.* **79** 2450
- Fraiman G M 1985 *Sov. Phys.—JETP* **61** 228
- Fujii T and Fukuchi T (ed) 2005 *Femtosecond White-Light Lidar* (New York: Dekker)
- Gaeta A L 2000 *Phys. Rev. Lett.* **84** 3582
- Gaeta A L and Wise F 2001 *Phys. Rev. Lett.* **87** 229401
- Gatz S and Herrmann J 1997 *J. Opt. Soc. Am. B* **14** 1795
- Geissler M, Tempea G, Scrinzi A, Schnürer M, Krausz F and Brabec T 1999 *Phys. Rev. Lett.* **83** 2930
- Germaschewski K, Grauer R, Bergé L, Mezentssev V K and Rasmussen J J 2001 *Physica D* **151** 175
- Gil'denburg V B, Pozdnyakova V I and Shereshevskii I A 1995 *Phys. Lett. A* **203** 214

- Glasse R T 1977 *J. Math. Phys.* **18** 1794
- Golubtsov I S, Kandidov V P and Kosareva O G 2003 *Quantum Electron.* **33** 525
- Gong Q-H, Li J-L, Zhang T-Q and Yang H 1998 *Chin. Phys. Lett.* **15** 30
- Gordon D F, Ting A C, Alexeev I, Fischer R P and Sprangle P 2006 *IEEE Trans. Plasma Sci.* **34** 249
- Grow T D and Gaeta A L 2005 *Opt. Express* **13** 4594
- Guyon L, Courvoisier F, Boutou V, Nuter R, Vinçotte A, Champeaux S, Bergé L, Glorieux P and Wolf J-P 2006 *Phys. Rev. A* **73** 051802
- Hao Z-Q, Yu J, Zhang J, Li Y-T, Yuan X-H, Zheng Z-Y, Wang P, Wang Z-H, Ling W-J and Wei Z-Y 2005b *Chin. Phys. Lett.* **22** 636
- Hao Z, Zhang J, Li Y T, Lu X, Yuan X H, Zheng Z Y, Wang Z H, Ling W J and Wei Z Y 2005a *Appl. Phys. B* **80** 627
- Hao Z, Zhang J, Zhang Z, Yuan X, Zheng Z, Lu X, Jin Z, Wang Z, Zhong J and Liu Y 2006 *Phys. Rev. E* **74** 066402
- Hauri C P, Kornelis W, Helbing F W, Heinrich A, Couairon A, Mysyrowicz A, Biegert J and Keller U 2004 *Appl. Phys. B* **79** 673
- He G S and Liu S H 1999 *Physics of Nonlinear Optics* (Singapore: World Scientific)
- Heck G, Sloss J and Levis R J 2006 *Opt. Commun.* **259** 216
- Hellwarth R W, Pennington D M and Henesian M A 1990 *Phys. Rev. A* **41** 2766
- Henz S and Herrmann J 1999 *Phys. Rev. A* **59** 2528
- Homoelle D and Gaeta A L 2000 *Opt. Lett.* **25** 761
- Hosseini S A, Luo Q, Ferland B, Liu W, Chin S L, Kosareva O G, Panov N A, Aközbek N and Kandidov V P 2004a *Phys. Rev. A* **70** 033802
- Hosseini S A, Yu J, Luo Q and Chin S L 2004b *Appl. Phys. B* **79** 519
- Husakou A V and Herrmann J 2001 *Phys. Rev. Lett.* **87** 203901
- Jedrkwicz O, Picozzi A, Clerici M, Faccio D and Di Trapani P 2006 *Phys. Rev. Lett.* **97** 243903
- Jin Z, Zhang J, Xu M H, Lu X, Li Y T, Wang Z H, Wei Z Y, Yuan X H and Yu W 2005 *Opt. Express* **13** 10424
- Jong-Il Y, Klenze R and Kim J I 2002 *Appl. Spectrosc.* **56** 852
- Kandidov V P, Aközbek N, Scalora M, Kosareva O G, Nyakk A V, Luo Q, Hosseini S A and Chin S L 2005 *Appl. Phys. B* **80** 267
- Kandidov V P, Golubtsov I S and Kosareva O G 2004 *Quantum Electron.* **34** 348
- Kandidov V P, Kosareva O G, Golubtsov I S, Liu W, Becker A, Aközbek N, Bowden C M and Chin S L 2003 *Appl. Phys. B* **77** 149
- Kandidov V P, Kosareva O G and Shlenov S A 1994 *Quantum Electron.* **24** 905
- Kandidov V P, Kosareva O G, Tamarov M P, Brodeur A and Chin S L 1999 *Quantum Electron.* **29** 911
- Karlsson M, Anderson D and Desaix M 1992 *Opt. Lett.* **17** 22
- Kasprian J *et al* 2000b *Opt. Lett.* **25** 1397
- Kasprian J *et al* 2003 *Science* **301** 61
- Kasprian J, Sauerbrey R and Chin S L 2000a *Appl. Phys. B* **71** 877
- Kath W L and Smyth N F 1995 *Phys. Rev. E* **51** 1484
- Keldysh L V 1965 *Sov. Phys.—JETP* **20** 1307
- Kelley P L 1965 *Phys. Rev. Lett.* **15** 1005
- Kennedy P K 1995 *IEEE J. Quantum Electron.* **31** 2241
- Knight A K, Scherbarth N L, Cremers D A and Ferris M J 2000 *Appl. Spectrosc.* **54** 331
- Kolesik M, Katona G, Moloney J V and Wright E M 2003a *Phys. Rev. Lett.* **91** 043905
- Kolesik M, Katona G, Moloney J V and Wright E M 2003b *Appl. Phys. B* **77** 185
- Kolesik M and Moloney J V 2004a *Phys. Rev. E* **70** 036604
- Kolesik M and Moloney J V 2004b *Opt. Lett.* **29** 590
- Kolesik M, Moloney J V and Mlejnek M 2002 *Phys. Rev. Lett.* **89** 283902
- Kolesik M, Moloney J V and Wright E M 2001 *Phys. Rev. E* **64** 046607
- Kolesik M, Wright E M, Becker A and Moloney J V 2006 *Appl. Phys. B* **85** 531
- Kolesik M, Wright E M and Moloney J V 2004 *Phys. Rev. Lett.* **92** 253901
- Kolesik M, Wright E M and Moloney J V 2005 *Opt. Express* **13** 10729
- Konno K and Suzuki H 1979 *Phys. Scr.* **20** 382
- Koopman D W and Wilkerson T D 1971 *J. Appl. Phys.* **42** 1883
- Koprinkov I G, Suda A, Wang P and Midorikawa K 2000 *Phys. Rev. Lett.* **84** 3847
- Koprinkov I G, Suda A, Wang P and Midorikawa K 2001 *Phys. Rev. Lett.* **87** 229402
- Kosareva O, Kandidov V P, Brodeur A, Chien C Y and Chin S L 1997 *Opt. Lett.* **22** 1332
- Kosmatov N E, Shvets V F and Zakharov V E 1991 *Physica D* **52** 16
- Krainov V P 1997 *J. Opt. Soc. Am. B* **14** 425
- Kruglov V I, Logvin Y A and Volkov V M 1992 *J. Mod. Opt.* **39** 2277

- Kruglov V I and Vlasov R A 1985 *Phys. Lett. A* **111** 401
- Kuznetsov E A 1996 *Chaos* **6** 381
- Kuznetsov E A, Rasmussen J J, Rypdal K and Turitsyn S K 1995 *Physica D* **87** 273
- Kuznetsov E A, Rubenchik A M and Zakharov V E 1986 *Phys. Rep.* **142** 103
- Kyuseok S, Yong-Ill L and Sneddon J 1997 *Appl. Spectrosc. Rev.* **32** 183
- LaFontaine B, Vidal F, Comtois D, Chien C-Y, Desparois A, Johnston T-W, Kieffer J-C, Mercure H-P, Pépin H and Rizk F A M 1999a *IEEE Trans. Plasma Sci.* **27** 688
- LaFontaine B, Vidal F, Jiang Z, Chien C Y, Comtois D, Desparois A, Johnston T W, Kieffer J C, Pépin H and Mercure H P 1999b *Phys. Plasmas* **6** 1615
- Landman M J, Papanicolaou G C, Sulem C and Sulem P L 1988 *Phys. Rev. A* **38** 3837
- Lange H R, Chiron A, Ripoché J-F, Mysyrowicz A, Breger P and Agostini P 1998a *Phys. Rev. Lett.* **81** 1611
- Lange H R, Grillon G, Ripoché J-F, Franco M A, Lamouroux B, Prade B S, Mysyrowicz A, Nibbering E T J and Chiron A 1998b *Opt. Lett.* **23** 120
- Lehmeier H J, Leupacher W and Penzkofer A 1985 *Opt. Commun.* **56** 67
- Lehner T and Auby N 2000 *Phys. Rev. E* **61** 1996
- LeMesurier B J 2000 *Physica D* **138** 334
- LeMesurier B J, Christiansen P L, Gaididei Y B and Rasmussen J J 2004 *Phys. Rev. E* **70** 046614
- Lenzner M, Krüger J, Sartania S, Cheng Z, Spielmann C, Mourou G, Kautek W and Krausz F 1998 *Phys. Rev. Lett.* **80** 4076
- Lewenstein M, Balcou P, Ivanov M Y, L'Huillier A and Corkum P B 1994 *Phys. Rev. A* **49** 2117
- Li M, Menon S, Nibarger J P and Gibson G N 1999 *Phys. Rev. Lett.* **82** 2394
- Liou L W, Cao X D, McKinstrie C J and Agrawal G P 1992 *Phys. Rev. A* **46** 4202
- Litvak A G, Mironov V A and Sher E M 2000a *J. Exp. Theor. Phys.* **91** 1268
- Litvak A G, Mironov V A and Sher E M 2000b *Phys. Rev. E* **61** 891
- Liu W and Chin S L 2005 *Opt. Express* **13** 5750
- Liu W, Chin S L, Kosareva O, Golubtsov I S and Kandidov V P 2003 *Opt. Commun.* **225** 193
- Liu W, Hosseini S A, Luo Q, Ferland B, Chin S L, Kosareva O G, Panov N A and Kandidov V P 2004 *New J. Phys.* **6** 1
- Liu W, Kosareva O, Golubtsov I S, Iwasaki A, Becker A, Kandidov V P and Chin S L 2002 *Appl. Phys. B* **75** 595
- Liu J, Li R and Xu Z 2006a *Phys. Rev. A* **74** 043801
- Liu J, Schroeder H, Chin S L, Li R and Xu Z 2005a *Opt. Express* **13** 10248
- Liu J, Schroeder H, Chin S L, Li R, Yu W and Xu Z 2005b *Phys. Rev. A* **72** 053817
- Liu W, Théberge F, Arevalo E, Gravel J-F, Becker A and Chin S L 2005c *Opt. Lett.* **30** 2602
- Liu W, Théberge F, Daigle J-F, Simard P T, Sarifi S M, Kamali Y, Xu H L and Chin S L 2006b *Appl. Phys. B* **85** 55
- Longhi S 2004 *Opt. Lett.* **29** 147
- Lotz W 1967a *Z. Phys.* **206** 205
- Lotz W 1967b *J. Opt. Soc. Am.* **57** 873
- Lugovoi V N and Prokhorov A M 1974 *Sov. Phys.—Usp.* **16** 658
- Luo Y, Ågren H, Minaev B and Jørgensen P 1995 *J. Mol. Struct.* **336** 61
- Luther G G, Moloney J V, Newell A C and Wright E M 1994a *Opt. Lett.* **19** 862
- Luther G G, Newell A C and Moloney J V 1994b *Physica D* **74** 59
- Luther G G, Newell A C, Moloney J V and Wright E M 1994c *Opt. Lett.* **19** 789
- Mairesse Y *et al* 2003 *Science* **302** 1540
- Malkin V M 1990 *Phys. Lett. A* **151** 285
- Malkin V M 1993 *Physica D* **64** 251
- Manassah J T 1992 *Opt. Lett.* **17** 1259
- Marburger J H 1975 *Prog. Quantum Electron.* **4** 35
- Mariyenko I G, Strohaber J and Uiterwaal C J G J 2005 *Opt. Express* **13** 7599
- Marklund M and Shukla P K 2006 *Opt. Lett.* **31** 1884
- Martin P, Guizard S, Daguzan P, Petite G, D'Oliveira P, Meynadier P and Perdrix M 1997 *Phys. Rev. B* **55** 5799
- McKinstrie C J and Russell D A 1988 *Phys. Rev. Lett.* **61** 2929
- Measures R M 1984 *Laser Remote Sensing—Fundamentals and Applications* (New York: Wiley-Interscience)
- Méchain G, Couairon A, Franco M, Prade B and Mysyrowicz A 2004 *Phys. Rev. Lett.* **93** 035003
- Méchain G, D'Amico C, André Y-B, Tzortzakis S, Franco M, Prade B, Mysyrowicz A, Couairon A, Salmon E and Sauerbrey R 2005a *Opt. Commun.* **247** 171
- Méchain G *et al* 2005b *Appl. Phys. B* **80** 785
- Méjean G *et al* 2006a *Appl. Phys. Lett.* **88** 021101
- Méjean G, Kasparian J, Yu J, Frey S, Salmon E, Ackermann R, Wolf J-P, Bergé L and Skupin S 2006b *Appl. Phys. B* **82** 341

- Méjean G, Kasparian J, Yu J, Frey S, Salmon E and Wolf J P 2004 *Appl. Phys. B* **78** 535
- Méjean G *et al* 2005 *Phys. Rev. E* **72** 026611
- Mével E, Tcherbakoff O, Salin F and Constant E 2003 *J. Opt. Soc. Am. B* **20** 105
- Meyers R A 2000 *Encyclopedia of Analytical Chemistry* (Chichester: Wiley)
- Michinel H, Campo-Táboas J, Quiroga-Teixeiro M L, Salgueiro J R and García-Fernández R 2001 *J. Opt. B: Quantum Semiclass. Opt.* **3** 314
- Miki M, Aihara Y and Shindo T 1993 *J. Phys. D: Appl. Phys.* **26** 1244
- Milsted C S Jr and Cantrell C D 1996 *Phys. Rev. A* **53** 3536
- Mlejnek M, Kolesik M, Moloney J V and Wright E M 1999 *Phys. Rev. Lett.* **83** 2938
- Mlejnek M, Wright E M and Moloney J V 1998a *Opt. Lett.* **23** 382
- Mlejnek M, Wright E M and Moloney J V 1998b *Phys. Rev. E* **58** 4903
- Moll K D and Gaeta A L 2004 *Opt. Lett.* **29** 995
- Moll K D, Gaeta A L and Fibich G 2003 *Phys. Rev. Lett.* **90** 203902
- Muth-Böhm J, Becker A and Faisal F H M 2000 *Phys. Rev. Lett.* **85** 2280
- Nibbering E T J, Curley P F, Grillon G, Prade B S, Franco M A, Salin F and Mysyrowicz A 1996 *Opt. Lett.* **21** 62
- Nibbering E T J, Grillon G, Franco M A, Prade B S and Mysyrowicz A 1997 *J. Opt. Soc. Am. B* **14** 650
- Niessner R 1994 *Proc. SPIE* **2360** 254
- Nishioka H, Odajima W, Ueda K and Takuma H 1995 *Opt. Lett.* **20** 2505
- Nisoli M, De Silvestri S, Svelto O, Szpöcs R, Ferencz K, Spielmann C, Sartania S and Krausz F 1997a *Opt. Lett.* **22** 522
- Nisoli M, Stagira S, Silvestri S D, Svelto O, Sartania S, Cheng Z, Lenzner M, Spielmann C and Krausz F 1997b *Appl. Phys. B* **65** 189
- Nisoli M, Stagira S, Silvestri S D, Svelto O, Sartania S, Cheng Z, Tempea G, Spielmann C and Krausz F 1998 *IEEE J. Sel. Top. Quantum Electron.* **4** 414
- Noack J and Vogel A 1999 *IEEE J. Quantum Electron.* **35** 1156
- Nurhuda M, Suda A, Hatayama M, Nagasaka K and Midorikawa K 2002a *Phys. Rev. A* **66** 023811
- Nurhuda M, Suda A and Midorikawa K 2002b *RIKEN Rev.* **48** 40
- Nuter R and Bergé L 2006 *J. Opt. Soc. Am. B* **23** 874
- Nuter R, Skupin S and Bergé L 2005 *Opt. Lett.* **30** 917
- Painter J C, Adams M, Brimhall N, Christensen E, Giraud G, Powers N, Turner M, Ware M and Peatross J 2006 *Opt. Lett.* **31** 3471
- Pan L, Taylor K T and Clark C W 1990 *J. Opt. Soc. Am. B* **7** 509
- Peck E R and Reeder K 1972 *J. Opt. Soc. Am.* **62** 958
- Peñano J R, Sprangle P, Hafizi B, Manheimer W and Zigler A 2005 *Phys. Rev. E* **72** 036412
- Peñano J R, Sprangle P, Hafizi B, Ting A, Gordon D F and Kapetanakis C A 2004 *Phys. Plasmas* **11** 2865
- Peñano J R, Sprangle P, Serafim P, Hafizi B and Ting A 2003 *Phys. Rev. E* **68** 056502
- Penetrante B M, Bardsley J N, Wood W M, Siders C W and Downer M C 1992 *J. Opt. Soc. Am. B* **9** 2032
- Pépin H *et al* 2001 *Phys. Plasmas* **8** 2532
- Perelomov A M and Popov V S 1967 *Sov. Phys.—JETP* **25** 336
- Perelomov A M, Popov V S and Terent'ev M V 1966 *Sov. Phys.—JETP* **23** 924
- Perelomov A M, Popov V S and Terent'ev M V 1967 *Sov. Phys.—JETP* **24** 207
- Perry M D, Landen O L, Szöke A and Campbell E M 1988a *Phys. Rev. A* **37** 747
- Perry M D, Szöke A, Landen O L and Campbell E M 1988b *Phys. Rev. Lett.* **60** 1270
- Petit S, Talebpour A, Proulx A and Chin S L 2000 *Opt. Commun.* **175** 323
- Pfeifer T, Spielmann C and Gerber G 2006 *Rep. Prog. Phys.* **69** 443
- Polesana P, Dubietis A, Porras M A, Kučinskas E, Faccio D, Couairon A and Di Trapani P 2006 *Phys. Rev. E* **73** 056612
- Porras M A and Di Trapani P 2004 *Phys. Rev. E* **69** 066606
- Porras M A, Dubietis A, Kučinskas E, Bragheri F, Degiorgio V, Couairon A, Faccio D and Di Trapani P 2005 *Opt. Lett.* **30** 3398
- Porras M A, Parola A, Faccio D, Dubietis A and Di Trapani P 2004 *Phys. Rev. Lett.* **93** 153902
- Quigora-Teixeiro M and Michinel H 1997 *J. Opt. Soc. Am. B* **14** 2004
- Rae S C and Burnett K 1992 *Phys. Rev. A* **46** 1084
- Rairoux *et al* 2000 *Appl. Phys. B* **71** 573
- Rambo P, Schwartz J and Diels J-C 2001 *J. Opt. A: Pure Appl. Opt.* **3** 146
- Ranka J K and Gaeta A L 1998 *Opt. Lett.* **23** 534
- Rasmussen J J and Rypdal K 1986 *Phys. Scr.* **33** 481
- Rayner D M, Naumov A and Corkum P B 2005 *Opt. Express* **13** 3208
- Reiss H R 1980 *Phys. Rev. A* **22** 1786



- Ripoche J F, Grillon G, Prade B, Franco M, Nibbering E, Lange R and Mysyrowicz A 1997 *Opt. Commun.* **135** 310
- Rodriguez et al 2002 *Opt. Lett.* **27** 772
- Rodriguez M et al 2004 *Phys. Rev. E* **69** 036607
- Rohwetter P, Stelmaszczyk K, Méjean G, Yu J, Salmon E, Kasparian J, Wolf J-P and Wöste L 2003 *J. Anal. At. Spectrom.* **19** 437
- Rothenberg J E 1992 *Opt. Lett.* **17** 1340
- Rypdal K and Rasmussen J J 1989 *Phys. Scr.* **40** 192
- Rypdal K, Rasmussen J J and Thomsen K 1985 *Physica D* **16** 339
- Salières P and Lewenstein M 2001 *Meas. Sci. Technol.* **12** 1818
- Schjöldt-Eriksen J, Gaididei Y B and Christiansen P L 2001a *Phys. Rev. E* **64** 066614
- Schjöldt-Eriksen J, Moloney J V, Wright E M, Feng Q and Christiansen P L 2001b *Opt. Lett.* **26** 78
- Schroeder H and Chin S L 2004 *Opt. Commun.* **234** 399
- Schroeder H, Liu J and Chin S L 2004 *Opt. Express* **12** 4768
- Schwarz J, Rambo P and Diels J-C 2001 *Appl. Phys. B* **72** 343
- Schwarz J, Rambo P, Diels J-C, Kolesik M, Wright E M and Moloney J V 2000 *Opt. Commun.* **180** 383
- Scrinzi A, Ivanov M Y, Kienberger R and Villeneuve D M 2006 *J. Phys. B: At. Mol. Opt. Phys.* **39** 1
- Sharma S K, Lucey P G, Ghosh M, Hubble H W and Horton K A 2003 *Spectrochim. Acta A* **59** 2391
- Shen Y R 1976 *Rev. Mod. Phys.* **48** 1
- Shen Y R 1984 *The Principles of Nonlinear Optics* (New York: Wiley)
- Silberberg Y 1990 *Opt. Lett.* **15** 1282
- Skupin S and Bergé L 2006 *Physica D* **220** 14
- Skupin S, Bergé L, Peschel U and Lederer F 2004a *Phys. Rev. Lett.* **93** 023901
- Skupin S et al 2004b *Phys. Rev. E* **70** 046602
- Skupin S, Nuter R and Bergé L 2006a *Phys. Rev. A* **74** 043813
- Skupin S, Peschel U, Etrich C, Leine L, Lederer F and Michaelis D 2003 *Opt. Quantum Electron.* **35** 573
- Skupin S, Peschel U, Etrich C, Leine L, Michaelis D and Lederer F 2002 *Opt. Lett.* **27** 1812
- Skupin S, Stibenz G, Bergé L, Lederer F, Sokollik T, Schnürer M, Zhavoronkov N and Steinmeyer G 2006b *Phys. Rev. E* **74** 056604
- Soto-Crespo J M, Wright E M and Akhmediev N N 1992 *Phys. Rev. A* **45** 3168
- Sprangle P, Esarey E and Krall J 1996 *Phys. Rev. E* **54** 4211
- Sprangle P, Peñano J R and Hafizi B 2002 *Phys. Rev. E* **66** 046418
- Sprangle P, Peñano J R, Hafizi B and Kapetanakis C A 2004 *Phys. Rev. E* **69** 066415
- Steinmeyer G, Sutter D H, Gallmann L, Matuschek N and Keller U 1999 *Science* **286** 1507
- Stelmaszczyk K, Rohwetter P, Méjean G, Yu J, Salmon E, Kasparian J, Ackermann R, Wolf J-P and Wöste L 2004 *Appl. Phys. Lett.* **85** 3977
- Stibenz G, Zhavoronkov N and Steinmeyer G 2006 *Opt. Lett.* **31** 274
- Stuart B C, Feit M D, Herman S, Rubenchik A M, Shore B W and Perry M D 1996 *Phys. Rev. B* **53** 1749
- Suda A, Hatayama M, Nagasaka K and Midorikawa K 2005 *Appl. Phys. Lett.* **86** 111116
- Sudrie L, Couairon A, Franco M, Lamouroux B, Prade B, Tzortzakis S and Mysyrowicz A 2002 *Phys. Rev. Lett.* **89** 186601
- Sudrie L, Franco M, Prade B and Mysyrowicz A 1999 *Opt. Commun.* **171** 279
- Sudrie L, Franco M, Prade B and Mysyrowicz A 2001 *Opt. Commun.* **191** 333
- Sulem C and Sulem P-L 1999 *The Nonlinear Schrödinger Equation: Self-focusing and Wave Collapse* 1st edn (New York: Springer)
- Talebpour A, Yang J and Chin S L 1999 *Opt. Commun.* **163** 29
- Tamaki Y, Itatani J, Nagata Y, Obara M and Midorikawa K 1999 *Phys. Rev. Lett.* **82** 1422
- Tempea G and Brabec T 1998a *Opt. Lett.* **23** 1286
- Tempea G and Brabec T 1998b *Opt. Lett.* **23** 762
- Théberge F, Aközbek N, Liu W, Becker A and Chin S L 2006a *Phys. Rev. Lett.* **97** 023904
- Théberge F, Aközbek N, Liu W, Gravel J-F and Chin S L 2005a *Opt. Commun.* **245** 399
- Théberge F, Liu W, Luo Q and Chin S L 2005b *Appl. Phys. B* **80** 221
- Théberge F, Liu W, Simard P T, Becker A and Chin S L 2006b *Phys. Rev. E* **74** 036406
- Theopold F A, Wolf J-P and Wöste L 2005 *Dial Revisited: Belinda and White-Light Femtosecond Lidar in Range-resolved Optical Sensing of the Atmosphere* (New York: Springer)
- Tien A-C, Backus S, Kapteyn H, Murnane M and Mourou G 1999 *Phys. Rev. Lett.* **82** 3883
- Tikhonenko V, Christou J and Luther-Davies B 1996 *Phys. Rev. Lett.* **76** 2698
- Ting A, Alexeev I, Gordon D, Fisher N, Kaganovitch D, Jones T, Briscoe E, Peñano J, Hubbard R and Sprangle P 2005a *Phys. Plasmas* **12** 056705



- Ting A, Gordon D F, Briscoe E, Peñano J R and Sprangle P 2005b *Appl. Opt.* **44** 1474
- Tohmon R, Mizuno H, Ohki Y, Sasagane K, Nagasawa K and Hama Y 1989 *Phys. Rev. B* **39** 1337
- Tong X M, Zhao Z X and Lin C D 2002 *Phys. Rev. A* **66** 033402
- Tosa V, Takahashi E, Nabekawa Y and Midorikawa K 2003 *Phys. Rev. A* **67** 063817
- Trillo S and Torruellas W (ed) 2001 *Spatial Solitons* (Berlin: Springer)
- Trushin S A, Panja S, Kosma K, Schmid W E and Fuss W 2005 *Appl. Phys. B* **80** 399
- Tzortzakis S, Anglos D and Gray D 2006 *Opt. Lett.* **31** 1139
- Tzortzakis S, Bergé L, Couairon A, Franco M, Prade B and Mysyrowicz A 2001a *Phys. Rev. Lett.* **86** 5470
- Tzortzakis S *et al* 2002 *Opt. Lett.* **27** 1944
- Tzortzakis S, Franco M A, André Y-B, Chiron A, Lamouroux B, Prade B S and Mysyrowicz A 1999 *Phys. Rev. E* **60** R3505
- Tzortzakis S, Lamouroux B, Chiron A, Franco M, Prade B, Mysyrowicz A and Moustazis S D 2000a *Opt. Lett.* **25** 1270
- Tzortzakis S, Lamouroux B, Chiron A, Moustazis S D, Anglos D, Franco M, Prade B and Mysyrowicz A 2001b *Opt. Commun.* **197** 131
- Tzortzakis S, Méchain G, Patalano G, Franco M, Prade B and Mysyrowicz A 2003 *Appl. Phys. B* **76** 609
- Tzortzakis S, Prade B, Franco M and Mysyrowicz A 2000b *Opt. Commun.* **181** 123
- Tzortzakis S, Prade B, Franco M, Mysyrowicz A, Hüller S and Mora P 2001c *Phys. Rev. E* **64** 057401
- Tzortzakis S, Sudrie L, Franco M, Prade B, Mysyrowicz A, Couairon A and Bergé L 2001d *Phys. Rev. Lett.* **87** 213902
- Vakhitov N G and Kolokolov A A 1975 *Radiophys. Quantum Electron.* **16** 783
- Verhoef A J, Seres J, Schmid K, Nomura Y, Tempea G, Veisz L and Krausz F 2006 *Appl. Phys. B* **82** 513
- Vidal F and Johnston T W 1996 *Phys. Rev. Lett.* **77** 1282
- Vinçotte A and Bergé L 2004 *Phys. Rev. A* **70** 061802
- Vinçotte A and Bergé L 2005 *Phys. Rev. Lett.* **95** 193901
- Vlasov S N, Petrishchev V A and Talanov V I 1974 *Radiophys. Quantum Electron.* **14** 1062
- Vlasov S N, Piskunova L V and Talanov V I 1989 *Sov. Phys.—JETP* **68** 1125
- Vuong L T, Grow T D, Ishaaya A, Gaeta A L, 't Hooft G W, Eliel E R and Fibich G 2006 *Phys. Rev. Lett.* **96** 133901
- Wagner N L, Gibson E A, Popmintchev T, Christov I P, Murnane M M and Kapteyn H C 2004 *Phys. Rev. Lett.* **93** 173902
- Ward H and Bergé L 2003 *Phys. Rev. Lett.* **90** 053901
- Weinstein M I 1983 *Commun. Math. Phys.* **87** 567
- Wiens R C, Arvidson R E, Cremers D A, Ferris M J, Blacic J D and Seelos F P IV 2002 *J. Geophys. Res. Planet.* **107** 8004
- Wille H, Rodriguez M, Kasparian J, Mondelain D, Yu J, Mysyrowicz A, Sauerbrey R, Wolf J P and Wöste L 2002 *Eur. Phys. J.—Appl. Phys.* **20** 183
- Wolf J-P 2000 Ultraviolet/visible light detection and ranging applications in air monitoring *Encyclopedia of Analytical Chemistry* (Chichester: Wiley)
- Wöste L *et al* 1997 *Laser Optoelektron.* **29** 51
- Xi T-T, Lu X and Zhang J 2006 *Phys. Rev. Lett.* **96** 025003
- Xu H L, Daigle J F, Luo Q and Chin S L 2006a *Appl. Phys. B* **82** 655
- Xu X H, Liu W and Chin S L 2006b *Opt. Lett.* **31** 1540
- Yablonovitch E 1974 *Phys. Rev. A* **10** 1888
- Yablonovitch E and Bloembergen N 1972 *Phys. Rev. Lett.* **29** 907
- Yamane K, Zhang Z, Oka K, Morita R, Yamashita M and Suguro A 2003 *Opt. Lett.* **28** 2258
- Yang H *et al* 2003 *Phys. Rev. E* **67** 015401
- Yang G and Shen Y R 1984 *Opt. Lett.* **9** 510
- Yu J, Mondelain D, Ange G, Volk R, Niedermeier S, Wolf J-P, Kasparian J and Sauerbrey R 2001 *Opt. Lett.* **26** 533
- Yu J, Mondelain D, Kasparian J, Salmon E, Geffroy S, Favre C, Boutou V and Wolf J-P 2003 *Appl. Opt.* **42** 7117
- Zakharov V E and Kuznetsov E A 1986 *Sov. Phys.—JETP* **64** 773
- Zakharov V E and Rubenchik A M 1974 *Sov. Phys.—JETP* **38** 494
- Zeng Z, Li R, Yu W and Xu Z 2003 *Phys. Rev. A* **67** 013815
- Zharova N A, Litvak A G and Mironov V A 2003 *J. Exp. Theor. Phys.* **96** 643
- Zozulya A A, Diddams S A, Van Engen A G and Clement T S 1999 *Phys. Rev. Lett.* **82** 1430

# Erratum

## Ultrashort filaments of light in weakly ionized, optically transparent media

L Bergé, S Skupin, R Nuter, J Kasparian and J-P Wolf

2007 *Rep. Prog. Phys.* **70** 1633–1713

Due to a typesetting error, a factor 0.367 is missing in the denominator of the collapse distance evaluated for focused Gaussian beams from the Marburger formula [see equation (50)]. The complete correct version of this formula is given below:

$$z_c = \frac{0.367 z_0}{\sqrt{\left(\sqrt{\frac{P_{\text{in}}}{P_{\text{cr}}}} - 0.852\right)^2 - 0.0219 + 0.367 \frac{z_0}{f}}}.$$